UNIVERSITÀ
DEGLI STUDI
DI PADOVA

Administrative unit: University of Padova

Department: **Land, Environment, Agriculture and Forestry (TESAF)**

PhD Program: **Land, Environment, Resources and Health (LERH)**

Batch: XXXIV

Bridging the mass – flow modelling with the reality

Thesis financially supported by CARIPARO Foundation

PhD Program Coordinator: Prof. Marco Borga

Supervisor: Prof. Vincenzo D'Agostino

PhD candidate: Tommaso Baggio

UNIVERSITÀ
DEGLI STUDI
DI PADOVA

Sede Amministrativa: Università degli Studi di Padova

Dipartimento Territorio e Sistemi Agro-Forestali (TESAF)

CORSO DI DOTTORATO DI RICERCA: **Land, Environment, Resources, Health (LERH)**

Ciclo: XXXIV

Congiungere la modellazione dei movimenti di massa alla realtà

Tesi redatta con il contributo finanziario della Fondazione CARIPARO

Coordinatore: Prof. Marco Borga

Supervisore: Prof. Vincenzo D'Agostino

Dottorando: Tommaso Baggio

Table of Contents

Summary

Mass flows are gravitational natural hazards typical of mountain areas causing economic losses and fatalities every year. Numerical models are a way to predict the propagation of potential mass flow events over a certain topography. To appropriately predict the consequences of future events, models require different inputs. Among them, the released volume, the triggering conditions and processes of interaction with the topography consistently affect the outcomes of mass flow models. Therefore, the main objective of the thesis is to improve: i) the phase of preparatory quantification of the input mass volume; ii) the following implementation of processes of interaction with the basal topography in order to increase the prediction of their dynamics through models; and, consequently, iii) the quality of hazard and risk mapping. In this context, the research focuses on two types of mass flows: debris flows and snow avalanches. Regarding debris flows, the study aims to improve the reliability of models to capture the increase in flow volume through channel bed erosion and mitigation structure collapse. For snow avalanches, the study aims to improve the identification of possible avalanche release areas taking into account the role of different types of vegetation structures. The thesis structure is a collection of articles of which three already published and one is currently under review.

The first paper improves the representation of debris flow erosion processes in computational models thanks to data of a severe event occurred in the rio Gere catchment (Veneto, IT). Exploiting the functionalities of a recent mass flow model, a function based on a smoothed terrain slope map is calibrated to derive the erosion coefficient. The erosion coefficient is then used to reproduce the observed erosion process occurred in the channel. Results can improve the reliability of future scenarios related to debris flows for which bed erosion plays an important role in the dynamic of the flow. The second study defines a procedure to simulate the effect of check dam collapse in a debris flow event. The methodology is proposed and successfully evaluated in the rio Rotian channel (Trentino, IT) where an extreme rainfall event triggered a debris flow causing the collapse of a series of 15 check dams. The developed methodology can be straight applied to map the residual risk of mountain channels or where the lack of maintenance may decrease torrent countermeasure stability and the probability of collapse may increase. The third paper involves the study of terrain roughness. We test seven algorithms computing terrain roughness in two study areas (Franza, IT and Braema, CH) with the aim to identify which roughness algorithm can represent in the most appropriate way the features on the ground (rocks, forests, etc.) interacting with natural hazards, especially focusing on vegetation structures commonly not considered (e.g., sparse and disturbed forests). Outcomes show that the best algorithm results the vector ruggedness and that the increase in data resolution does not improve the classification performance. Results can improve the reliability of mass flow propagation models over natural areas providing a better identification of potential release areas of snow avalanches. The fourth project analyses the protection capacity of forests affected by windstorms. Thanks to multi-temporal observations, we develop and test two new algorithms to assess the characteristics of abated trees. Results assess the time of minimum level of forest protection against snow avalanches and the successive recovery

time. The developed algorithms could be applied at regional scale (on regions covered by remote sensed data) to provide immediate information of the protection capacity of wind disturbed forests for a management purpose and consequently monitor their changes over time.

The results of the research projects enhance the reliability of mass flow models through the improvement in (i) the estimation of the released volume, (ii) the implementation in models of mechanisms of mass release and (iii) mass flow interaction with the basal topography. In particular, the projects investigated entrainment processes, effect of mitigation structure failures and the identification of potential triggering areas. Outcomes of the four papers fill the respective gaps of knowledge, improving our capability to manage better several uncertainties in mass flow numerical modelling. Furthermore, the projects have strong methodological outcomes and new methods to improve the volume estimation of mass flows are developed and tested. Such methods are further applicable outside of the study areas, supporting different stakeholders in the management of natural hazards of mountain areas.

Sommario

I flussi di massa sono pericoli naturali di tipo gravitativo caratteristici delle zone montane che causano ogni anno perdite economiche e vittime. I modelli numerici sono strumenti utili per prevedere la propagazione di potenziali eventi di flussi di massa su una determinata topografia. Per riprodurre realisticamente possibili eventi futuri, i modelli richiedono diversi input. Gli input e i processi che sostanzialmente influenzano i risultati dei modelli sono rappresentati dalla quantificazione del volume, dalle condizioni di innesco e dalle interazioni topografia – flusso di massa. Pertanto, l'obiettivo principale della tesi è quello di migliorare la quantificazione del volume coinvolto in un evento di flusso di massa e di aumentare la rappresentazione dell'interazione tra il flusso e la topografia al fine di aumentarne l'accuratezza della loro dinamica attraverso i modelli numerici. In questo contesto, sono stati studiati due tipi di flussi di massa: debris flow e valanghe di neve. Per quanto riguarda i debris flow, la tesi vuole migliorare l'affidabilità dei modelli analizzando l'aumento del volume del flusso attraverso l'erosione del letto del canale e il collasso di strutture di mitigazione. Per le valanghe di neve, lo studio ha come obbiettivo quello di migliorare l'identificazione delle possibili aree di distacco prendendo in considerazione il ruolo di diversi tipi vegetazionali. La tesi è stata strutturata come una raccolta di articoli dei quali tre sono stati pubblicati e uno è attualmente in fase di revisione.

Il primo articolo ha migliorato la rappresentazione dei fenomeni erosivi nei modelli numerici grazie ai dati di un intenso evento di debris flow avvenuto nel bacino del rio Gere (Veneto, IT). Sfruttando le funzionalità di un recente modello di flusso di massa, è stata calibrata una funzione basata sui valori di pendenza topografica per ricavare il coefficiente di erosione. Il coefficiente di erosione è stato poi utilizzato per riprodurre l'erosione osservata nel canale. I risultati sono utili per migliorare l'accuratezza di futuri scenari da debris flow per i quali l'erosione del fondo rappresenta un processo importante nella dinamica del flusso. Il secondo studio ha definito una procedura per simulare l'effetto del collasso delle briglie di consolidamento in un evento di debris flow. La metodologia è stata sviluppata e testata con successo nel rio Rotian (Trentino, IT), dove un evento di pioggia estrema ha innescato un debris flow che ha provocato il collasso di una serie di 15 briglie. La metodologia sviluppata può essere direttamente applicata per mappare il rischio residuo dei canali da debris flow in cui siano presenti opere o dove la mancanza di manutenzione delle misure di mitigazione può diminuire la loro stabilità e quindi aumentare la probabilità di collasso. Il terzo progetto riguarda lo studio della rugosità del terreno. Sette algoritmi di calcolo della rugosità sono stati testati in due aree studio (Franza, IT e Braema, CH) al fine di identificare quale algoritmo possa rappresentare nel modo più appropriato le tipologie del terreno (rocce, foreste, ecc.) che interagiscono con i fenomeni di massa, concentrandosi soprattutto su tipologie vegetative solitamente non considerate (foreste poco dense/giovani o che hanno subito dei disturbi). I risultati hanno mostrato che il miglior algoritmo è risultato il vector ruggedness e che l'utilizzo di una risoluzione maggiore non ha migliorato le performance. I risultati, aumentando l'accuratezza della perimetrazione delle potenziali aree di distacco di valanghe, possono migliorare l'affidabilità dei modelli di propagazione del flusso di massa su aree naturali.

Il quarto progetto ha analizzato la capacità di protezione delle foreste colpite da tempeste di vento. Grazie a osservazioni multi-temporali abbiamo sviluppato e testato due nuovi algoritmi per valutare le caratteristiche degli alberi abbattuti. I risultati hanno evidenziato che il momento di protezione minimo delle foreste contro le valanghe di neve è dopo 10 anni l'evento di tempesta. Inoltre, gli algoritmi sviluppati nello studio possono essere applicati direttamente su scala regionale (purchè coperti da dati di telerilevamento) per migliorare la gestione e il monitoraggio delle aree forestali interessate da danni da vento.

I risultati dei progetti di ricerca possono aumentare l'affidabilità dei modelli di flusso di massa grazie ai miglioramenti nella stima del volume di input, l'implementazione di nuovi meccanismi di rilascio del volume e interazioni tra flusso e topografia. I diversi studi hanno analizzato i processi di erosione, l'effetto del collasso di briglie e l'identificazione di potenziali aree di innesco. I risultati dei quattro progetti hanno risposto ai corrispondenti obbiettivi, migliorando la comprensione dei flussi di massa e quindi la previsione di eventi futuri. Inoltre, i progetti forniscono importanti risultati metodologici e nuovi metodi sono stati sviluppati e testati al fine di migliorare la stima del volume dei flussi di massa. Tali metodi sono inoltre applicabili al di fuori delle aree di studio prese in esame, dando supporto a diversi stakeholder nella gestione dei rischi naturali in aree montane.

1 General introduction

1.1 Research background and justification

Natural hazards cause every year victims and economic losses (Gall et al., 2011; Raschky, 2008) worldwide. This trend is increasing in the last decades due to climate change (IPCC, 2021) and the increase in the world population living in exposed areas (Fuchs et al., 2017). Consequently, the number and the extension of risk prone areas subjected to natural hazards will increase in the next decades (Huppert and Sparks, 2006). Mass flows are a type of natural hazards and they can be defined as movements of a material or a mix of them moving down through a certain topography driven by the gravity (Mergili et al., 2017). These events involve snow, rock, or ice avalanches, landslides and debris flows. In the last decades, different models were implemented to reproduce and then to study the formation, dynamic, properties and peculiarities of such devastating phenomena (Pudasaini and Hutter, 2007). Models are fundamental tools to predict probable impact areas, impact forces, travel times and runout distances. Basing on the model results, civil authorities can set up specific evacuation plans and project infrastructures to mitigate the effects of these events (Barbolini et al., 2000; Jamieson and Stethem, 2002; Soares-Frazão et al., 2008). For these reasons, mass flow models are extremely useful tools to identify and predict the consequence of mass movements.

In this research work the focus is on debris flows and snow avalanches because they are the most frequent types of mass flow affecting the Alp region. Debris flows are multiphase gravity – driven flows consisting of randomly dispersed interacting phase (O'Brien et al., 1993). They are a mixture of sediment and water, moving downstream driven by the gravitational force and they reach an extremely high mobility thanks to the presence of internal gap filled by water (Takahashi, 2007). The resulting density is higher than the density of the water and consequently its impact force increases noticeable. Debris flow dynamic depends mainly on the slope and the shape of the torrent bed, the flow rheology and the solid volumetric concentration (C_{sv}). C_{sv} is defined as the ratio between the sediment volume and the total volume. For debris flow the C_{sv} is in the range of 0.25 – 0.7 (Hungr et al., 2014); for values lower than 0.25 they are defined as bed load sediment transport, while if the ratio is higher than 0.7 are classified like landslides (Church and Jakob, 2020). Typically, debris flows have a characteristic shape: the higher quantity of the sediment with big boulders is present in the front, followed by the body composed by water and sediment more or less in the same quantity and the tail with a lower C_{sv} value (Pierson, 1986).

Snow avalanches are snow masses that rapidly descend steep slopes (Schweizer et al., 2003). They can contain or entrain along the path rock, soil, vegetation, or ice. There are mainly two types of snow avalanches: loose snow and slab avalanches (Quervain de, 1966). Loose snow avalanches are characterized by a relatively cohesionless surface layer of dry snow moving downward. In case of powdery snow, initial failure occurs within a small volume, but as soon this starts moving it suddenly entrains snow material producing a triangular shape on the slope with the apex in the starting point. These types of avalanches can

be very destructive and may also trigger big slab avalanches (Perla et al., 1980). The mean thickness of the disconnected layer is not very high (around 0.5-1.0 m). The second category includes the release of a cohesive slab over an extended plane of weakness. Areas of shear fracture along the plane of weakness may range between 10^2 to 10^4 m^2; thickness of the slab layer can easily be larger than 1 m (Perla et al., 1980). Once in motion the slab may entrain additional mass increasing the magnitude of the flow (Sovilla et al., 2007). However, the original extent of the disconnected layer makes slab avalanches more dangerous and characterized by a higher impact force than loose avalanches. The contributing factors to the release of snow masses are essentially five: terrain, precipitation (especially new snow), wind, temperature (including radiation effects) and snowpack stratigraphy (Schweizer, 2003).

For their composition and dynamic debris flows and snow avalanches are extremely dangerous mass movements. A way to predict their movements is the use of computational models. Models can be divided in two main categories, empirical and physically based models. The firsts are models based on an extensive observation and collection of parameters on documented events trying to find correlation between these variables. This approach does not aim to understand the physics of these phenomena but it just develops statistical relations in order to calculate parameters to assess the potential impact areas of these events. Physical models, instead, aim to predict the motion of mass flow moving over a certain topography. They use a set of equations to describe the flow for each time-step and computational element of the grid. Depending on the adopted set of equations, physical models want to reproduce the dynamic of the mass from a physical point of view with the most rigorous approach.

Different physical based models have been developed to reproduce the propagation of mass flows from a defined starting point through a digital elevation model representing the original topography. The reliability of the models is constantly increasing thanks to data collection of observed mass flow events and the increase in computer performance. Thanks to new data (laboratory experiments and field observations), the mechanics (or dynamics) of mass flows can be better understood, represented and then incorporated in physical models, while the increase of computer performances allows the implementation of a larger system of equations and a higher spatial computational resolution. Moreover, observed data are extremely useful to test models and to assess their performance in reproducing a particular mass flow event. Different sources of uncertainty are still present in models and their reduction is of high interest for civil authorities in order to increase the delineation of possible impact areas and/or to specifically design mitigation structures and/or warning systems.

The input volume represents one of the main sources of uncertainty. Mass flow models require as input a release mass that in the case of snow avalanches is represented by a map of the release heights while for debris flows by an input hydrograph. The evaluation of the volume propagating along a given topography is not straightforward since it can be extremely variable due to local conditions especially in case of high return period (100 – 300 years) event under prediction. In other cases, the estimation of the mass could result difficult due to changing and infrequent particular local conditions (i.e. land cover changes).

Furthermore, additional processes related to the propagation of the flow can significantly increase-decrease the volume of mass flows, successively influencing their dynamic. Such processes are mainly, bed erosion, bank collapse, structure failures, interaction with vegetation and mitigation structures. The volume involved in a mass flow event is a key parameter for the propagation of a certain type of mass flow. The volume can ideally represent the potential energy involved in snow avalanches and debris flows. Normally, greater is the initial/released volume higher is the impact of the event on the valley areas. In such sense, an accurate quantification of the input volume and the implementation of reliable release and entrainment/deposition processes are highly relevant factors to improve the quality of model results.

1.2 State of knowledge

The study focuses on the dynamic and the prediction of rapid mass flows through simulation models. Rapid mass flows are characterized by rapid movements with mean velocities in the range of from 1 to 10^2 m s^{-1} in which the mass is made up of solid grains and intergranular fluid (Iverson and Vallance, 2001). Mass flows consist of an element or a mix of them as rock, ice, stone, granular material and water moving over a certain topography driven by gravity. For their composition and for the speeds that they can reach, they are responsible for several damages and fatalities worldwide (Badoux et al., 2016). These events are commonly known as rock, ice or snow avalanches, debris flows, debris floods, mud flows and rapid earth flows.

Regarding debris flows, the path is characterized by an initiation, transport, and deposition zone. Regarding the generation of such phenomena mainly two processes can be identified. Debris flow can be triggered by landslides (especially in poorly-sorted soils where the fraction of silt and clay is lower than 30-40%) (Ellen et al., 1982) or in channel beds due to high surface water flow that mobilize the loose debris and entrains it, progressively increasing the solid concentration (Griffiths et al., 1997). The latter process depends on the channel slope, the availability of loose material and of a threshold of water discharge able to produce a certain value of shear force (Berti and Simoni, 2005; Takahashi, 2000). Once the flow is in motion, debris flows show a typical shape. In the front part, there are the biggest boulders and the flow height presents its maximum value as well as for the solid volumetric concentration. After the front passage, the flow depth gradually decreases and the solid volumetric concentration too. Also in the propagation phase, debris flows can entrain additional sediment volume material from the channel bed and banks as observed in several studies (Berger et al., 2011). Depending on local geological (sediment composition, depth of bed rock) and topographical (slope, channel width) conditions, entrainment could be very intense causing a great increase in mass volume and consequently in impact forces. For the Alp region extreme observed erosion rates for channel length are in the range of 50-100 $m^3 m^{-1}$ while extreme values of 300 $m^3 m^{-1}$ are recorded worldwide (Rickenmann et al., 2003). The simulation of bed erosion has been incorporated in some mass flows routing models through empirical laws and process-based models. The firsts consist of relations easy to use for practical purposes and they are based on an erosion rate (Chen et al., 2006; Egashira and Ashida, 1987).

Differently, process based models aim to represent the processes involving bed destabilization, erosion and entrainment through a set of equations (Crosta et al., 2015; Pudasaini and Fischer, 2016). Despite the proposed models, the simulation of debris flow erosion is still a challenging objective because of the presence of several factors influencing the dynamic of erosion and entrainment (Pudasaini and Fischer, 2020). A new promising physical based model has been proposed by Pudasaini and Krautblatter (2021) with the aim to physically represent the erosion and deposition of multiphase mass flows. Even if the importance of erosion and entrainment processes are widely recognised, an accurate implementation and calibration of erosion flow parameters to improve their representation in simulation models is still an open research question, biased furtherly by the fact that the bed/terrain strength of the layer under erosion can be highly variable both in depth, and crosswise and longitudinally respect to the flow direction.

A way to contrast bed destabilisation and consequently reduce debris flow erosion and entrainment is the building of mitigation structures. Consolidation check dams are the most common type of mitigation structure used in mountain channels (Piton and Recking, 2014). They are transversal structures usually constructed in series with the aim to reduce the slope of the channel, stabilize the bed and banks, reduce the sediment transport and the flow speed and decrease the pulsing behaviour (Zeng et al., 2009). Regarding the alpine region most of the check dams have been built in the past (mainly between 1800-1900) and nowadays are facing problems of deterioration and functional deficiencies and some of them required forthcoming maintenance operations. In this context, the high number of check dams and their remote access indicate a probable future increase of the propensity to collapse (partially or totally), particularly in case of high magnitude debris flow/flood events. These events are rare but they may occur as observed in some cases (Benito et al., 1998; Cucchiaro et al., 2019). The effect of check dam failure is the release of the retained volume and the possible overall destabilization of the channel bed behind the structure. The available material can be easily entrainable by the flow, increasing its flow volume and its momentum. The effects are the increase of the peak discharge and the extent of impact areas. Therefore, the prediction of such catastrophic events is necessary to update the hazard map in those basins where check dams are becoming less stable or to provide indications of residual hazard. Actually, just a few studies reproduced the effect of check dam collapse with numerical models, but none of them adequately represented the effect of the release mass retained by the structure and the successive erosion and entrainment processes.

Regarding snow avalanches the impact area can be divided in three reaches similarly to the debris flows. The triggering area is where the avalanche starts due to particular snow cover conditions, the transport one is where the flow transfer the initial mass to a depositional zone. Along the transport area, depending on the type of snow avalanches, the flow may increase in volume through entrainment (Sovilla et al., 2006). Differently from debris flow the erodible layer is represented by the height of the snow cover, therefore the entrained volume respect the initial sliding volume is less influent to the flow runout. In such sense more efforts should be placed on the identification of the possible release area (PRA) and the evaluation of the slab height. The identification of PRA on open slopes where vegetation is absence was widely studied and different semi-automatic algorithms have been implemented (Bühler et al., 2013; Veitinger et al., 2016).

Most of them consider the forest as a binary layer where the user can only indicate the presence or absence of forest. However, vegetation interact with the snow cover in different ways in accordance with biomass characteristics and it can effectively stabilize the snow preventing the release of snow avalanches (Bebi et al., 2021). Some studies are now trying to efficiently assess the role of the different types of vegetation and especially the shrub, sparse, young and disturbed forest (Brožová et al., 2020; Schönenberger et al., 2005). The quantification of the vegetation effects is important in a climate change context, since in the alpine region forests are expected to increase in altitude and established in new areas. At the same time also disturbances as wildfires, storms and insect outbreaks are increasing (Schlögel et al., 2020). Therefore, there is the need for the hazard mapping to adequately assess areas where vegetation is present but not represented by dense forest (crown cover density > 80%) for an accurate delineation of PRA and an assessment of the potential slab depth. A better assessment of the potential volume of snow avalanches starting in vegetated areas employs a better estimation of their dynamic through numerical models. Furthermore an accurate evaluation of the vegetation cover is also crucial for simulations of snow avalanches impacting vegetated area (Teich et al., 2014). In particular, sparse and dense forests can noticeably reduce the runout distance and the maximum impact pressure of small and medium snow avalanches.

1.3 Objectives of the study

Different models resulted suitable to reproduce the propagation of mass flows. Input volume together with mass flow – topography interaction are factors and processes affecting the reliability of mass flow simulations and consequently the delineation of possible impact areas. Simulated volume and the flow – topography interaction are considered the most important factors influencing mass flow model outcomes, consequently affecting the predicted flow velocity, impact force, and runout distance. Therefore, a correct estimation of flow volume and related processes leads to a better estimation of simulated flows. Some gaps of knowledge exist and the study aims to fill some of them. The investigation focuses on two types of mass flows: debris flows and snow avalanches. Regarding debris flows, the study has the objective to improve the reliability of mass flow models to capture the increase in flow volume through channel bed erosion and mitigation structure collapse. As to snow avalanches, the study wants to improve the identification of possible avalanche release areas taking into account the role of different types of vegetation structure. Since different variables affect the assessment of these processes, a further objective is to propose new methods that are applicable also outside the study areas in order to be effectively used by a wide range of stakeholders and public authorities, which are involved in the management cycle of the natural hazards.

1.4 Structure of the thesis

The thesis is a collection of four scientific articles, resulting from the three years of the doctoral period. Three articles have been already published on high impact peer-review scientific journals (chapters 2, 3 and 4), while the fourth is currently under review (chapter 5).

The first paper reports a well documented high magnitude debris flow event occurred in the rio Gere catchment (near Cortina d'Ampezzo, IT). Thanks to pre- and post-event data a function linking terrain slope and erosion parameter has been calibrated and it can be used to improve debris flow simulation on erodible channels. The manuscript entitled *Advances in the simulation of debris flow erosion: The case study of the Rio Gere (Italy) event of the 4th August 2017* was published in *Geomorphology* in 2021.

The second paper defined a procedure to simulate the effect of check dam collapse in a debris flow event. The developed methodology was assessed in a debris flow channel where an extreme event caused the collapse of a series of check dams. The methodology can be straight applied to map the residual risk in mountain channels or where the lack of maintenance may decrease torrent countermeasure stability. The manuscript is entitled *Simulating the effect of check dam collapse in a debris-flow channel* and it was published in *Science of the Total Environment* in 2021.

The third paper focuses on terrain roughness. We tested seven different algorithms to compute terrain roughness in order to identify which one is capable to represent in the most appropriate way the features on the ground (rocks, forests, etc.) that interact with natural hazards. The outcomes can improve the reliability of mass flow propagation models over natural areas and the assessment of the input volumes. The manuscript entitled *Multiscale analysis of surface roughness for the improvement of natural hazard modelling* was published in *Natural Hazards and Earth System Sciences* in 2021.

The fourth paper analyses the protection capacity of forests hit by windstorms. With multi-temporal observations we developed and tested two new algorithms to assess the protection capacity of abated trees. Results assessed the time of minimum level of forest protection against snow avalanches since the storm event and the possibility to apply the proposed methodology at regional scale for management and monitoring purposes. The manuscript entitled *Assessment indices for snow avalanche protection of wind-disturbed forests* is currently under review in the journal *Ecological Engineering*.

2 Advances in the simulation of debris flow erosion: the case study of the Rio Gere (Italy) event of the 4th August 2017

Tommaso Baggio[1,*], Martin Mergili[2,3], Vincenzo D'Agostino[1]

[1] *Department of Land, Environment, Agriculture and Forestry, University of Padua, via dell'Università 16, 35020 Legnaro (PD), Italy*

[2] *Cascade – Mountain processes and mountain hazards, Institute of Geography and Regional Science, University of Graz, Heinrichstraße 36, 8010 Graz, Austria*

[3] *Institute of Applied Geology, University of Natural Resources and Life Sciences (BOKU), Peter-Jordan-Straße 70, 1190 Vienna, Austria*

This chapter has been published in *Geomorphology* in 2021

2.1 Abstract

Debris flows are natural hazards causing fatalities and damages to infrastructures every year. One of the current challenges is to improve the predictability of such events using simulation tools. In this direction, the paper aims to model debris-flow generation starting from the water component and then simulating the motion of the bulked solid-fluid mixture mass flow. The debris component is progressively increased through entrainment of the channel bed material. The simulation has been performed exploiting the tool r.avaflow, which implements a physically-based model (Pudasaini and Mergili, 2019) for the flow propagation and an empirical multi-phase model for the entrainment processes.

The investigated study case occurred in the Northeastern Alps of Italy, near the town of Cortina d'Ampezzo (Veneto Region), during the summer of 2017. The debris flow was triggered by a heavy rainstorm that caused extreme surface runoff, leading to entrainment of sediment from the channel bed. The debris flow obstructed the bridge of a regional road and consequently flooded the adjacent areas.

Different types of debris flow simulations are performed, testing four specific functions to compute the entrainment rate. The simulated results are then compared against field observations. The analysis considers the differences in volume and depth of entrainment and in the output hydrograph.

We conclude that entrainment is correlated with the terrain slope, particularly if it is calculated on a smoothed digital elevation model, which dilutes a less significant local steepness. We calibrate a spatially distributed slope-dependent erosion coefficient that successfully reproduced the observed entrainment volumes. The outcomes highlight the great importance of simulating debris flow entrainment processes adopting a multiphase model, which resulted particularly suitable for an accurate reproduction of the investigated event. The results, corroborated by further verifications, can improve the reliability of challenging predictive simulations on debris flow erosion.

Keywords: Debris flows; Entrainment; Propagation modelling; Multi-phase flow

2.2 Introduction

Debris flows are gravity-driven mass movements composed of a mixture of water and sediment particles of various sizes (from clay to boulders), moving down through a defined topography (Coussot and Meunier, 1996; Hutter et al., 1994; Jakob et al., 2005; Pudasaini et al., 2005). The motion of such phenomena is influenced by both solid and fluid forces, distinguishing debris flows from related geomorphological processes such as rock avalanches and sediment transport through water floods (Hungr et al., 2014; Iverson, 1997). Debris flows are often characterized by high flow velocities, high impact forces and long runout distances, and represent one of the most hazardous landslide types (Hutter et al., 1996; Jakob et al., 2005; Takahashi and Das, 2014). To predict the necessary parameters for hazard and risk mapping, different simulation tools have been developed in recent years. Most of them are based on single-phase models, in which the solid and fluid phases are considered as a mixture (Bartelt et al., 1999; Grigorian et al., 1967; Iverson, 2012; Sampl and Zwinger, 2004; Savage and Hutter, 1989; Voellmy, 1955), while only a few consider the two components separately (Armanini et al., 2009; Gregoretti et al., 2018; Pitman and Long, 2005; Pudasaini, 2012). Some of these numerical models are implemented in simulation tools and used to map and define hazard areas. Examples of such tools are DAN (Hungr, 1995), FLO-2D (O'Brien et al., 1993), LAHARZ (Iverson et al., 1998), TITAN 2D (Pitman and Long, 2005), SAMOS-AT (Sampl and Zwinger, 2004), RAMMS (Christen et al., 2010), or TRENT–2D (Armanini et al., 2009; Rosatti and Begnudelli, 2013). These simulation tools can mainly reproduce the propagation through a defined topography of a mass flow starting from a release area (in the case of landslides or avalanches) or alternatively from an input hydrograph (for debris flows or floods).

A current research challenge consists in the reliable simulation of the generation, propagation and deposition of debris flows. Regarding the generation and development of debris flows, threshold conditions in terms both rainfall and runoff amounts are fundamental (Pastorello et al., 2020). Two main processes can be identified, depending on the material characteristics. In poorly-sorted soils where the fraction of silt and clay is higher than 30-40%, debris flows are mainly triggered by shallow landslides in combination with high surface runoff (Baum et al., 2011; Ellen et al., 1982; Kean et al., 2013). In other cases, extreme water flux in a channel can destabilize its bed and banks (Berger et al., 2011) and progressively entrain granular debris, increasing the solid concentration of the flow (Griffiths et al., 1997). The latter process depends on the channel slope, availability of loose material and the exceedance of a water discharge threshold able to exert a certain shear force (Berti and Simoni, 2005; Takahashi, 2000). Moreover, once a debris flow has been triggered it can erode and entrain new debris (Iverson, 2012; Jakob et al., 2005; Reid et al., 2011), increasing its momentum and consequently runout distance and impact force (Iverson et al., 2011; Pudasaini and Fischer, 2020). Bed incision can reach depths of a few metres, or more, leading to a noticeable increase in the transported volume and peak discharge (Berti et al., 1999; Jakob et al., 2005; Pirulli and Pastor, 2012). Particularly if the bed slope increases beyond 10°, the flow can destabilize the channel path (Bagnold, 1966) and sediments can be mobilized and entrained into the flow.

Two types of erosion models have mainly been developed to take in account the increase in destructive potential of the flowing mass: empirical and process-based ones. Empirical laws are easy to use for practical purposes, and they are generally based on an erosion rate, that is time dependent rate of entrained material at the interface between flow and channel bed (Chen et al., 2006; Egashira and Ashida, 1987; McDougall and Hungr, 2005; Takahashi et al., 1992; Takahashi and Kuang, 1986), or on a yield rate (mean entrained volume for channel length unit) (Hungr et al., 1984; Rickenmann et al., 2003). Differently, process-based models consider the physical understanding of exchanges between the flow and the erodible bed (Armanini et al., 2009; Crosta et al., 2015; Fraccarollo and Capart, 2002; Iverson, 2012; Pudasaini and Fischer, 2020). In spite of that, the simulation of debris flow erosion processes still remains a challenge due to the spatial variation of the entrainable material, complex dynamics of such flows and their rheology at the interface layer (Pudasaini and Fischer, 2020). Even if erosion processes are not completely physically understood they should be considered in debris flow simulations, since they noticeably increase the magnitude, runout distance, and impact force of such gravitational flows (Berger et al., 2011; Han et al., 2015; Rickenmann, 2007; Takahashi et al., 1992). Moreover, erosion models should account for the biphasic nature of debris flows, in order to simulate debris flow propagation in the most reliable way (Pudasaini and Fischer, 2020).

The computational tool r.avaflow (Mergili et al., 2017) includes an enhanced version of the Pudasaini and Mergili (2019) multi-phase model and an empirical full multi-phase erosion model. Thanks to these characteristics, r.avaflow is a simulation tool potentially suitable to reproduce the generation of a debris flow event through progressive channel erosion starting from water flux. Although the process-based, fully mechanical multi-phase erosion model presented by Pudasaini and Fischer (2020) could possibly better represent the physics of erosion and entrainment phenomena, for simplicity here we only consider an empirical erosion rate model. Furthermore, it also has the advantage of a more flexible calibration as to a real case study.

In this paper we evaluate the applicability of the simulation tool r.avaflow to reproduce the generation of debris flow event that occurred in 2017 in the Gere catchment, located near the town of Cortina d'Ampezzo (Veneto, Italy). In detail, we test different ways to set up the empirical modelling of erosion implemented in r.avaflow, varying the coefficient of erosion as a function of the terrain slope. We also calibrate a function to calculate the erosion coefficient as an input map for the simulation tool r.avaflow, based on the erosion observations of the 2017 Gere event. Moreover, we evaluate this new model erosion setup against the default method that fixes the erosion coefficient through the whole computational area. Lastly, we compare the different simulation results, analysing the entrained volume and the output hydrograph.

2.3 Study area and debris flow event

The analysed event occurred in summer 2017, near the town of Cortina d'Ampezzo located in the province of Belluno (Italy). During the night between the 4th and 5th August 2017, a heavy rainstorm event hit the Bigontina catchment, producing a large amount of surface runoff, consequently triggering a debris flow and intense bed load transport, leading to one fatality and flooding the village of Alverà.

The Bigontina catchment has a surface of 17.5 km^2 extending from 3221 m a.s.l. (summit of Cristallo peak) to 1150 m a.s.l. at the confluence with the Boite river near Cortina d'Ampezzo (Figure 2.1). Rio Gere, the alpine stream that produced the debris flow event under investigation, is located in the upper part of the catchment. The Rio Gere joins the Bigontina channel at an elevation of 1650 m a.s.l., just downstream from the bridge of the regional road connecting Cortina d'Ampezzo with Misurina. After the confluence with the Bigontina channel, the thalweg slope of the channel becomes gentler, but the 2017 event still maintained enough energy and turned in a debris flood event (Church and Jakob, 2020), evident by the debris deposit upstream the village of Alverà.

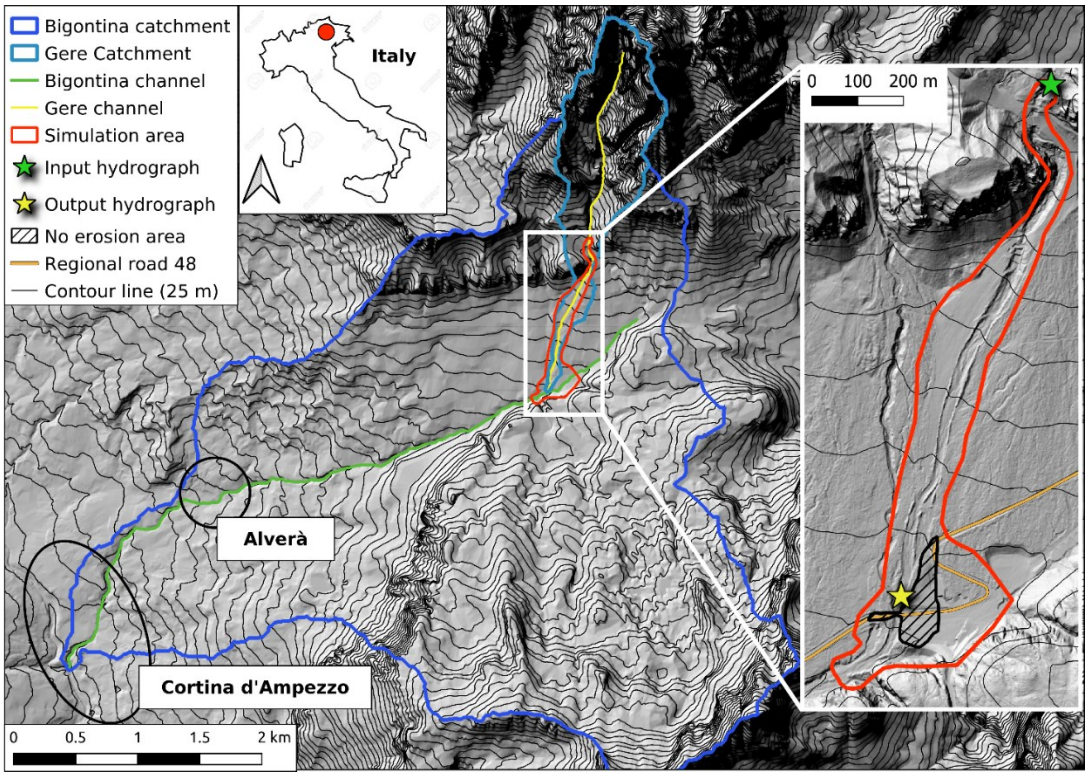

Figure 2.1: Overview of the Bigontina catchment (elevation difference between contour lines: 25 m). The no erosion area (black polygon) represents the parking lot, the bridge of the regional road and the chairlift station.

In this paper we analyse the debris flow event triggered and propagated in the Rio Gere basin (Figure 2.1 and Figure 2.2). The analysed catchment has an area of 1.68 km^2 and a mean slope of 42°. The main channel is 3276 m long and has a mean slope of 19.9°. The relative Melton number (1.19) is consistently higher than the value of 0.5 identified as the threshold for debris flow-prone catchments in north eastern Italy suggested by D'Agostino (1996), meaning that the Gere basin has the morphological characteristics to

produce mature debris flows. The basin can be divided into two morphologically and geologically homogeneous parts. We define the basin part with an elevation above 1921 m a.s.l. (elevation of the input hydrograph, Figure 2.1, 0.94 km^2) as the "high Gere" catchment and the remaining part (0.74 km^2), down to the confluence with the Bigontina channel, as the "low Gere" catchment. Both areas are formed by dolomite rocks. The "high Gere" consists of steep slopes and near-vertical walls (mean slope 62.2°). The rock channel network is deeply incised into the bedrock (main channel length 1375 m and mean slope of 25.2°), except for a 400 m channel section located upward the input hydrograph point, where the channel bed and banks are formed by loose sediment. The "low Gere" is less steep (the mean catchment and channel slope are 29.3° and 10.9° respectively) and consists of open slopes as consequence of past weathering breakage processes and glacial debris transport. The channel passes through colluvial deposits and is well defined by banks 2 - 5 m high for the first 450 m downward the input section. Towards the confluence, the channel path becomes rather diffuse and is characterized by loose debris deposits. This sediment can therefore be quite easily mobilized during intense rainfall events. The mean grain diameter surveyed in the lower part of the Gere channel bed after the reported event is 87.2 mm (range: 3.8 – 1019 mm) (D'Agostino et al., 2018).

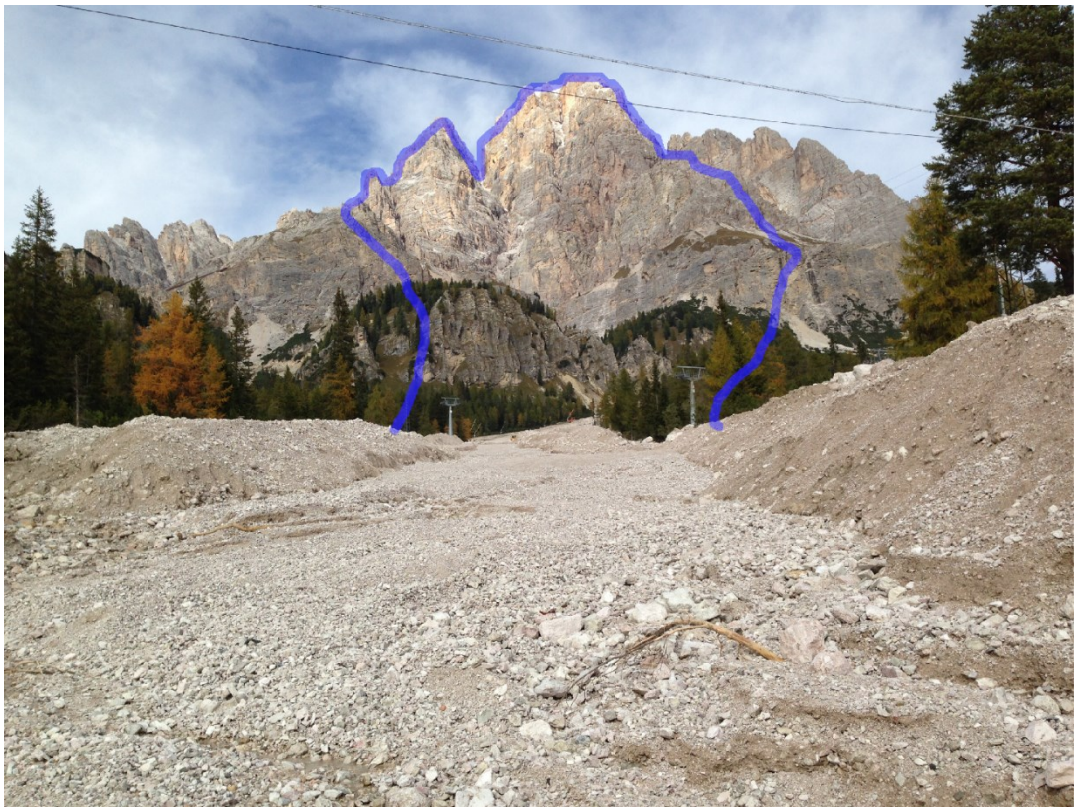

Figure 2.2: Photo of the Gere catchment, captured 200 m upward from the confluence with the Bigontina channel toward the watershed border. The blue line represents the watershed line. Photo taken by Francesco Bettella (University of Padova) on 10th April 2017.

The analysed debris flow event took place during the evening of the 4th August 2017. The rainfall event had a total duration of three hours characterized by two major peaks. The nearest weather station (Misurina, 3.5 km to the east) recorded a total amount of 110 mm between 10.00 p.m. and 12.00 p.m. of the 4th August with two peaks of 10.8 mm/5min and 10.5 mm/5min respectively at 10.10 pm and 11.40 pm (local time). The intense runoff in the Gere catchment triggered a debris flow through entrainment of debris from the bed and banks.

2.4 Material and methods

2.4.1 The simulation tool r.avaflow and the empirical erosion model algorithm

To back-calculate the described event we use the simulation tool r.avaflow, which is able to reproduce rapid mass flows and process chains starting from a defined area down to a deposition zone (Mergili et al., 2017). r.avaflow is a raster module of GRASS GIS 7 (GRASS Development Team, 2021) and is completely open source and freely available at Mergili and Pudasaini (2020). The tool includes two different models: a single-phase shallow water model with Voellmy friction relation (Christen et al., 2010; Fischer et al., 2012) and the Pudasaini and Mergili (2019) multi-phase model with ambient drag (Kattel et al., 2016). The simulation tool is wrapped in Python (data management, pre- and post- processing tasks), while the core of the flow propagation algorithm is implemented in the C programming language. R (R Core Team, 2020) is employed for the validation and visualization functions. The multi-phase mass flow model can simulate the propagation of three different components: solid, fine solid and fluid. Each of them has a specific physical behaviour as described in Pudasaini and Mergili (2019). For this case study we represent the debris as solid component and the water fraction as fluid.

The essential inputs of r.avaflow are a digital terrain model (DTM), the solid and fluid release heights or hydrographs and a set of values describing the flow rheology. Moreover, six specific optional complementary functions are implemented in r.avaflow: conversion of release heights into release depths, diffusion control, surface control, entrainment, stopping and dynamic adaptation of friction parameters.

Focusing on the entrainment model, the algorithm implemented in r.avaflow is based on an empirical multi-phase model. Considering the multi-phase model applied with two phases, the potential fluid and solid entrainment depths ($D_{E,f}$ and $D_{E,s}$ [m]) are expressed as a function of the fluid and solid momentum (M_f and M_s [kg m s^{-1}], fluid/solid mass multiplied by its mean velocity), based on a user-defined empirical erosion coefficient (C_E [kg^{-1}]). The solid fraction ($\alpha_{s,Emax}$) of the entrained material is defined by the user as a fixed number. Alternatively, it can be spatially varied throughout the computational region.

$$D_{E,s} = C_E \left| M_s + M_f \right| \alpha_{s,Emax} \Delta t \qquad (2.1)$$

$$D_{E,f} = C_E \left| M_s + M_f \right| \left(1 - \alpha_{s,Emax}\right) \Delta t \qquad (2.2)$$

The solid and fluid entrained depths are added to the flow after each time step and the basal topography (represented by a DTM) is updated at the same time. Flow momenta are updated accordingly. The maximum depth of entrainment can be defined by the user as a raster map.

In this study we use the r.avaflow model (version 2.2), where entrainment is considered as a complementary function of the multiphase model of Pudasaini and Mergili (2019).

To highlight how the erosion model works within r.avaflow, a simple demonstrative debris flow scenario is reproduced. Eleven simulations are performed reproducing a hypothetical debris flow, propagating on a computer-generated hillslope. The topography is represented by a uniform slope, 500 m long with a grade of 0.20 m/m; the channel has a width of 20 m and is delimited by two levees 5 m high. The input hydrograph has a triangular shape, starting with a discharge of 20 m^3/s, reaching a peak of 100 m^3/s after 160 s, decreasing to 20 m^3/s and stopping after 320 s. The input solid volumetric concentration is set to a constant value of 0.5; the total input volume amounts to 19,240 m^3. The eleven simulations are performed on this scenario, progressively varying the erosion coefficient in a range between $5 \cdot 10^{-8}$ and $2 \cdot 10^{-6}$ kg^{-1}. The simulated entrained volumes are then normalized for the channel length and width (eroded volume per unit of channel width and per unit of channel length), obtaining a normalized mean erosion depth (De_n) that is reported in Figure 2.3. De_n has a power trend approximated by equation (2.3).

$$De_n = 2.51 \cdot 10^7 \cdot {C_E}^{1.26} \qquad (2.3)$$

From this scenario it is possible to detect that entrainment is significant ($De_n > 0.15$ m) for values of C_E greater than $3 \cdot 10^{-7}$ kg^{-1}; the upper C_E limit could be detected between $2 - 3 \cdot 10^{-6}$ kg^{-1} corresponding to a mean De_n of 1.6 – 2.8 m.

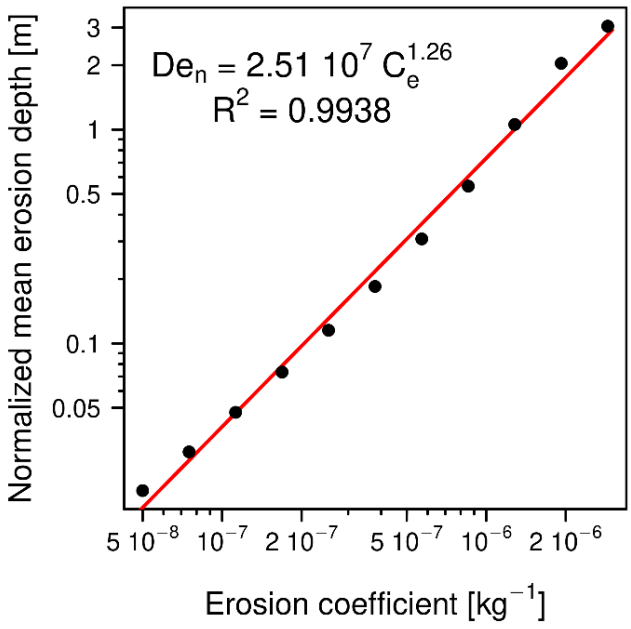

Figure 2.3: Results of the sensitivity analysis of the normalized mean erosion depth to the erosion coefficient. The x and y axes are displayed in logarithmic scale.

2.4.2 Topographic information and simulation input data

To perform a debris flow simulation with entrainment in r.avaflow, the following data have to be set up as input: DTM, input hydrograph, flow and entrainment parameters. Moreover, to assess the performance of the simulation model we use a post-event LiDAR based DTM.

The pre-event DTM is derived from a LiDAR survey performed in 2009. It has a spatial resolution of 1m. The point cloud was produced within the PST-A programme (extraordinary Italian plan of remote sensing). We obtained the already processed raster-based DTM from the Italian Environmental Ministry. The vertical and planimetric errors are 0.15 and 0.30 m respectively. The DTM is successively resampled to a resolution of 2 m, using a mean value method, in order to reduce the computational time. The DTM is also modified to represent the obstructed bridge on the regional road SR48. We consider the bridge as a filter of an open check dam for sediment retention, for which the quasi-total trapping condition occurs when $B_{min}/ D_{DF} < (1.5 – 2)$, where B_{min} is the minimum filter dimension (vertical or horizontal dimension) and D_{DF} the maximum boulder diameter of the debris flow (D'Agostino, 2010). In this case B_{min} and D_{DF} are 1.60 and 1.01 m, leading to a complete obstruction of the opening. For this reason, the cells representing the river bed in the location of the bridge are raised to the elevation of the road.

After the debris flow the whole area of the Bigontina catchment was surveyed through a LiDAR campaign on 26th October 2017. The vertical accuracy is 0.051 m (root mean square error of seven ground control points surveyed with a RTK-GPS) and the mean point density is 10 pts/m^2. From the LiDAR data, the DTM (1 m resolution) is computed using a kriging method (Oliver and Webster, 1990), representing the post-event conditions. Thanks to the availability of the pre- and post-event DTMs we compute the DEM of Difference (DoD). We adopt a simple minimum level of detection approach (Brasington et al., 2000; Fuller et al., 2003), assuming a uniformly distributed error. Difference values lower than the minimum level of detection are not considered in the DoD analysis. The individual errors in the DTMs are propagated in the DoD as the root of the square DTMs' error sum (Brasington et al., 2003).

The resulting area of interest for the simulations is shown in Figure 2.1. The computational domain has an extent of 0.183 km^2 corresponding to 44,700 computational cells. The length of the simulated channel is 1483 m with a vertical height drop of 266 m (from 1920 m a.s.l. to 1654 m a.s.l.). The mean channel slope is 10.2°, varying along the channel path: the upper part (the first 500 m downstream from the input hydrograph) has a mean slope equal to 13.6° while the rest of the path has a mean slope of 8.3°.

The position of the input hydrograph is shown in Figure 2.1. It is placed in that location in order to simulate the observed erosion process which occurred downstream. The liquid discharge is calculated from the radar measurement of the precipitation in the "high Gere" catchment. The data were acquired by the meteorological station at Monte Macaion (province of Trento, IT), at a distance of 75.5 km from catchment in W direction. The original reflectivity volume scans are elaborated using correction algorithms able to diminish the impact of errors due to (i) radar hardware mis-calibration (Marra et al., 2014), (ii) partial beam blockage (Pellarin et al., 2002), and (iii) signal attenuation due to heavy rain (Marra and Morin, 2015,

2018). Radar reflectivity (R) is converted to rain intensity (Z) following a power-law relationship in the form $Z = 308 \cdot R^{1.5}$, well suited for convective precipitation in the area (Anagnostou et al., 2010), and projected to a 1 km grid. Finally, radar estimates are compared with in-situ rain gauge measurements from 3 stations, and adjusted to remove the residual mean field bias (Marra et al., 2014).

After the rainfall assessment, the FLO-2D (O'Brien et al., 1993) two-dimensional flood routing model is used to calculate the fluid hydrograph at the starting location. The SCS - CN (Soil Conservation Service - Curve Number) (Mishra and Singh, 2003) method is adopted to compute the surface rainfall runoff generation together with the model equations for flow propagation as reported in O'Brien (1986). The input data are (i) the DTM (cell size of 20 m); (ii) the initial abstraction (considered equal to 5% of the potential maximum retention); (iii) the Curve Number CN (we used CN at the Antecedent Moisture Conditions AMC III, since the soil was already wet before the event) derived from the combination of the land use-land cover and the hydrological soil group map; (iv) the Manning's surface roughness derived from the land cover map; (v) the radar derived precipitation rainfall intensity (temporal resolution of 5 min and cell size of 20 m, resampled with the natural neighbour algorithm from the 1 km resolution grid). We used an average on the weighted area to derive the CN and the Manning values, that resulted equal to 75.3 and 0.053 respectively (the lithological, land cover maps and tables used to calculate the CN value and the Manning number are reported in D'Agostino et al. 2018). The model calculates two major discharge peaks of 14.48 and 13.02 m^3/s; according to this simulation the time between the two peaks is 64 minutes (D'Agostino et al., 2018). Since it is not possible to validate the modelled peak water discharge in the field, due to the bedrock channel morphology, we compare it with (i) the empirical relation of Forti (1920) for extreme events and (ii) the rational method (suitable for small alpine catchments (Grimaldi and Petroselli, 2015). The first method results in a peak discharge of 13.07 m^3s^{-1}, while using the rational method we derive a peak of 15.80 m^3s^{-1}. We adopt here a runoff coefficient equal to 0.8 (Berti et al., 1999) and use a concentration time of 27 minutes coupled with the corresponding mean rainfall intensity of 75 mm/h (according to the above mentioned rainfall data). Through these crossed verifications, we confirm the peak discharge value of the spatially distributed model. The time period between the two major peaks is then cut from the final hydrograph to decrease the computational time, keeping the fluid flow discharge to 3 m^3/s for 300 s (interval: 1100 – 1400 s). Furthermore, 10% of solid content is added to the input hydrograph to reproduce the flux coming from the upper catchment in a more realistic way. The upper part of the Gere catchment stores a consistent amount of debris (particle diameter range: 25 – 100 mm) easily entrainable in the case of an intense rainfall event such as the one investigated. Consequently, it is very likely that the flux at the input hydrograph section already transported a certain quantity of solid particles before the debris flow triggering. The resulting input hydrograph used in the simulations is shown in Figure 2.4.

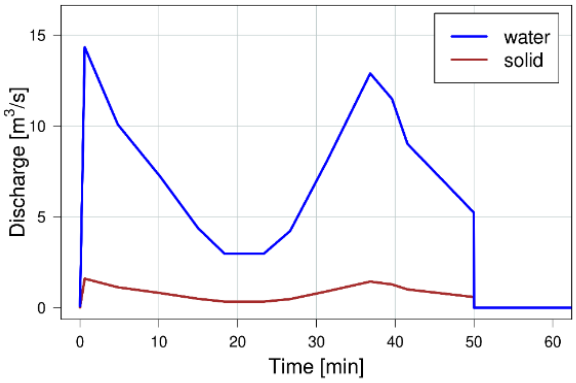

Figure 2.4: Input hydrograph used in the r.avaflow simulations (source: D'Agostino et al., 2018)

The solid and fluid physical parameters used in this case study are shown in Table 2.1. A description of the parameters is reported in Pudasaini and Mergili (2019). The values are not optimized ad hoc for this event because instruments to detect flow depth and velocity are not present along the channel path and cross sections of the path are strongly modified by the passage of the debris flow causing deep erosion and making a reconstruction of the frontal flow depth unreliable. The physical parameters are basically derived from the back calculation of the 2013 Gadria debris flow event (Bolzano, IT) reported in Baggio (2018), in which an accurate calibration procedure was adopted thanks to the availability of real time event flow depth measurements and relative velocities. The parameters differ from the Gadria case in terms of the basal friction angle (δ) and fluid friction coefficient (C_{FF}). These two parameters are slightly modified in order to obtain reliable front flow velocities as observed in other debris flow events that occurred in catchments of the Dolomites (Berti et al., 1999).

Table 2.1: Physical parameters used to perform the simulation in r.avaflow.

Symbol	Physical parameter	Unit	Value
ρ_s	Solid material density	kg m^{-3}	2650
ρ_f	Fluid material density	kg m^{-3}	1000
φ	Solid internal friction angle	Degree	35
δ	Solid basal friction angle	Degree	18
ν	Fluid kinematic viscosity	m^2 s^{-1}	10^{-3}
τY	Fluid yield strength	Pa	0
C_{AD}	Ambient drag coefficient	-	0.02
C_{FF}	Fluid friction coefficient	-	0.05

2.4.3 Observed entrainment

We analyse the erosion depth of each pixel and correlate it with the slope map to verify whether entrainment would depend on the local slope and to obtain a possible correlation between these two variables, and a slope threshold for entrainment. The analysis is performed at the post-event DTM resolution (1 m), dividing the main channel in different reaches 20 m long in order to obtain mean erosion and slope values for each specific channel reach.

Another important use of the DoD is to assess the accuracy of the simulated entrained volumes and entrainment patterns. We investigate the difference between the observed and simulated entrainment patterns. For the whole computational area, we calculate the total eroded volumes and compare them with the simulated ones.

2.4.4 Improvement of the erosion input data

The empirical erosion algorithm implemented in r.avaflow (Equations 2.1 and 2.2) is based on the erosion coefficient that can be set up in the model as a fixed value or a raster map, allowing a pattern of different entrainment rates within the computational region to be created. Together with the erosion coefficient, the model requires the maximum possible height of erosion and the solid fraction of the entrainable material. For the reported event, we fix the maximum erosion height at 8 m, based on the DTM of difference that highlights a maximum erosion height around 8 m (Figure 2.7). In some areas, entrainment is not allowed, corresponding to artificial surfaces (Figure 2.1), representing the regional road, the bridge, the parking area and a chairlift station. We set the solid fraction of the entrainable material to 0.7, considering the saturated soil condition caused by the rainfall preceding the debris flow event.

We test the hypothesis that the erosion coefficient can be calibrated as a function of topographic variables. In the literature the variable that mainly affects the erosion rate is the slope (Jakob et al., 2005; Kronfellner-Kraus, 1984; Rickenmann et al., 2003). In this way we use the observed erosion depths in order to calibrate a function able to link the slope with the input erosion coefficient. We study four different functions to derive the spatial distributed erosion coefficient. The types of functions are exponential, linear, logarithmic and power. In particular, the exponential function allows the prediction of a broad variety of eroded volumes for channel units with different terrain slopes, depending on the chosen parameters. Therefore, we test a total of six exponential functions. The tested functions are summarized in Table 2.2 and shown in Figure 2.5. Moreover, we perform a simulation with a fixed coefficient of erosion for the whole computational region ($C_E = 10^{-6.3}$). The function parameters are selected through preliminary 'best-fitting' simulations in which those parameters are progressively varied. 'Best-fitting' depends on the results of the sensitivity analysis introduced along with the entrainment model. The minimum C_E value, for a slope of 0%, is in the range between $2 \cdot 10^{-8}$ and 10^{-7} kg^{-1}. The maximum value of C_E is fixed at 10^{-6} kg^{-1} which, from Equation 2.3, leads to a normalized mean erosion depth of 1 m.

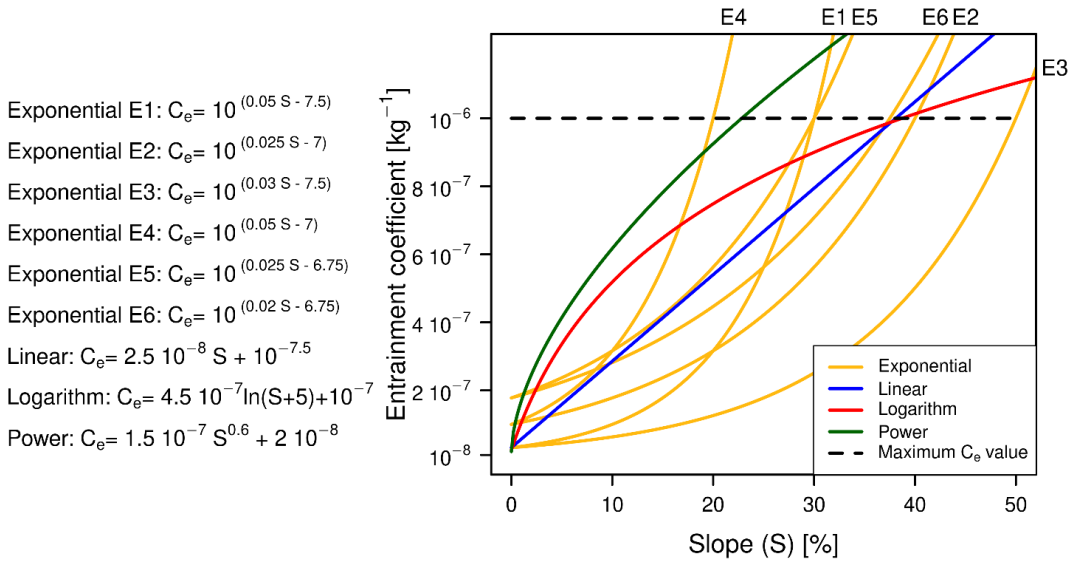

Figure 2.5: Functions used to calculate the spatially distributed erosion coefficient in relation to the slope map.

In this study, we report the 'best' simulations for the following function types: linear, logarithm and power, while all the performed simulations are reported for the exponential function. The slope map to calculate the erosion coefficient is derived from the pre-event DTM. As highlighted in the results of the DoD analysis, we avoid the effect of microtopography, re-sampling the slope map derived from the 1m pre-event DTM to a raster cell size of 10 m and then interpolate it to a final resolution of 2 m, using a bicubic method. This final raster map is used to create the different erosion coefficient maps used in the simulations. To find out which equation better represents the observed entrainment pattern we compare the simulated eroded volumes with the DoD as described in the section 'Observed erosion'. A given simulation is considered accurate if it reproduces the eroded volume within an error of 20% with respect to the observed erosion (derived from the DoD).

Quantification of the increase in debris flow volume and solid concentration due to entrainment is based on the analysis of the simulated output hydrograph located at the lower end of the computational area (the location of the hydrograph is shown in Figure 2.1). At the end, we compare the output hydrographs of those five simulations providing the best performance for each type of erosive map (fixed, linear, power, logarithm, exponential). In this way, we analyse the evolution of the solid concentration at the lower end of the computational domain as well as the related peak discharge. We compare the output hydrographs of the ten different simulations performed with different erosion coefficient maps. In this way we can detect whether the differences in the erosion coefficient map lead to a significant difference between the simulated output hydrographs.

2.5 Results

Firstly, we analyse the patterns of the DoD (propagated error 0.16 m). Figure 2.6(A) illustrates the erosion depths within the computational area. The post-event DTM was recorded on 26th October 2017, 3 months after the investigated event. As shown in Figure 2.6(A), we manage to compute the observed eroded volumes only for two areas (control areas 1 and 2) of the simulated channel path. This is because the material was immediately moved by human activity after the event and before the LiDAR survey. Some places were filled in, others excavated, in order to restore the channel flow and the ski slope for the coming winter season.

The first investigated area is located in the upper part of the computational area (Figure 2.6(A), Control area 1) and corresponds to the right turn of the channel. There, major erosion processes due to bank and bed debris entrainment are observed. The maximum values of erosion depth are in the range between 6 and 7 m. In that reach, the main channel has a total length of 216 m and mean slope of 12.9°. Regarding this control area, the calculated total eroded volume is 17,684 m^3, corresponding to an erosion of 81 m^3 per meter of channel length. The value is so high due to the collapse of part of the external bank in correspondence to the left turn. The calculated volume of the bank failure is 6,970 m^3. Recalculating the erosion per channel meter excluding this volume results in 50 m^3/m.

The second control area is located near the confluence with the Bigontina channel (Figure 2.6(A), Control area 2). In this part, the channel is not confined to a clearly recognizable path, but flows mainly on the ski slope. The considered reach has a length of 423 m and a mean slope of 8.9°. The calculated entrained volume caused by the debris flow event is 13,215 m^3, corresponding to a volume of 31 m^3 per meter of channel length (Table 2.2).

Regarding the deposit, we make an estimation of the debris volume accumulated at the confluence between the Gere and the Bigontina channels. Unfortunately, the 2017 LiDAR was acquired after the anthropogenic movement of the deposited material in order to re-establish the flow passage and so the post-event DTM is not suitable for the volume calculation. However, thanks to helicopter and citizens pictures captured the day after the event, we can identify the debris deposit height relatively to the channel banks. We then fill up the channel post-event DTM for those segments recognised in the pictures and we calculate a total deposit of 13,500 m^3. Such value is just an estimation since it is not derived from a rigorous DoD analysis.

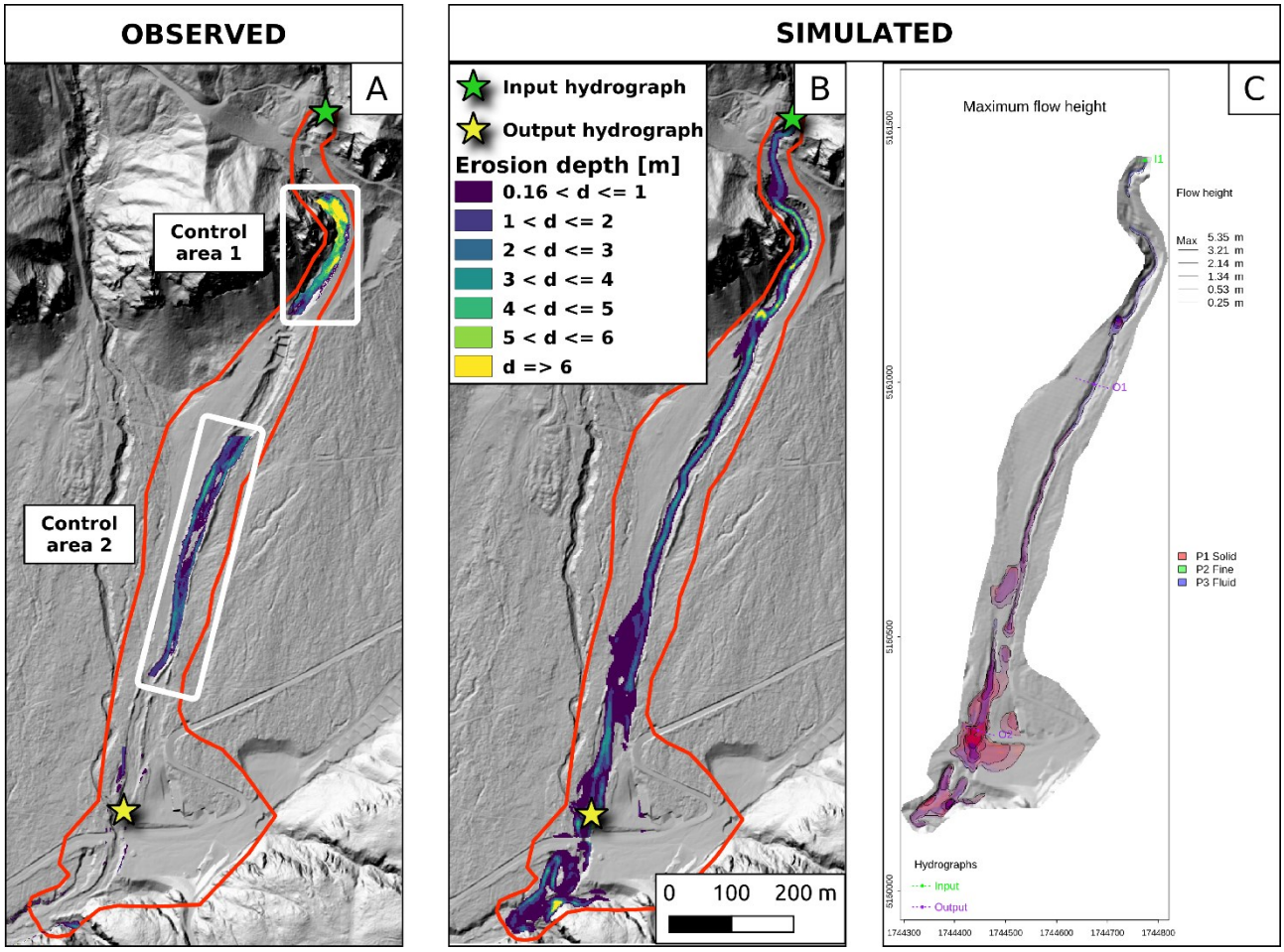

Figure 2.6: Maps representing the observed erosion depths (A), simulated erosion depths (B, results of simulation E6) and maximum flow height for simulation E6 (C). In (C) the eroded material is part of the flow height (values lower than 0.25 m are not displayed).

2.5.1 DOD analysis – pixel scale

Starting from the DoD map (Figure 2.6 A), we analyse the erosion depth (*ED*) at pixel level and correlate it with the local slope. In Figure 2.7 and Figure 2.8 we illustrate the results of this analysis. Figure 2.7 A shows the correlation between the slope and erosion depth at pixel level (1 m resolution). In Figure 2.7 A we simply plot these two variables: the slope is derived from the post-event DTM. The results are widely scattered and it is not possible to identify a significant relationship between these two variables. When substituting the previous slope values with the slope extracted from the map used to calculate the erosion coefficient values (pre-event DTM resampled to a resolution of 10 m and afterwards interpolated to the final resolution of 1 m, using a bicubic method), it is possible to identify a logarithmic trend between slope and erosion depth (Figure 2.7 B). The correlation becomes satisfactory only for slopes steeper than 25%. For slope values around 20% the observed erosion depths appear extremely heterogeneous with several observations of erosion depths between 0 and 3 m.

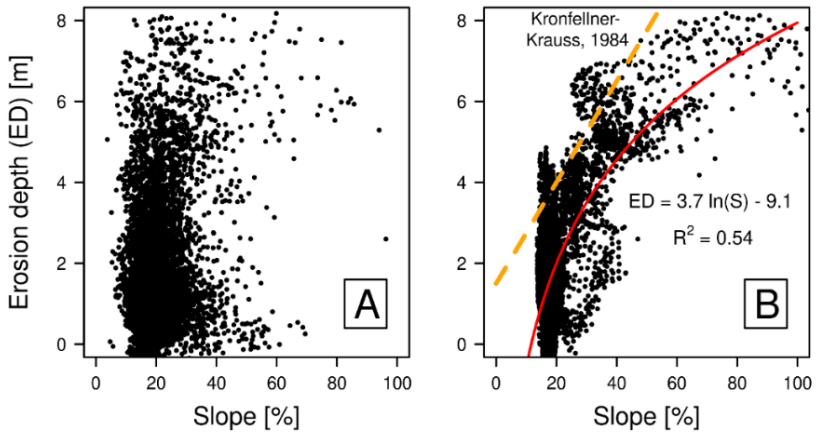

Figure 2.7: Analysis of the slope and observed erosion depth derived from the DoD at pixel level. In plot A we extract the slope from the 1m resolution post event DTM, while in plot B the slope is resampled from the pre-event DTM to 10 m and successively interpolated to 1 m (bicubic method).

2.5.2 DOD analysis – 20m segments of the channel bed

After the analysis at pixel level we focus on erosion of the channel bed in different reaches. To derive a mean value for different reaches of the channel path, we divide it in segments 20 m long for both selected control areas (Figure 2.6 A). For each segment, we extract the mean slope (using the slope map to derive the erosion coefficients) and the mean observed erosion depth. The results are plotted in Figure 2.8. On these data, we perform a linear correlation between slope and erosion depth, finding a quite good correlation between these two variables. Furthermore, analysing data reported in Figure 2.8 we notice that low values of channel slope (10 – 22%) are associated again (as for Figure 2.7 at pixel scale) to a great heterogeneity in erosion depth with a variance of 2.1 m (range: 0.3 – 2.4 m).

Comparing the mean erosion and slope per channel segment with the maximum entrainment thresholds identified by Kronfellner-Krauss (1984), we can confirm that relationship (Figure 2.8). Moreover, the Kronfellner-Krauss (1984) threshold and the linear interpolation of the mean segment values show similar trends (0.13 and 0.17, respectively).

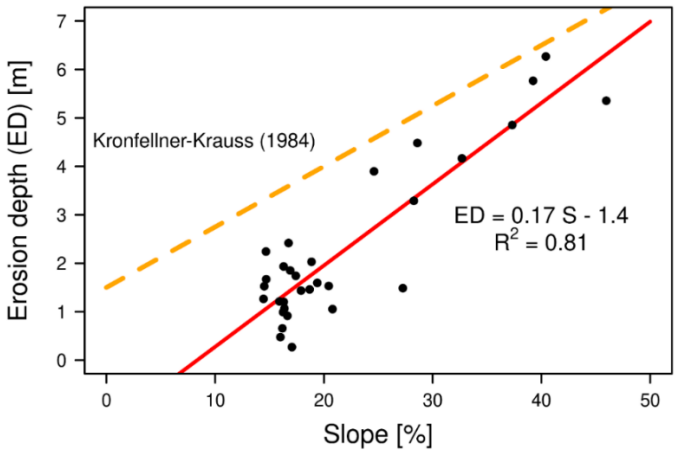

Figure 2.8: Analysis of the erosion depths derived from the DOD and local slope. Points represent mean values extracted from the channel bed, dividing it in segments 20 m long. The reported slope values are derived from the pre-event DTM resampled to 10 m and successively interpolated to 1 m (bicubic method). The red line shows the linear regression derived from the points. The orange dashed line represents the maximum erosion depth identified by Kronfellner-Kraus (1984).

2.5.3 Comparison of observed and simulated volumes

We now focus on the eroded volumes. The simulations performed in this case study are reported in Table 2.2, together with the results in terms of eroded volumes. The equations employed to obtain the erosion coefficient maps are shown in Figure 2.5. In order to assess the accuracy of the simulations, we compare the simulated erosion, represented by the change of the basal surface, and the observed erosion, represented by the DoD. The results are shown in Table 2.2 and Figure 2.6. Looking at the eroded volumes within the computational area, the simulation that entrained the highest debris volume is simulation *P* (C_E calculated with the power function) (173,469 m^3), while simulation *E3* (C_E calculated with the exponential function) predicts the uptake of the least amount of material (10,000 m^3). Analysing the eroded volumes for the control area 1, most of the simulations (*E1*, *E4*, *E5*, *E6*, *LIN*, *LOG* and *P*) yield an accurate (error less than 20%) prediction in terms of the eroded volume. The simulations *F* (fixed C_E), *E2* and *E3* underestimate the eroded volumes with an error of between 48 and 66% (Table 2.2). Looking at the control area 2, the simulation that most accurately represents the observed eroded mass is simulation *E6* with a difference between the simulated and observed eroded volumes of -614 m^3 (relative error of -5%). Simulations *F*, *E4, E5*, *LIN*, *LOG* and *P* entrain a large amount of solid material with respect to the observed debris volume (error between 39 and 425%). On the contrary, the simulations *E1*, *E2*, *E3* entrained considerably small amounts of volume (error between -49 and -89%).

The ratio between the simulated and observed eroded volumes reveals that simulation *E6* represents the observed data for both control areas in the most accurate way (Table 2.2). The other simulations represent either control area 1 or control area 2 in an accurate way. Figure 2.6 shows the results of simulation *E6* for the entrained depths and maximum flow depths (Figure 2.6 B and 2.6 C, respectively).

Table 2.2: Comparison between the simulation results with different coefficients of erosion, calculated for the whole computational area (AOI), the upper part (control area 1) and lower part (control area 2) of the channel path. Observed values are shown as reference.

		AOI	Control area 1			Control area 2		
	C_E	Volume [m^3]	Volume [m^3]	Simulated / observed	Volume/channel length [m^3/m]	Volume [m^3]	Simulated / observed	Volume/channel length [m^3/m]
Observed (DoD)	-	-	10714 ± 824	-	49.6 ± 3.8	13215 ± 1625	-	31.2 ± 3.8
Fixed C_E (*F*)	$C_E = 10^{-6.3}$	73722	5528	0.52	25.6	21410	1.66	50.5
Exponential 1 (*E1*)	$C_E = 10^{(0.05\ S\ -\ 7.5)}$	41702	11445	1.07	53.0	6570	0.51	15.5
Exponential 2 (*E2*)	$C_E = 10^{(0.025\ S\ -\ 7)}$	29968	6429	0.60	29.8	5875	0.45	13.9
Exponential 3 (*E3*)	$C_E = 10^{(0.03\ S\ -\ 7.5)}$	10000	3611	0.34	16.7	1424	0.11	3.4
Exponential 4 (*E4*)	$C_E = 10^{(0.05\ S\ -\ 7)}$	151393	12505	1.17	57.9	48475	3.75	114.4
Exponential 5 (*E5*)	$C_E = 10^{(0.025\ S\ -\ 6.75)}$	83267	11601	1.08	53.7	21815	1.69	51.5
Exponential 6 (*E6*)	$C_E = 10^{(0.02\ S\ -\ 6.75)}$	52710	8645	0.81	40.0	12294	0.95	29.0
Linear (*LIN*)	$C_E = 2.5\ 10^{-8}\ S + 10^{-7.5}$	69947	9659	0.90	44.7	17932	1.39	42.3
Logarithm (*LOG*)	$C_E = 4.5\ 10^{-7}\ \ln(S+5) + 7\ 10^{-7}$	128648	11140	1.04	51.6	40619	3.14	95.9
Power (*P*)	$C_E = 1.5\ 10^{-7}\ S^{0.6} + 2\ 10^{-8}$	173469	12377	1.16	57.3	54923	4.25	129.7

Analysis of the output hydrograph located just upstream from the confluence with the Bigontina torrent (Figure 2.9) allows the simulated peak discharges and solid volume concentrations of the best five simulations to be quantified. The hydrograph showing the discharge and flow volumetric solid concentration for every time step is displayed in Figure 2.9 (for the exponential type simulations we only show E6 for clarity). We further detect that all the simulated flows increase their solid content, reaching a steady value around 0.4 – 0.6 at the output hydrograph location, but they never exceed a value of 0.7. The solid volumetric concentration increases over time for all the simulations represented in Figure 2.9 because of the dam effect of the simulated bridge obstruction. The obstruction involves deposition of the solid component while the fluid fraction slowly flows downstream, consequently increasing the volumetric solid concentration at the output hydrograph location (Figure 2.9). Looking at the discharge, the performed simulations show two types of patterns. Simulations *F*, *P* and *LOG* show a single discharge peak corresponding with the first surge, while the second surge is not captured in the output hydrograph. On the contrary, simulations *LIN* and *E6* show the opposite pattern with a weaker discharge peak for the first surge and a stronger one for the second surge. This can be explained by the terrain morphology of the computational area and the maximum entrainable depth. The simulations P and LOG entrain a large amount of sediment especially in control area 2 (Table 2.2), leading to a big discharge peak at the output hydrograph

for the first surge. However, they do not show the same discharge intensity for the second surge because the maximum entrainment depth has almost been reached after the passage of the first surge. In this way, the simulations *P* and *LOG* do not predict a large amount of entrainable sediment available for the second surge. On the contrary, the simulations *LIN* and *E6* show higher discharge peaks for the second surge, resulting in agreement with the witnesses to the event. In this case, the first surge is mitigated by the morphology of the computational area in which the obstructed bridge creates a dam effect, decreasing the flow velocity and promoting deposition of the solid component. This mitigation effect is not present with the second surge, because the channel has already been filled up with the sediment of the first surge. The second discharge peak thus results decisively more intense than the first one, also due to remobilisation of the previously deposited debris.

Figure 2.9 reveals two further aspects: the first surge is highly impulsive showing a sharp discharge increment, conserving a pattern which is similar to the input hydrograph. In addition, the solid volumetric concentration is similar for all the simulations, looking at the first surge, with values around 0.50 - 0.55.

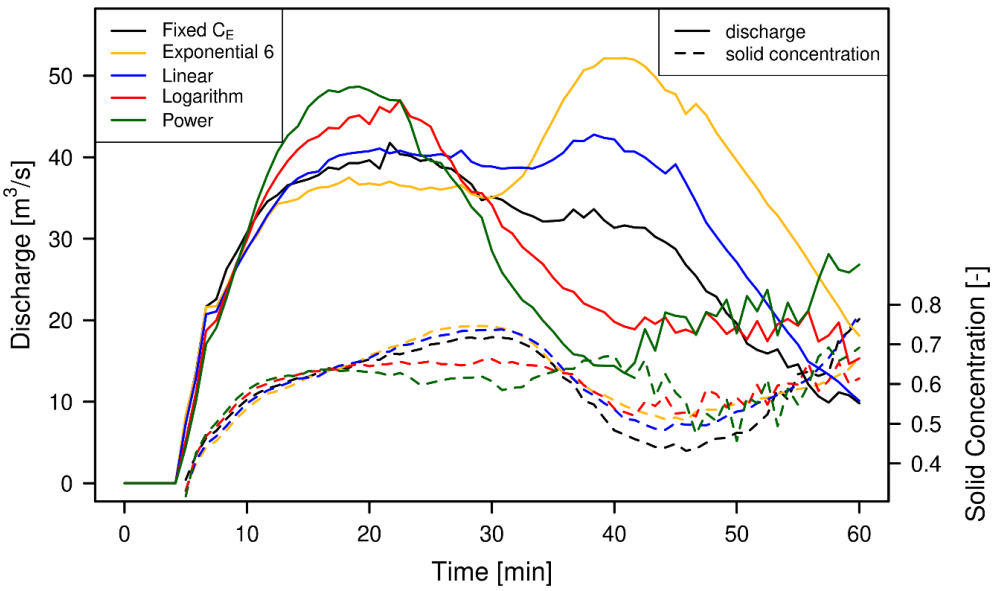

Figure 2.9: Output hydrographs (total discharge and volumetric solid concentration over time) of the performed best simulations just upstream of the confluence with the Bigontina torrent (location shown in Figure 1).

2.6 Discussion

We investigated the debris flow event which occurred in a Dolomitic catchment near the town of Cortina D'Ampezzo (IT) on 4th August 2017. We firstly analysed the observed erosion pattern and then adapted the parameterization of the erosion model implemented in r.avaflow in order to reproduce the observed entrained volumes in the most accurate way. The first analysis was based on the comparison of pre- and post-event DTMs. From these data we identified a maximum erosion depth value of 8 m. Entrainment was comparatively high with a value of 50 m^3 per meter of channel unit in control area 1 and 31 m^3 per meter channel unit in control area 2. Comparing these values with other erosion amounts in literature, it is possible

to highlight the intensity of the event in terms of debris flow erosion. Rickenmann and Zimmermann (1993) reported maximum erosion depths for debris flows in the Swiss Alps of around 5 m. Hungr et al. (2005) reviewed debris flow erosion analysing the entrainment per channel unit, obtaining a range 0 – 50 m^3/m considering more than 500 events reported in 14 studies from different mountain chains. Extreme values of 300 m^3/m were identified by Rickenmann and Weber (2003) for debris flow events in Kazakhstan due to bank failure. Regarding the eastern Alps, Marchi and Cavalli (2007) related values of entrainment per channel unit to the cumulative frequency. In the same study they investigated a debris flow event, reporting a maximum value of 110 m^3 per meter of channel unit. Furthermore, Marchi and D'Agostino (2004) analysed the magnitude of 127 debris flow events in the Eastern Alps, observing that the erosion per channel unit is rarely larger than 50 m^3/m (7% of the entire sample). Thus, according to these findings, the present case study with a maximum value of 50 m^3/m is established as one of the most extreme values recorded in the eastern Alps and worldwide.

Such high eroded volumes per channel unit are the result of a combination of different contributing factors. In the investigated area the availability of a thick layer of loose sediment, a well-defined channel path and the saturation conditions enhanced the debris flow propensity to erosion processes in a noticeable way (Berger et al., 2011; Cannon et al., 2003; Reid et al., 2011). Moreover, the rainfall pattern distribution, characterized by two peaks of equal high intensity, constantly stressed the torrent path, leading to a major destabilization of the channel bed.

Another important driver of erosion in channelized beds is the slope (Hungr et al., 2005); therefore we analysed this variable related to the observed erosion depths. We noticed that plotting the erosion depths against slope values at the DTM resolution we obtained no significant relationship, as illustrated in plot A. Next, we removed the microtopography from the slope map by resampling the slope map from the resolution of 1 m to 10 m (mean value method) and interpolating it to the initial resolution (bicubic method). The new slope values correlated well with erosion depths in a logarithmic way (Figure 2.7, plot B). This reveals that debris flow erosion is more related to a smoothed slope than to a more precise slope value analysed in this case at the resolution of a 1m LiDAR DTM. We may infer that the energy amount of routing debris flows is so big that it can hardly be influenced by small changes in slope, especially if we refer to a resolution of 2 m.

In order to understand the mean erosion rate along the channel path, we divided the torrent bed in reaches of 20 m and then correlated the mean erosion depth with the slope of each bed area. We were able to derive a regression trend line between these two variables confirming the maximum threshold identified in Kronfellner-Krauss (1984), supported by data reported in Rickenmann and Zimmermann (1993). Marchi et al. (2009) computed a similar analysis for a debris flow event in the Eastern Alps (Rio Cucco basin), observing high erosion depths (6 - 9 m) for channel slopes of 30 - 40% and lower erosion depths for steeper sections (regarding the loose sediment bed material). We further confirmed the threshold identified by Takahashi (2007) for the initiation of stony debris flows for channel bed erosion equal to a slope value of

25%. In Figure 2.8, this value identifies those channel reaches for which erosion processes resulted more intense, with mean erosion depths exceeding 3 m, nevertheless a significant contribution to debris flow triggering cannot be excluded in the range 15-20% (Figure 2.8). In our case study, the interpretation of the modelling results also confirmed that slope is one of the main drivers in entrainment processes related to debris flow events in natural confined beds, given that the other torrent conditions remain the same along the path (geology, availability and grain size of loose material and bed width). The slope can be considered as an indicator of the limit strength of the debris to bear erosion for a certain catchment geology. Complementarily, we could suppose that higher is this limit/slope more intense is the erosion when this limit is exceeded, because of great shear stresses become suddenly effective during flashy floods. In addition, after the solid particles detach from the channel bed, the erosion process is amplified by the component of their weight along the direction of the flow momentum (a component that increases as the terrain slope increases). For such reason, we might consider the topographic slope as the main control for debris flow erosion as confirmed in Figure 2.7 and Figure 2.8. However, more studies for a range of rheological and geological situations are required to further investigate the role of slope angle as a control for debris flow entrainment processes.

Since we identified such slope control in channel erosion processes, then we improved the parameterization of the empirical erosion model implemented in r.avaflow calculating the coefficient of erosion (C_E) as a function of the slope. Four different types of functions were used to calculate C_E. We compared the eroded simulated volumes with the DoD and showed that an appropriately parameterized exponential function represents the erosion pattern in the most accurate way. We compared these results with a simulation performed with a fixed coefficient of erosion equal to $10^{-6.3}$ kg^{-1}. This comparison shows a more accurate simulation using an exponentially slope-dependent erosion coefficient, highlighting empirically adequate results for the two control areas characterized by different mean slopes.

We have deliberately employed a simple and straightforward erosion model, multiplying the momentum of the flow with an empirical entrainment coefficient, and calculate this coefficient according to the slope. In the newer literature, in contrast, erosion is often computed by comparing the mechanical strengths of the flow material and the bed (Iverson and Ouyang, 2015; Pudasaini and Fischer, 2020). Whereas these models have a sound physical basis, they are still very hard to apply to real-world cases in practice. The model outcomes are very sensitive to the difference between the mechanical properties of the flow and the surface – however, these properties are usually unknown, and the best which could be done in this respect would be to calibrate the strength parameters with observations. We have followed the alternative way to define those areas as erodible where the bed material is most likely weaker than the flow material, based on geomorphological evidences, and then tried to quantify erosion by hypothesizing a relationship with flow momentum and topography. However, there is an urgent need for more research on how to appropriately compute and parameterize erosion through debris flow processes.

In this study, we were able to reproduce the generation and dynamic of a debris flow through channel bed entrainment thanks to the use of the Pudasaini and Mergili (2019) multi-phase model included in the simulation tool r.avaflow, employing an empirical multi-phase erosion model applied with two phases (equation 2.1 and 2.2). The r.avaflow tool allows the simulation of different types of mass flows and considers the strong relation between the fluid, fine solid and solid momentum transfer. It could therefore be used to reproduce the interaction, mixing and separation of up to three considered phases. The simulations performed in this study used two phases and showed that the solid and fluid components entrained by the flow were mixed and contributed to the momentum increase of the flowing mass. In particular, the fluid component played the main role in the entrainment process particularly in the initial stage, progressively entraining solid material (the input hydrograph had a 10% solid fraction). At the lower end of the computational area, the results of simulation *E6* (C_E as an exponential function of the slope) showed a solid fraction up to 50 – 55% for the two discharge peaks, typical for a mature debris flow. The similar solid concentration of the performed simulations can be explained by (i) the value of the bed solid fraction (equation (2.1) – (2.2), $\alpha_{s,Emax}$) fixed to 0.7 and (ii) the effect of the fluid fraction necessary to produce drag force for solid phase motion. In particular, if the fluid fraction is not sufficient to move the total amount of the solid phase, the solid part tends to deposit and eventually, it can be successively moved if the upcoming flow can generate enough drag force. In this way, the simulated solid fraction at the output hydrograph never exceeded a value of 0.57 during the flow propagation, as shown in Figure 2.9 for the first 20 min of the different simulations. Afterwards, the solid component noticeably increased for the deposition process caused by the bridge.

Comparing the simulated and observed entrained volumes and the erosion depths per channel unit for the two control areas we found a good accuracy of the simulated amount of entrained material (Table 2.2). The peak discharge increased up to four times the input hydrograph for the second surge. The observed and simulated entrainment patterns lead to the consideration that erosion processes have to be accurately assessed for the simulation of debris flows over mobile beds since they can notably increase their destructive potential as highlighted in earlier studies (Berger et al., 2010; Chen and Zhang, 2015; Gregoretti et al., 2019; Mergili et al., 2018; Rosatti and Begnudelli, 2013). In addition, the proposed entrainment approach could be straightforwardly applied for the simulation of a dam break scenario. The erosion coefficient is really small in the case of flat terrain (C_E is never equal to zero), but if the flow momentum results high, the fluid flux can trigger a debris flood or debris flow depending both on its momentum and terrain topography. The obtained slope-dependent function for C_E assessment is at the same time an easy and efficient approach to model debris flow erosion. The proposed method can be potentially implemented also in other mass flow propagation models, making it a broadly useful approach.

The investigated case study can be classified as extreme considering the observed erosion rates, caused by the availability of a large amount of loose saturated debris. The findings correspond to earlier studies both for the Alps (Marchi and Cavalli, 2007) and worldwide, and the erosion model reported here is considered suitable to reproduce this event. We can affirm that the model may be used to accurately estimate maximum

thresholds of erosion in the simulations of debris flows over natural channels. However, the calibrated exponential function to derive the erosion coefficient has to be accurately tested with other case studies to evaluate its reliability. Future refinements of the proposed approach might consider other factors affecting erosion such as bed confinement and bed forms, and parameters describing the debris flow composition in more detail.

2.7 Conclusions

We investigated the debris flow event which occurred in 2017 in the Bigontina dolomitic catchment of the Eastern Alps in Italy. The event obstructed the bridge of the regional road and successively triggered an intense bed load transport event that flooded the village of Alverà causing one fatality. In this study we focused on the entrainment processes of the debris flow event. The availability of pre- and post-event LiDAR campaigns allowed us to study the spatial patterns of the volumes entrained by the debris flow. We then successfully back-calculated the debris flow using the simulation tool r.avaflow and proposing a new parameterization of the erosion model.

Regarding the observed eroded volumes, we compared the investigated event with studies reported in the literature and we can define this event as one of the most extreme affecting the eastern Alps, in terms of documented erosion. Furthermore, we confirmed that channel erosion is highly correlated with a smoothed slope map (Figure 2.7). Moreover, we analyzed the mean erosion depth observed within each channel segment (Figure 2.8), and we confirmed the threshold suggested by Kronfellner-Krauss (1984).

Regarding the back calculation part, we used the Pudasaini and Mergili (2019) multi-phase model included in r.avaflow, together with the empirical erosion model. Since erosion is related to slope (Figure 2.7 and Figure 2.8), we evaluated different equations to calculate a spatially distributed erosion coefficient based on the topographic slope (Figure 2.5). We compared the simulated eroded volumes against the difference between the pre- and post-event DTMs. Thereby, an exponential function of the slope turned out as the most accurate way to derive the spatially distributed erosion coefficient for simulating the entrainment process and to capture the complex dynamics of a composite/double peak triggering event. Another important simulation result is the generation of a mature debris flow through progressive entrainment of the solid component along the channel path. The input hydrograph is characterized by 10% solid content (Figure 2.4), while at the end of the computational area the solid ratio is 45 - 60% (Figure 2.8), noticeably increasing the peak discharge.

This study highlights that channel erosion processes have to be taken into great account in debris flow simulations because they increase destructive potential, times of passage of the surges, and dynamics of the events. Furthermore, r.avaflow appears suitable for the simulation of debris flows on erodible channels thanks to the multi-phase propagation model in combination with a multi-phase empirical erosion model. In particular, we defined a new method to improve the quality of the entrainment parameters by calibrating a function for the calculation of the spatially distributed erosion coefficient. Future studies have to confirm

and possibly to improve the reported approach in order to make it suitable for predictive simulations within the framework of hazard mapping and risk management.

Acknowledgements

This work was supported by the project: “Bridging the mass-flow modelling with the reality”, funded by CARIPARO foundation. Authors wish to thank the Italian Environment Minister for the 2009 LiDAR data, and, the Regional Environment Agency of Veneto for the 2017 LiDAR data. Data are available on request to the corresponding author. Thanks to Francesco Marra for his fundamental contribution in the radar data analysis and precipitation evaluation and also to Francesco Bettella for his support in the hydrological analysis. Thanks to Fabio Da Re of the Veneto Region for his contribution to the reconstruction of the debris flow event through collecting information from witnesses and through qualitative post-event surveys. We are grateful to the two reviewers for their useful suggestions.

2.8 References

Anagnostou, M.N., Kalogiros, J., Anagnostou, E.N., Tarolli, M., Papadopoulos, A., Borga, M., 2010. Performance evaluation of high-resolution rainfall estimation by X-band dual-polarization radar for flash flood applications in mountainous basins. J. Hydrol. 394, 4–16. https://doi.org/10.1016/j.jhydrol.2010.06.026

Armanini, A., Fraccarollo, L., Rosatti, G., 2009. Two-dimensional simulation of debris flows in erodible channels. Comput. Geosci. 35, 993–1006. https://doi.org/10.1016/j.cageo.2007.11.008

Baggio, T., 2018. Assessment of the mass flow multi- process simulation model: r.avaflow (Master dissertation). University of Padova.

Bagnold, R.A., 1966. An Approach to the Sediment Transport Problem from General Physics. USGS Prof. Pap. 42. https://doi.org/10.1017/S0016756800049074

Bartelt, P., Salm, B., Gruber, U., 1999. Calculating dense-snow avalanche runout using a Voellmy-fluid model with active/passive longitudinal straining. J. Glaciol. 45, 242–254. https://doi.org/10.3189/002214399793377301

Baum, R.L., Godt, J.W., Coe, J.A., 2011. Assessing susceptibility and timing of shallow landslide and debris flow initiation in the Oregon Coast Range, USA, in: International Conference on Debris-Flow Hazards Mitigation: Mechanics, Prediction, and Assessment, Proceedings. pp. 825–834. https://doi.org/10.4408/IJEGE.2011-03.B-090

Berger, C., McArdell, B.W., Fritschi, B., Schlunegger, F., 2010. A novel method for measuring the timing of bed erosion during debris flows and floods. Water Resour. Res. 46, 1–7. https://doi.org/10.1029/2009WR007993

Berger, C., McArdell, B.W., Schlunegger, F., 2011. Direct measurement of channel erosion by debris flows, Illgraben, Switzerland. J. Geophys. Res. Earth Surf. 116, n/a-n/a. https://doi.org/10.1029/2010JF001722

Berti, M., Genevois, R., Simoni, A., Tecca, P.R., 1999. Field observations of a debris flow event in the Dolomites. Geomorphology 29, 265–274. https://doi.org/10.1016/S0169-555X(99)00018-5

Berti, M., Simoni, A., 2005. Experimental evidences and numerical modelling of debris flow initiated by

channel runoff. Landslides 2, 171–182. https://doi.org/10.1007/s10346-005-0062-4

Brasington, J., Langham, J., Rumsby, B., 2003. Methodological sensitivity of morphometric estimates of coarse fluvial sediment transport. Geomorphology 53, 299–316. https://doi.org/10.1016/S0169-555X(02)00320-3

Brasington, J., Rumsby, B.T., McVey, R.A., 2000. Monitoring and modelling morphological change in a braided gravel-bed river using high resolution GPS-based survey. Earth Surf. Process. Landforms 25, 973–990. https://doi.org/10.1002/1096-9837(200008)25:9<973::AID-ESP111>3.0.CO;2-Y

Cannon, Susan H, Cannon, S H, Gartner, J.E., Parrett, C., Parise, M., 2003. Wildfire-related debris-flow generation through episodic progressive sediment-bulking processes, western USA, in: Debris-Flow Hazards Mitigation: Mechanics, Prediction, and Assessment.

Chen, H., Crosta, G.B., Lee, C.F., 2006. Erosional effects on runout of fast landslides, debris flows and avalanches: a numerical investigation. Géotechnique 56, 305–322. https://doi.org/10.1680/geot.2006.56.5.305

Chen, H.X., Zhang, L.M., 2015. EDDA 1.0: Integrated simulation of debris flow erosion, deposition and property changes. Geosci. Model Dev. 8, 829–844. https://doi.org/10.5194/gmd-8-829-2015

Christen, M., Kowalski, J., Bartelt, P., 2010. RAMMS: Numerical simulation of dense snow avalanches in three-dimensional terrain. Cold Reg. Sci. Technol. 63, 1–14. https://doi.org/10.1016/j.coldregions.2010.04.005

Church, M., Jakob, M., 2020. What Is a Debris Flood? Water Resour. Res. 56. https://doi.org/10.1029/2020WR027144

Coussot, P., Meunier, M., 1996. Recognition, classification and mechanical description of debris flows. Earth-Science Rev. 40, 209–227. https://doi.org/10.1016/0012-8252(95)00065-8

Crosta, G.B., De Blasio, F. V., Locatelli, M., Imposimato, S., Roddeman, D., 2015. Landslides falling onto a shallow erodible substrate or water layer: an experimental and numerical approach. IOP Conf. Ser. Earth Environ. Sci. 26, 012004. https://doi.org/10.1088/1755-1315/26/1/012004

D'Agostino, V., 2010. Filtering-retention check dam design in mountain torrents, in: Garcia, C.C., Lenzi, M.A. (Eds.), Check Dams, Morphological Adjustments and Erosion Control in Torrential Streams. Nova Science, New York. Nova Science Publishers, pp. 185–210.

D'Agostino, V., 1996. Analisi quantitativa e qualitativa del transporto solido torrentizio nei bacini montani del Trentino Orientale. 1a Sezione, Vol. Present. Occas. del Convegno di Stud. I Probl. dei Gd. comprensori irrigui c, 111–123.

D'Agostino, V., Pastorello, R., Bettella, F., 2018. Analisi storica degli eventi di piena, analisi idrologica e reologica dei fenomeni di trasporto solido e di massa nel torrente Bigontina a monte dell'abitato di Alverà, in comune di Cortina D'Ampezzo per l'individuazione delle opere idrauliche per la messa in sicurezza d-infrastrutture viarie e abitati. (Technical report)

Egashira, S., Ashida, K., 1987. Sediment transport in steep slope flumes, in: Japan Joint Seminar on Water Resources.

Ellen, S.D., Algus, M.A., Cannon, S.H., Fleming, R.W., Lahr, P.C., Peterson, D.M., Reneau, S.L., 1982. Description and mechanics of soil slip/debris flows in the storm. California. U.S. Geol. Surv. Prof. Pap. 1434, 63–112.

Fischer, J.T., Kowalski, J., Pudasaini, S.P., 2012. Topographic curvature effects in applied avalanche modeling. Cold Reg. Sci. Technol. 74–75, 21–30. https://doi.org/10.1016/j.coldregions.2012.01.005

Forti, A., 1920. Elementi per la progettazione delle piene catastrofiche nei corsi d'acqua montani. Ann. del Cons. Super. delle Acque 2, 55–74.

Fraccarollo, L., Capart, H., 2002. Riemann wave description of erosional dam-break flows. J. Fluid Mech. 461, 183–228. https://doi.org/10.1017/S0022112002008455

Fuller, I.C., Large, A.R.G., Charlton, M.E., Heritage, G.L., Milan, D.J., 2003. Reach-scale sediment transfers: An evaluation of two morphological budgeting approaches. Earth Surf. Process. Landforms 28, 889–903. https://doi.org/10.1002/esp.1011

GRASS Development Team, 2020. Geographic Resources Analysis Sup- port System (GRASS) Software, Version 7.8 [WWW Document]. URL http://grass.osgeo.org (accessed 8.1.20).

Gregoretti, C., Degetto, M., Bernard, M., Boreggio, M., 2018. The Debris Flow Occurred at Ru Secco Creek, Venetian Dolomites, on 4 August 2015: Analysis of the Phenomenon, Its Characteristics and Reproduction by Models. Front. Earth Sci. 6, 80. https://doi.org/10.3389/feart.2018.00080

Gregoretti, C., Stancanelli, L.M., Bernard, M., Boreggio, M., Degetto, M., Lanzoni, S., 2019. Relevance of erosion processes when modelling in-channel gravel debris flows for efficient hazard assessment. J. Hydrol. 568, 575–591. https://doi.org/10.1016/j.jhydrol.2018.10.001

Griffiths, P.G., Webb, R.H., Melis, T.S., 1997. Initiation of debris flows in tributaries of the Colorado River in Grand Canyon, Arizona, in: 1st International Conference on Debris-Flow Hazards Mitigation, Mechanics, Prediction and Assessment.

Grigorian, S.S., Eglit, M.E., Iakimov, I.L., 1967. New statement and solution of the problem of the motion of snow avalanche. Tr. Vycokogornogo Geofiz. Instituta 12, 104–113.

Grimaldi, S., Petroselli, A., 2015. Do we still need the Rational Formula? An alternative empirical procedure for peak discharge estimation in small and ungauged basins. Hydrol. Sci. J. 60, 67–77. https://doi.org/10.1080/02626667.2014.880546

Han, Z., Chen, G., Li, Y., Tang, C., Xu, L., He, Y., Huang, X., Wang, W., 2015. Numerical simulation of debris-flow behavior incorporating a dynamic method for estimating the entrainment. Eng. Geol. 190, 52–64. https://doi.org/10.1016/j.enggeo.2015.02.009

Hungr, O., 1995. A model for the runout analysis of rapid flow slides, debris flows, and avalanches. Can. Geotech. J. 32, 610–623. https://doi.org/10.1139/t95-063

Hungr, O., Leroueil, S., Picarelli, L., 2014. The Varnes classification of landslide types, an update. Landslides 11, 167–194. https://doi.org/10.1007/s10346-013-0436-y

Hungr, O., McDougall, S., Bovis, M., 2005. Entrainment of material by debris flows, in: Debris-Flow Hazards and Related Phenomena. Springer, Berlin, Heidelberg, pp. 135–158. https://doi.org/10.1007/3-540-27129-5_7

Hungr, O., Morgan, G.C., Kellerhals, R., 1984. Quantitative analysis of debris torrent hazards for design of remedial measures. Can. Geotech. J. 21, 663–677. https://doi.org/10.1139/t84-073

Hutter, K., Svendsen, B., Rickenmann, D., 1996. Debris flow modeling: a review. Contin. Mech. Thermodyn. 23, 93. https://doi.org/10.1016/S0301-9322(97)80255-8

Hutter, K., Svendsen, B., Rickenmann, D., 1994. Debris flow modeling: A review. Contin. Mech. Thermodyn. https://doi.org/10.1007/BF01175749

Iverson, R.M., 2012. Elementary theory of bed-sediment entrainment by debris flows and avalanches. J. Geophys. Res. Earth Surf. 117, 1–17. https://doi.org/10.1029/2011JF002189

Iverson, R.M., 1997. The Physics of debris flow. Rev. Geophys. 35, 245–296.

https://doi.org/10.1603/033.046.0206

Iverson, R.M., Ouyang, C., 2015. Entrainment of bed material by Earth-surface mass flows: Review and reformulation of depth-integrated theory. Rev. Geophys. 53, 27–58. https://doi.org/10.1002/2013RG000447

Iverson, R.M., Reid, M.E., Logan, M., LaHusen, R.G., Godt, J.W., Griswold, J.P., 2011. Positive feedback and momentum growth during debris-flow entrainment of wet bed sediment. Nat. Geosci. 4, 116–121. https://doi.org/10.1038/ngeo1040

Iverson, R.M., Schilling, S.P., Vallance, J.W., 1998. Objective delineation of lahar-inundation hazard zones. Geol. Soc. Am. Bull. 110, 972–984. https://doi.org/10.1130/0016-7606(1998)110<0972:ODOLIH>2.3.CO;2

Jakob, M., Hungr, O., Jakob, D., 2005. Debris-flow hazards and related phenomena, Springer.

Kattel, P., Khattri, K.B., Pokhrel, P.R., Kafle, J., Tuladhar, B.M., Pudasaini, S.P., 2016. Simulating glacial lake outburst floods with a two-phase mass flow model. Ann. Glaciol. 57, 349–358. https://doi.org/10.3189/2016AoG71A039

Kean, J.W., McCoy, S.W., Tucker, G.E., Staley, D.M., Coe, J.A., 2013. Runoff-generated debris flows: Observations and modeling of surge initiation, magnitude, and frequency. J. Geophys. Res. Earth Surf. 118, 2190–2207. https://doi.org/10.1002/jgrf.20148

Kronfellner-Kraus, G., 1984. Extreme Feststofffrachten und Grabenbildungen von Wildbächen [ex- treme sediment loads and erosion of torrents], in: Int. Symp. Interpraevent. Villach, pp. 109–118.

Marchi, L., Cavalli, M., 2007. Procedures for the documentation of historical debris flows: Application to the Chieppena Torrent (Italian Alps). Environ. Manage. 40, 493–503. https://doi.org/10.1007/s00267-006-0288-5

Marchi, L., Cavalli, M., Sangati, M., Borga, M., 2009. Hydrometeorological controls and erosive response of an extreme alpine debris flo. Hydrol. Process. 2727, 2714–2727. https://doi.org/10.1002/hyp

Marchi, L., D'Agostino, V., 2004. Estimation of debris-flow magnitude in the Eastern Italian Alps. Earth Surf. Process. Landforms 29, 207–220. https://doi.org/10.1002/esp.1027

Marra, F., Morin, E., 2018. Autocorrelation structure of convective rainfall in semiarid-arid climate derived from high-resolution X-Band radar estimates. Atmos. Res. 200, 126–138. https://doi.org/10.1016/j.atmosres.2017.09.020

Marra, F., Morin, E., 2015. Use of radar QPE for the derivation of Intensity–Duration–Frequency curves in a range of climatic regimes. J. Hydrol. 531, 427–440. https://doi.org/10.1016/j.jhydrol.2015.08.064

Marra, F., Nikolopoulos, E.I., Creutin, J.D., Borga, M., 2014. Radar rainfall estimation for the identification of debris-flow occurrence thresholds. J. Hydrol. 519, 1607–1619. https://doi.org/10.1016/j.jhydrol.2014.09.039

McDougall, S., Hungr, O., 2005. Dynamic modelling of entrainment in rapid landslides. Can. Geotech. J. 42, 1437–1448. https://doi.org/10.1139/t05-064

Mergili, M., Emmer, A., Juřicová, A., Cochachin, A., Fischer, J.T., Huggel, C., Pudasaini, S.P., 2018. How well can we simulate complex hydro-geomorphic process chains? The 2012 multi-lake outburst flood in the Santa Cruz Valley (Cordillera Blanca, Perú). Earth Surf. Process. Landforms 43, 1373–1389. https://doi.org/10.1002/esp.4318

Mergili, M., Fischer, J.T., Krenn, J., Pudasaini, S.P., 2017. R.avaflow v1, an advanced open-source computational framework for the propagation and interaction of two-phase mass flows. Geosci. Model

Dev. 10, 553–569. https://doi.org/10.5194/gmd-10-553-2017

Mergili, M., Pudasaini, S.P., 2020. r.avaflow - The mass flow simulation tool [WWW Document]. URL https://www.avaflow.org (accessed 1.7.20).

Mishra, S.K., Singh, V.P., 2003. Soil Conservation Service Curve Number (SCS-CN) Methodology, Water Science and Technology Library. Springer Netherlands, Dordrecht. https://doi.org/10.1007/978-94-017-0147-1

O'Brien, J.S., 1986. Physical processes, rheology and modeling of mudflows. Colorado State University.

O'Brien, J.S., Julien, P.Y., Fullerton, W.T., 1993. Two-Dimensional water flood and mudflow simulation. J. Hydraul. Eng. 119, 244–261.

Oliver, M.A., Webster, R., 1990. Kriging: A method of interpolation for geographical information systems. Int. J. Geogr. Inf. Syst. 4, 313–332. https://doi.org/10.1080/02693799008941549

Pastorello, R., D'Agostino, V., Hürlimann, M., 2020. Debris flow triggering characterization through a comparative analysis among different mountain catchments. Catena 186, 104348. https://doi.org/10.1016/j.catena.2019.104348

Pirulli, M., Pastor, M., 2012. Numerical study on the entrainment of bed material into rapid landslides. Géotechnique 62, 959–972. https://doi.org/10.1680/geot.10.p.074

Pitman, E.B., Long, L.E. Le, 2005. A two-fluid model for avalanche and debris flows. Philos. Trans. R. Soc. A Math. Phys. Eng. Sci. 363, 1573–1601. https://doi.org/10.1098/rsta.2005.1596

Pudasaini, S.P., 2012. A general two-phase debris flow model. J. Geophys. Res. Earth Surf. 117, 1–28. https://doi.org/10.1029/2011JF002186

Pudasaini, S.P., Fischer, J.T., 2020. A mechanical erosion model for two-phase mass flows. Int. J. Multiph. Flow 132, 1–16. https://doi.org/10.1016/j.ijmultiphaseflow.2020.103416

Pudasaini, S.P., Mergili, M., 2019. A Multi-Phase Mass Flow Model. J. Geophys. Res. Earth Surf. 124, 1–23. https://doi.org/10.1029/2019jf005204

Pudasaini, S.P., Wang, Y., Hutter, K., 2005. Modelling debris flows down general channels. Nat. Hazards Earth Syst. Sci. 5, 799–819. https://doi.org/10.5194/nhess-5-799-2005

R Core Team, 2020. R: A language and environment for statistical computing [WWW Document]. R Found. Stat. Comput. URL http://www.r-project.org (accessed 8.1.20).

Reid, M.E., Iverson, R.M., Logan, M., Lahusen, R.G., Godt, J.W., Griswold, J.P., 2011. Entrainment of bed sediment by debris flows: Results from large-scale experiments, in: International Conference on Debris-Flow Hazards Mitigation: Mechanics, Prediction, and Assessment, Proceedings. pp. 367–374. https://doi.org/10.4408/IJEGE.2011-03.B-042

Rickenmann, D., 2007. Runout prediction methods, in: Springer (Ed.), Debris-Flow Hazards and Related Phenomena. Berlin, pp. 305–324. https://doi.org/10.1007/3-540-27129-5_13

Rickenmann, D., Weber, D., Stepanov, B., 2003. Erosion by debris flows in field and laboratory experiments. Int. Conf. Debris-Flow Hazards Mitig. Mech. Predict. Assessment, Proc. 2, 883–894.

Rickenmann, D., Zimmermann, M., 1993. The 1987 debris flows in Switzerland: documentation and analysis. Geomorphology 8, 175–189. https://doi.org/10.1016/0169-555X(93)90036-2

Rosatti, G., Begnudelli, L., 2013. Two-dimensional simulation of debris flows over mobile bed: Enhancing the TRENT2D model by using a well-balanced Generalized Roe-type solver. Comput. Fluids 71, 179–195. https://doi.org/10.1016/j.compfluid.2012.10.006

Sampl, P., Zwinger, T., 2004. Avalanche simulation with SAMOS. Ann. Glaciol. 38, 393–398. https://doi.org/10.3189/172756404781814780

Savage, S.B., Hutter, K., 1989. The motion of a finite mass of granular material down a rough incline. J. Fluid Mech. 199, 177–215. https://doi.org/10.1017/S0022112089000340

Takahashi, T., 2007. Debris Flow: Mechanics, Prediction and Countermeasures.

Takahashi, T., 2000. Initiation and flow of various types of debris-flow, in: Debris-Flow Hazards Mitigation: Mechanics, Prediction, and Assessment. pp. 15–25.

Takahashi, T., Das, D., 2014. Debris flow: mechanics, prediction and countermeasures, 2nd editio. ed. CRC Press, Balkema.

Takahashi, T., Kuang, S.F., 1986. Formation of debris flow on varied slope bed. Disaster Prev. Res. Inst. Annu. 29, 343–359.

Takahashi, T., Nakagawa, H., Harada, T., Yamashiki, Y., 1992. Routing Debris Flows with Particle Segregation. J. Hydraul. Eng. 118, 1490–1507. https://doi.org/10.1061/(ASCE)0733-9429(1992)118:11(1490)

Voellmy, A., 1955. Über die Zerstörungskraft von Lawinen. Schweizerische Bauzeitung 73, 159–165. https://doi.org/10.2746/042516407X182811

3 Simulating the effect of check dam collapse in a debris-flow channel

Tommaso Baggio[1,*], Vincenzo D'Agostino[1]

[1] *Department of Land, Environment, Agriculture and Forestry, University of Padua, via dell'Università 16, 35020 Legnaro (PD), Italy*

This chapter has been published in *Science of the Total Environment* in 2021

3.1 Abstract

Sequences of erosion control/consolidation check dams are the most widespread channel countermeasure in the European Alps. Some of them were built in the past based on ancient technologies. Nowadays they may not be fully adequate to mitigate the debris-flow/flood events that are becoming more frequent and intense. Consequently, there is the remote possibility that they could fail with disastrous consequences as observed in some cases. A reliable methodology to reproduce the effect of check dam collapse has not yet proposed. Therefore the aim of this study is to define a procedure to simulate the effect of check dam collapse in a debris-flow event. In this study we analysed the catastrophic debris flow occurred in the Rotian channel (Italian Alps) during which a series of check dams collapsed magnifying the event and causing severe damages. With the aid of field data we reconstructed the event and used the simulation tool r.avaflow to reproduce the debris flow. We then defined three scenarios to simulate the event: (A) debris-flow propagation over an erodible channel; (B) propagation on a rigid channel bed combined with the release of impulsive masses to isolate the analysis of the effect of check dam collapse; (C) a combination of the previous scenarios. The simulation performance was assessed analysing the pre- and post-event LiDAR surveys. Results showed that the C scenario accurately reproduced the observed debris-flow erosion pattern. In particular, we found out that most of the entrained debris volume derived from bed erosion rather than the sediment retained by check dams. The adopted method, which composes the contribution of bed erosion and check dam collapse, could be of particular relevance for residual risk estimation when mitigation structures are old and may fail with potential disastrous consequences.

Keywords: Debris flow, Check dam collapse, Bed erosion, Propagation modelling

3.2 Introduction

Debris flows are rapid mass movements made up by a mixture of water, fine particles, sediment and boulders (Hungr et al., 2014; Jakob et al., 2005; Takahashi, 2007). They can develop high velocities (up to 10 ms^{-1}) generating impressive impact forces (Rickenmann et al., 2003) because of their high bulk density. When debris flows affect villages they can completely destroy infrastructures and buildings causing severe damage and fatalities (Dowling and Santi, 2014; Larsen et al., 2001). For this reason, debris-flow mitigation structures have been built to reduce the associated risk. Such structures mitigate the risk in different ways (Huebl and Fiebiger, 2005; Mizuyama, 2008): they decrease the flow velocity and bed erosion rates (consolidation check dams), promote sediment deposition (flow breakers, open retention check dams, sediment traps, deposition areas, flood reservoir), prevent bed and bank erosion (channelization, bank reinforcements, bed sills) and control the flow spread (deflection walls). Such countermeasures are planned and located according to the morphology, sediment budget and characteristics of the channel and basin (Johnson and McCuen, 1989; Osti and Egashira, 2008). All of these structures have the final goal of reducing the potential consequences of debris-flow events. The hazard and risk map is calculated taking into account the mitigation structures located in the watershed (Fuchs et al., 2007; Gentile et al., 2007; Rodríguez-Morata et al., 2019). A consolidation check dam is the most common type of mitigation structure for debris flow within the channel bed (Piton and Recking, 2014). They are transversal structures often built in a staircase – like sequence in a way that decreases bed erosion, sediment transport, front velocity, pulse behaviour and bank destabilization (Zeng et al., 2009). Even if check dams have been designed taking into account the geomorphological conditions after analysing past events, they may not be representative of future events (Hübl et al., 2005). In fact, in the last decades climate change has rapidly triggered glacier melting, permafrost degradation and taken rainstorms to extremes (Borga et al., 2014; Prein et al., 2016; Stoffel et al., 2014; Vagnon, 2020). The expected consequence is an increase of debris-flow severity and frequency in terms of water and sediment volume. Moreover, check dams can be damaged by debris flow and debris flood over decades, causing scouring erosion to the foundations, damage to the crest and body and lateral erosion (Tacnet et al., 2012; Victoriano et al., 2018). Furthermore the correct maintenance of mitigation structures is increasingly lacking (Mazzorana et al., 2014). The consequences may lead to the collapse of check dams as observed in some cases of extreme events (Benito et al., 1998; Chen et al., 2015; Cucchiaro et al., 2019a, 2019b; Wang, 2013). The volume of debris flow increases both because of the released material during the collapse and the increase of local channel slope after the collapse (Piton et al., 2016). As consequence of channel slope increase both entrainment (Gregoretti, 2008; Lamb et al., 2008) and transport capacity (Armanini, 2015; Lanzoni et al., 2017; Takahashi, 2007) grow. Therefore the failure of a check dam or a series of them can have incredibly severe consequences, and debris flows can likely impact areas classified as having no or low risk. Then, the concept that mitigation measures are commonly always considered adequate to decrease the event magnitude may not be totally confirmed (Piton et al., 2016). Scenarios of mitigation structures collapse are seldom considered but they should at least be mentioned and taken into account as a remote but possible scenario in the risk assessment framework.

Simulation tools can reproduce the dynamic of mass movements (landslides, debris flows, floods) along a defined topography given a set of input data (Scheidl et al., 2013). Therefore, the production of hazard maps and then risk maps is commonly based on the output of hydraulic and mass flow propagation models (Mazzorana et al., 2009; Stecher et al., 2012).

Simulation tools can be used to assess the effectiveness of check dams (Bernard et al., 2019; Osti and Egashira, 2008; Remaître et al., 2008; Liu et al., 2012) and to predict the residual risk in the case of protection measure collapse (Tseng et al., 2012). To simulate structure collapse scenarios, the choice of an adequate simulation tool is fundamental to reproduce the phenomena in the most reliable way. For debris flow phenomena the tool should match different characteristics. (i) It should consider the flow as a biphasic mass in order to both accurately represent the behaviour of the debris flow phenomenon (Kean et al., 2013) and to reproduce the released or entrained mass since they are characterized by a higher debris content than the flowing mass (Papa et al., 2004). (ii) The model should incorporate the flow propagation over erodible bed, since erosion processes can be really strong after the structure collapse (Cucchiaro et al., 2019a). (iii) The simulation tool should consider (a) the possibility of introducing the volume into the computational domain through mass release to represent the volume of debris released after the check dam collapse and (b) a solid-liquid hydrograph to introduce the debris-flow routing. Different models for debris-flow propagation have been developed in the last years and successfully tested with real case scenarios (Frank et al., 2015; Gregoretti et al., 2018; McDougall and Hungr, 2004; O'Brien et al., 1993; Rosatti and Begnudelli, 2013). Some of them incorporate an erosion model and the possibility of releasing a mass. Among the different tools, r.avaflow (Mergili and Pudasaini, 2021) resulted adequate for structures collapse scenarios thanks to its flexibility in introducing the mass in the computational domain, the presence of the empirical erosion model (Mergili et al., 2017) and the multi-phase mass flow propagation model (Pudasaini and Mergili, 2019). Moreover, r.avaflow have already been used to back calculate geomorphologically complex scenarios that include interaction between landslide, glacier, debris flow and lake (Baggio et al., 2018; Gylfadóttir et al., 2019; Mergili et al., 2020b, 2018). The empirical erosion model has been analysed and calibrated for landslide (Mergili et al., 2020a) and debris flow phenomena (Baggio et al., 2021).

The need to strengthen our capacity to model the effect of the collapse of a series of check dams is still an open research question (Zhang et al., 2019) and is motivated by the increasing attention of public authorities towards communication of the residual hazard and related risk (Hartmann et al., 2021). The aim of this study is to develop and test a procedure to adequately simulate the effect of check dam collapse in case of a high-magnitude debris-flow event.

For this purpose a recent extreme debris-flow event amplified by the failure of a series of check dams is presented. Thanks to pre- and post- event surveys and a field campaign, the event is reconstructed. The debris-flow hydrograph is estimated and an operative procedure is proposed to simulate the effect of check dam failure. Three simulation scenarios are computed to reproduce the effects of check dam failure through mass release and channel erosion. The following discussion considers the reliability, implications and

generalization of the results. The outcomes of the study highlight a replicable methodologic path that can be used to simulate the consequences of check dam failure in debris-flow hazard scenarios for risk mapping.

3.3 Material and methods

In this section it is first described the characteristics of the Rotian catchment reporting the morphology of the channel, the pre-event mitigation structures and fan description. Then the debris-flow event occurred on 29th October 2018 is recounted, describing the methods to reconstruct the debris-flow characteristics and erosion pattern. Lastly, the simulation model is depicted, as well as the input data to reproduce the event and evaluate the simulation performance.

3.3.1 Study site: the rio Rotian channel

The rio Rotian channel is a mountainous torrent located in the autonomous province of Trento, in the Eastern Italian Alps. The catchment has a total extent of 2.4 km^2 and a mean slope of 26.4°, extending from an altitude of 2042 to 824 m a.s.l. (Figure 3.1). The shape of the basin is elongated along the main channel path in a north – east direction. The geology of the basin is composed by colluvial, alluvial and glacial deposits in the lower part (below 1300 m a.s.l.), while the upper part is composed by stratified layers of limestone and clay. Due to these geological characteristics, in the last centuries the channel progressively deepened, generating a canyon-like incision of around 10–50 m of elevation difference compared with the top of the banks. The banks are very steep (range 30–45°) and they are very probably the source of sediment supply to the stream in the case of intense runoff.

The channel is 4.8 km long and has a mean slope of 11.9°. It has been consolidated with a series of 15 check dams built in 1977 (reach in the range from 1233 to 1030 m a.s.l.) and made of reinforced concrete. The check dam mean height is 5.3m (range 2.9–7.8m) for a cumulative sum of 78.9m and a mean channel slope of 13°. Immediately downstream of the last check dam the channel bed has been enlarged in order to create a depositional area formed by a series of 5 retention basins connected each other by a sloped reach (total length 250 m, mean width 25 m). In 2014, a 7.4 m high open check dam was constructed at 989 m a.s.l., immediately downstream of the retention basins (Figure 3.1), to increase the deposition of the flowing solid component.

The fan apex is at an altitude of 824m a.s.l. and the fan has an area of 0.38 km^2. The channel crosses the fan centrally and joins with the Noce river at an elevation of 782m a.s.l. The village of Dimaro is located on the fan, mainly consisting of a campsite on the left hand side of the channel and settlements on the right hand side.

In the past, the Rotian channel produced three recorded debris-flow events. The 1776 event was described as a catastrophic phenomenon: the channel transported a large amount of sediment to the confluence with the Noce river stopping the flow and deviating its original path. In 1882 two debris-flow events of the same

magnitude hit the village destroying some settlements and depositing boulders in the fan area. More recently, in September 2000, the Rotian channel produced a small debris-flood event where most of the transported sediment was deposited upstream of the fan apex and the flow remained confined to the channel path.

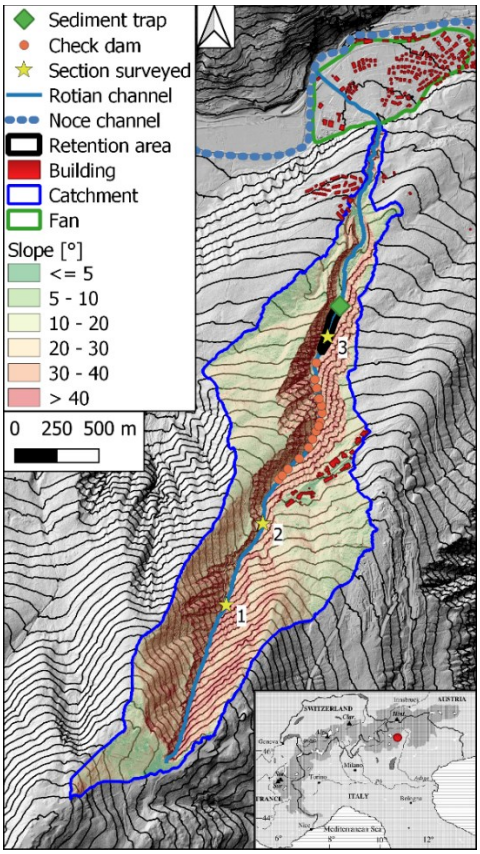

Figure 3.1: overview of the rio Rotian catchment and fan, showing the position of mitigation measures and the surveyed sections. In background the slope map. (contour lines altitude difference: 25m).

3.3.2 The 27-30th October 2018 event

Between the 27th and 30th October 2018 the North-Eastern Italian Alps were hit by an extreme storm, named "Vaia". The event was characterized by intense rainfall associated with high wind speeds, up to 200 km h^{-1} (Chirici et al., 2019). Focusing on the rio Rotian basin, the debris flow occurred at the end of the Vaia storm on the 29th October. The event was characterized by three different surges occurring at 19:02, 19:48 and 23:35 CET (Borga and Zaramella, 2020). An analysis of the rainstorm was carried out by Borga and Zaramella (2020) using the radar data of the Macaion station (located 32 km in the NE direction with respect to the fan apex). They calculated a total precipitation amount of 359 mm for the rio Rotian basin in the period 27 – 29th October, corresponding to a return period (three days maximum) of 300 years. Furthermore, the most intense precipitation occurred at the end of the event. A further rainfall analysis on the duration of the three hours before the event resulted in a return period of 100 years (Borga and Zaramella, 2020). The

basin, already stressed by two consecutive days of heavy rainfall, generated a catastrophic debris flow. The flow was characterized by major bed destabilization and erosion, which took place starting from the upper part of the basin. Propagating downward the flow increased its sediment component and destroyed the series of 15 check dams. The collapsed structures released debris that was engulfed by the flow causing a further bed instability and triggering a severe erosion process. The open check dam situated at 989 m a.s.l. retained a large quantity of the transported debris (32,000 m^3) but its storage capacity was not sufficient to effectively reduce the debris volume of such an extreme event. Consequently, the debris flow continued propagating downwards and flooded part of the fan, depositing a large volume of debris along the roads of the village (160,000 m^3). The flow affected several settlements and the campsite, causing severe damage and one fatality.

The debris flow was mainly formed by a fine sediment matrix (principally silt and sand) together with large rocks and boulders. According to field evidence, the debris flow can be classified as a muddy debris flow (Jakob et al., 2005). The front of the debris flow transported big boulders (diameters larger than 1 m and up to 6 m) depositing some of them in the fan, near the campsite (Figure 3.2A). A really big boulder (estimated volume of 18 m^3) was transported probably by the front of the flow and completely closed the open check dam (Figure 3.2B). Parts of the collapsed check dams were entrained in the flow and pieces were found in the retention basins (Figure 3.2C). In addition, the channel part upstream of the 15 consolidation check dams exhibited erosion and bank destabilization (Figure 3.2D).

Figure 3.2: pictures of the post-event conditions. The debris deposit at the campsite (A), the sediment trap (B), the check dam channel reach (C) and the upper part of the channel (D); the white and red lines represent the minimum and maximum debris-flow front height with respect to the channel bed.

Two days after the event (31st October 2018) the Mountain Basin Service of the Trento province performed a drone survey involving the fan area. Seven days later (7th November 2018) the Service surveyed the channel in the zone of the sediment trap and retention basin (1050 m a.s.l.), covering a torrent length of 350 m upstream of the check dam. Fifteen ground control points (GCP) were located within the surveyed area and their positions recorded with a high resolution GPS (estimated error of 0.05 m). The acquired images were processed to generate a point dense cloud and then a high resolution (0.1 m) digital surface model (Basin Mountain Service, 2018). Regarding the upper part of the channel that was not surveyed with the drone flight, we used the 2019 LiDAR data (acquired on 14-15th June 2019 with a 0.5 m resolution) as representative of the post-event conditions (no debris flood and flow events occurred between the October 2018 event and the LiDAR survey). Thanks to the pre-event LiDAR survey (acquired in 2014, 0.5 m resolution, error 0.1 m) we then performed a Dem of Difference (DoD) analysis, calculating the eroded and deposited volume pattern for the whole channel path and fan area. We used the minimum level of detection method (Brasington et al., 2003) to estimate the associated error. The DoD error is the result of the following equation $\delta u_{DoD} = \sqrt{\delta u_{pre}^2 + \delta u_{post}^2}$, where δu_{pre} and δu_{post} are the pre- and post-event associated DTM errors, respectively. The DoD analysis was the basis for the event reconstruction, input hydrograph, magnitude estimation and evaluation of the simulation performance.

On the 12th and 13th November we collected field data walking along the channel bed from the confluence with the Noce river to an elevation of 1480 m a.s.l. The grain-size distribution of the debris for three different sampling points was collected (two in the channel path and one in the retention basin). Also three channel sections were acquired in places where the estimated channel erosion was weak and where the maximum flow level was recognizable on both banks. For every section the upward thalweg profile was surveyed for a minimum distance of 25 m. The profiles and sections were surveyed measuring the horizontal and vertical distance with a TruePulse laser distance meter (accuracy 0.1 m). The maximum flow depth (sign of the passage on the banks), flow area and upward thalweg slope were derived. Empirical equations reported in the literature were used to back calculate the peak flow velocity (Hungr et al., 1984; Lo, 2000; Prochaska et al., 2008; Rickenmann, 1999) and consequently the peak discharge. The general form of velocity [m/s] empirical equation is $v = a\left(H^b S^c\right) + d$ where H is the flow depth [m], S the slope [m/m] and *a, b, c, d* are empirical coefficients reported in Table 3.1. The calculated peak discharge was compared with the empirical equation of Benini (2000), which considers the threshold for motion velocity of a sediment particle transported by a debris flow (in this case we considered the maximum particle diameter D that was moved):

$$v = \left[21.8\frac{(\gamma_s - \gamma)}{\gamma}\right]^{0.5} D^{0.5} \tag{3.1}$$

where γ_s and γ are the specific weights of the particle and flow, respectively.

Using the DoD map the erosion upstream section 1 was derived to calculate the debris volume. For further verification, the obtained value is compared with empirical relationships (Mizuyama et al., 1992).

Based on the peak discharge and total solid volume estimation, for a modelling aim an input hydrograph with a triangular shape was derived, fixing the volumetric concentration of the solid component to 0.5 (Gregoretti et al., 2018).

3.3.3 Simulation model and input data

To back calculate the debris flow, the simulation tool r.avaflow version 2.4 was adopted (Mergili and Pudasaini, 2021). The tool implements the multi-phase mass flow model described in (Pudasaini and Mergili, 2019). The model can simulate the propagation of different types of mass flows down a general topography. The mass can be introduced in the calculation domain simultaneously or alternatively through a hydrograph (discharge versus time relation) or a release mass (raster map). An additional function of the model is the possibility of releasing the mass from a certain cell at a given time.

Implementing r.avaflow for the Rotian debris-flow event, the multi-phase model was reduced to a two-phase model, considering the solid component as debris material and the fluid one as water. The selected flow parameters are basically the same values reported in the user manual (Mergili and Pudasaini, 2021). We varied two flow parameters in order to reproduce the rheology of a muddy debris flow. In particular, the basal friction angle was decreased to 16° and the fluid kinematic viscosity increased to 0.005 m^2s^{-1}. Furthermore, the tool provides an empirical multi-phase erosion model, calculating for each time step (Δt) the entrained volume in terms of erosive depths D_E by means of the following function of the flow momentum (M) (Eq. 3.2 and 3.3):

$$D_{E,s} = C_E \left| M_s + M_f \right| \alpha_{s,Emax} \Delta t \tag{3.2}$$

$$D_{E,f} = C_E \left| M_s + M_f \right| \left(1 - \alpha_{s,Emax}\right) \Delta t \tag{3.3}$$

Where C_E is the coefficient of erosion, $\alpha_{s,Emax}$ the sediment volumetric concentration of the eroded material and M is the flow momentum. The subscripts s and f refer to the solid and fluid phase of the flow, respectively.

The erosion model requires the assignment of C_E, $D_{E,max}$ maximum erosion depth, and $\alpha_{s,Emax}$. These parameters are defined by the user alternatively as a single value or spatially distributed (raster map). The maximum erosion depth was set to 10 m (maximum erosion observed) but erosion was not permitted in correspondence to the retention basin and sediment trap, since in those locations the channel bed was reinforced with stones. Indeed, $\alpha_{s,Emax}$ was set to 0.7, representing the water saturated pre-event soil conditions. The value is similar to that observed in the triggering area of two debris-flow basins of Eastern Alps (Gregoretti et al., 2019, 2018). Deposition is considered as the remaining mass at the end of the simulation time; in this study it is fixed to 3000 s (50 min) for all simulations performed.

Regarding the DTM, the 2014 LiDAR derived terrain model was used, representing the pre-event conditions. The original DTM was resampled from a resolution of 0.5 m to 2 m for computational speed, adopting a mean value method. The DTM was further modified to represent the open check dam, since it was under construction in 2014. It has been represented as a rigid wall since the opening had been closed by a big boulder, likely transported by the front of the debris flow. We located the input hydrograph 830 m upstream of the first check dam in correspondence to the surveyed section 1 (Figure 3.1).

To reproduce the Rotian debris flow three scenarios representing three different ways to implement the check dam collapse were tested:

A. Scenario representing the propagation of the debris flow over an erodible channel bed (check dams are considered erodible). C_E is a function of a smoothed slope (S_S [%], calculated as the mean value within a circular moving window of 5x5 cells) as the most performing function calibrated in (Baggio et al., 2021) for debris-flow entrainment over erodible channel.

$$C_{E,exp6} = 10^{(0.02S_s - 6.75)} \quad (3.4)$$

Moreover, the smoothed slope dependent function was varied in the channel reach between the input hydrograph location and the check dam 01 (Area 1, Figure 3.4) in order to further improve the reliability of the erosion model. In Area 1 the simulated eroded volumes adopting the function of eq. 3.4 resulted considerably higher than the observed one. Other two functions were tested (reported in Baggio et al., 2021) to simulate erosion in Area 1, always based on a smoothed slope:

$$C_{Eexp2} = 10^{(0.025S_s - 7)} \quad (3.5)$$

$$C_{Eexp3} = 10^{(0.03S_s - 7.5)} \quad (3.6)$$

B. Scenario of a debris-flow propagation over a non-erodible channel bed. The check dam collapses are reproduced by debris material released for every check dam. To calculate the release volume an upward sliding failure slope of 25° was supposed (angle of repose of debris soaked material; assessed by means of local surveys of terrain collapses after the events) as the result of the lack of bed stabilization provided by the check dam Figure 3.3. The depth of the released material is then calculated as the difference between the original topography (input DTM) and the assumed failure slope plane. The calculated mass retained by the check dam is released at the passage of the simulated debris-flow peak discharge (estimated with a previous simulation). The solid mass released for every check dam results variable in accordance with its height as highlighted in the sketch of Figure 3.3 and the solid ratio has been set to 0.8. Such mass was released considering only the channel bed using a mask layer. An example of the final released mass height distribution of a check dam collapse is represented in Figure 3.3. The calculation was implemented as a pre-processing algorithm in the same script to launch the mass flow propagation with r.avaflow. The input data required for every check dam is a polyline

identifying the downstream border of the check dam step and a mask outlining the upstream channel bed. It is also possible to adapt the algorithm to reproduce a partial collapse of a check dam in terms of height or width. In the first case (height under collapse) it is just necessary to modify the elevation value of the lowest border of the computer generated slope. In the second case (work width under collapse) the channel mask can be modified to simulate the check dam collapse for a particular area of interest.

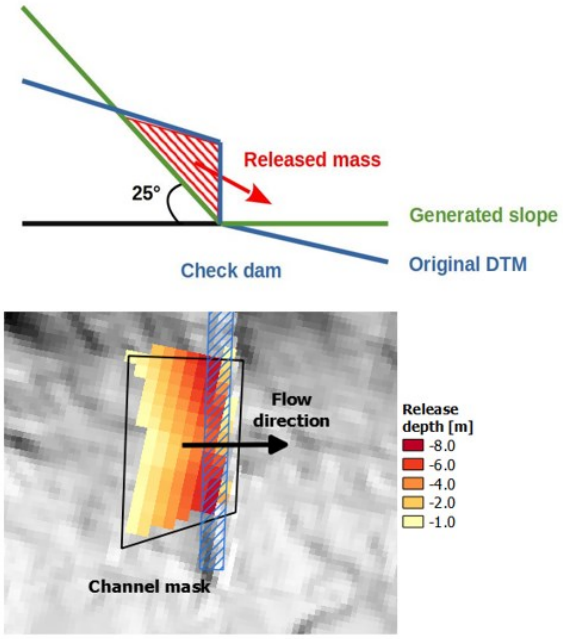

Figure 3.3: profile sketch and plan view of the release depth calculation for the simulation of a check dam collapse.

C. Scenario representing a combination of the previous two scenarios. The mass representing the check dam collapse is calculated and released at the peak discharge passage as explained in B. Moreover, erosion is allowed in the computational domain and C_E has been set to a unique value for the whole computational domain. Six simulations were performed where C_E was progressively varied from 10^{-7} to $10^{-6.2}$ kg^{-1} in order to calibrate the erosion coefficient in accordance with the observed erosion volume of the check dam series in the torrent reach under analysis.

To evaluate the best scenario the observed net balance (difference between deposited and eroded volumes) was compared with those simulated for two selected channel reaches. Area 1 represents the channel reach between the input hydrograph until 50 m upstream of check dam 1 while area 2 encloses the channel part of the check dam series (Figure 3.4). In particular, a simulation was considered accurate when it reproduces the balance volume within an error of 20% with respect to the observed value.

3.4 Results

3.4.1 Hydrograph reconstruction

Hydrograph reconstruction was based on the calculation of the solid volume (DoD map) and on the peak discharge reconstruction. Adopting empirical relations, the mean velocity was derived for the debris-flow front. Then, the bulked peak discharge was calculated through the product of the wet area surveyed in the field and the flow velocity of the front.

A total of three channel sections and the related upstream channel profile were surveyed, collecting their horizontal and vertical coordinates with respect to a reference point (locations are reported in Figure 3.1). The maximum flow depth that occurred during the 29th October 2018 event, the upward thalweg slope and wet area were estimated. Through the empirical equations, the peak discharges were derived, which are listed in Table 3.1. For section 1 the maximum flow depth was modified, decreasing the value of 1.5 m. In fact, it was assumed that the channel deepening to the bedrock was caused by the tail of the debris flow and not by the front surge under estimation. A sign of such front passage can be identified in the channel banks, (Figure 3.2D, white and red lines). The modification of the bed bottom position were supported by information on the bed topography from the DoD map.

Table 3.1: discharge peak reconstruction of the surveyed sections through empirical equations derived from field data. The suffix "mod" means that the surveyed max flow depth has been modified. We also report the empirical equations to calculate the max flow velocity and consequently peak discharge.

				Velocity [m s^{-1}]				*Peak discharge [m^3 s^{-1}]*				
Section ID	*Max flow depth [m]*	*Wet area [m^2]*	*Slope [m m^{-1}]*	*Hungr et al. (1984)*	*Lo (2000)*	*Rickenmann (1999) & Lo (2000)*	*Rickenmann (1999)*	*Hungr et al. (1984)*	*Lo (2000)*	*Rickenmann (1999) & Lo (2000)*	*Rickenmann (1999)*	*Mean*
				$v=0.55H^{3/2}S^{1/2}+4.59$	$v=3.32H^{2/3}S^{1/5}+0.70$	$v=4.47H^{2/3}S^{1/2}+1.71$	$v=8.90H^{0.30}S^{1/2}+1.06$	*Velocity x Wet area*				
SEZ. 1	3.3	25.4	0.41	6.7	5.4	8.0	8.6	169.3	136.7	203.6	218.3	187.0
SEZ. 1 mod	1.8	15.8	0.41	5.4	3.8	5.9	6.6	85.2	59.7	92.5	103.5	78.3
SEZ. 2	3.5	46.5	0.20	6.2	4.1	6.3	6.4	287.9	190.5	292.2	300.0	267.6
SEZ. 3	8.3	237.4	0.17	9.9	6.2	9.2	8.7	2354.4	1481.4	2176.8	2064.4	2019.3
SEZ. 3 mod	5.8	82.6	0.17	7.7	5.1	7.6	7.5	638.8	419.8	628.6	616.2	575.9

The calculation of the peak discharge of section 1 is particularly important, since it is the basis for the construction of the input hydrograph for the simulation model. From Table 3.1 it is possible to identify the peak discharge of section 1 that for the modified section resulted 78 m^3s^{-1}, calculated as the mean of the empirical equations. The estimated total solid volume from the DoD map resulted 33,600 m^3. The value is computed as the erosion rate per channel length between section 1 and 2 (equal to 32 m^3m^{-1} according to the DoD) multiplied by the channel length upstream of section 1 (1050 m). The estimation has been performed due to the impossibility to compute a reliable DoD map upstream of section 1 (presence of vegetation cover within the channel and steep slopes not well captured by the post-event survey). Using the equation of Mizuyama et al. (1992) the solid volume associated to the peak discharge of 78m^3s^{-1} resulted

37,237 m^3. The statistical analysis of debris flows occurring in the Eastern Alps by Marchi and D'Agostino (2004) corroborated the debris volume of such an event. According to these authors, the maximum debris volume (V_s) related to the upper catchment area A [km^2] is given by the upper envelope equation: V_s =70,000 A, calculating a value of 41,300 m^3 for section 1 (upper catchment area of 0.59 km^2). This value is in line with the debris volume derived from the DoD map upstream of the section 1. Furthermore, the peak discharge in section 1 was confirmed by means of the limiting equation (Eq. 3.1) for boulder entrainment (max grain diameter 1.0 m), obtaining a value of 81.6 m^3s^{-1}. The comparison with equations reported in the literature and the DoD analysis confirmed that the calculated peak discharge and associated debris volume can be consistently representative of the investigated event.

We then used these values to build up an input hydrograph with a triangular shape in accordance with field observations (Berti et al., 2000; Gregoretti et al., 2019; Kean et al., 2012). We fixed the peak discharge at 100 s after the hydrograph starts. After the peak, the discharge progressively decreased to zero in a total time of 956 s. The solid volumetric concentration was set to 0.5 since the event was mainly triggered by the movement of the soaked bed deposits within the whole channel path and eye witnesses reported the passage of a dense debris flow.

Regarding the section 2 the estimated peak discharge is equal to 267 m^3/s (mean of all equations). However, this value is probably overestimated since the tail of the debris flow eroded the channel bed increasing the apparent maximum flow depth, that was measured in the field. Besides, the estimated peak discharge of the section 3 was assessed in 575 m^3/s (mean of all equations, Table 3.1). Also in this case, the discharge assessment is uncertain since a deposition followed by an intense bed erosion influenced maximum flow depth measure.

3.4.2 Erosional and depositional pattern analysis

The DoD was computed as the difference between the 2019 and 2014 DTM. For our objective, involving the check dam collapse simulation, the focus was on the channel reach between the input hydrograph location (section 1, Figure 3.1) and the last downstream check dam (right upstream of the retention basin). Two areas of interest were defined for the calculation of the eroded and deposited volumes (Figure 3.4). The error associated with the DoD map resulted 0.14 m and, adopting the minimum level of detection method, the eroded and deposited volumes within the two areas were calculated (Table 3.2).

In the investigated areas the erosion processes resulted predominant with respect to the depositions one. For Area 1 (comprised between 1435 and 1238 m a.s.l for a length of 817 m) intense erosion was observed, with an associated volume balance per channel length of 31 m^3m^{-1}. In Area 2 (covering the torrent reach between 1238 and 1029 m a.s.l for a length of 852 m) the erosion process became more severe. In this channel segment the erosion resulted 119 m^3m^{-1}. The net balance between eroded and deposited volumes consisted in −25,630 m^3 (± 1855) and 102,393 m^3 (± 4110) for Area 1 and 2 respectively. The erosion depth per channel length in Area 1 is typical of debris-flow triggering reaches, while the high values of Area 2 is the combined result of the check dam collapses and the successive bed erosion process. As to those areas

not directly investigated in this study, the volume balance was computed for the zone of the retention basins (from just downstream of Area 2 to the open check, altitude range 1029–989ma.s.l., length 290m) resulting in a net balance in favour of deposition of 20,048 m^3 (± 2831). The reach downstream of the open check dam up to the municipal road (altitude range 1029–928 m a.s.l., length 531 m) exhibited erosion processes characterized by a net balance of −18,447 m^3.

*Table 3.2: analysis of the volume balance (deposition – erosion) based on the DoD map and comparison with the simulated scenarios. * Represents the balance error of the DoD for the investigated area.*

	Area 1			***Area 2***		
Scenario	*Volume balance (deposited – eroded) [m^3]*	*Error (simulated / observed)*	*Volume / channel length [m^3/m]*	*Volume balance (deposited – eroded) [m^3]*	*Error (simulated / observed)*	*Volume / channel length [m^3/m]*
Observed	-25,630	1,855*	-31.4	-102,393	4,110*	-119.2
Scenario A (C_E: Area 1 -> $C_{E,exp2}$; Area 2 -> $C_{E,exp6}$)	-28,732	1.12	-33.72	-99,492	0.98	-116.8
Scenario B (mass release – without erosion)	0	-	0.0	-22,304	0.22	-26.2
Scenario C (mass release and erosion, $C_E = 10^{-6.4}$)	-30,864	1.20	-36.2	-109,096	1.07	-128.1

3.4.3 Scenario results

Three scenarios A, B, C were computed, releasing the selected input hydrograph in section 1. Scenario A involved the flow propagation over an erodible channel, scenario B the release of a mass for every check dam (sketch in Figure 3.3) and scenario C was a combination of bed erosion and mass release. The total volume released by the collapse of the check dam series at the passage of the peak discharge is equal to 22,304 m^3 (scenario B and C). The erosion and deposition patterns of the performed simulations are illustrated in Figure 3.4. For scenarios A and C were showed only the simulations best matching the observed erosion rates. For scenario A, the best performing simulation is the result of the combination of two C_E functions ($C_{E,exp2}$ for Area 1 and $C_{E,exp6}$ for Area 2, Eqs. 3.5 and 3.4 respectively). Regarding scenario C the chosen C_E coefficient is $10^{-6.4}$ kg^{-1}. In Table 3.2 the comparison between the observed and simulated erosion and deposition volumes is reported. For Area 1, representing the channel reach between the input hydrograph and the first check dam, scenario A performed best, resulting in a relative error of 12% of additional erosion with respect to the observed value. Scenario C predicted a slightly greater volume of eroded sediment volume respect to scenario A with an overestimated error for erosion of about 20%. The simulated erosion patterns of scenarios A and C resulted slightly different in Area 1. In particular, in the scenario A erosion was more variable (more intense for steeper slopes) than in the scenario C for which erosion resulted steadier with a more intense process upstream than check dam 01. Anyway, both scenarios accurately represented the erosion pattern observed in Area 1, since the relative error resulted equal to or lower than 20%. Obviously, in the scenario B no erosion occurred since it has not been permitted in the computational domain. Regarding Area 2, representing the check dam series, both scenarios A and C represented the observed eroded volume satisfactorily and provided a relative error of −2 and 7%

respectively. Instead scenario B predicted just a small amount of eroded/released material (22,304 m^3) corresponding to the released debris of the check dam collapses only.

Regarding the erosion pattern in Area 2, we can notice an observed intense erosion process upstream of check dam 01 and between check dam 08 and 11 with associated erosion depths reaching a maximum of 11 m. Moreover, for check dam 06 erosion occurred both upstream and downstream of its position. For check dams 02, 04 and 05 erosion mainly occurred downstream, while for check dams 01 and 03 it occurred mostly upstream. Regarding Area 2 (check dam series), scenario A and C exhibited a similar pattern. Scenario A eroded a large amount of material in correspondence and downstream of the check dams while scenario C generated erosion both upstream and downstream. Even if scenarios A and C are both considered adequate to reproduce the observed eroded pattern, the two simulations have a different approximation in the process representation. The operative procedure developed for scenario C resulted more reliable to simulate the effect of check dam collapse than scenario A, since scenario C released the mass retained by the check dams at the passage of the peak discharge. The hydrograph in Figure 3.5B of scenario C captured this aspect of impulsive mass release as highlighted by a greater peak discharge than scenario A.

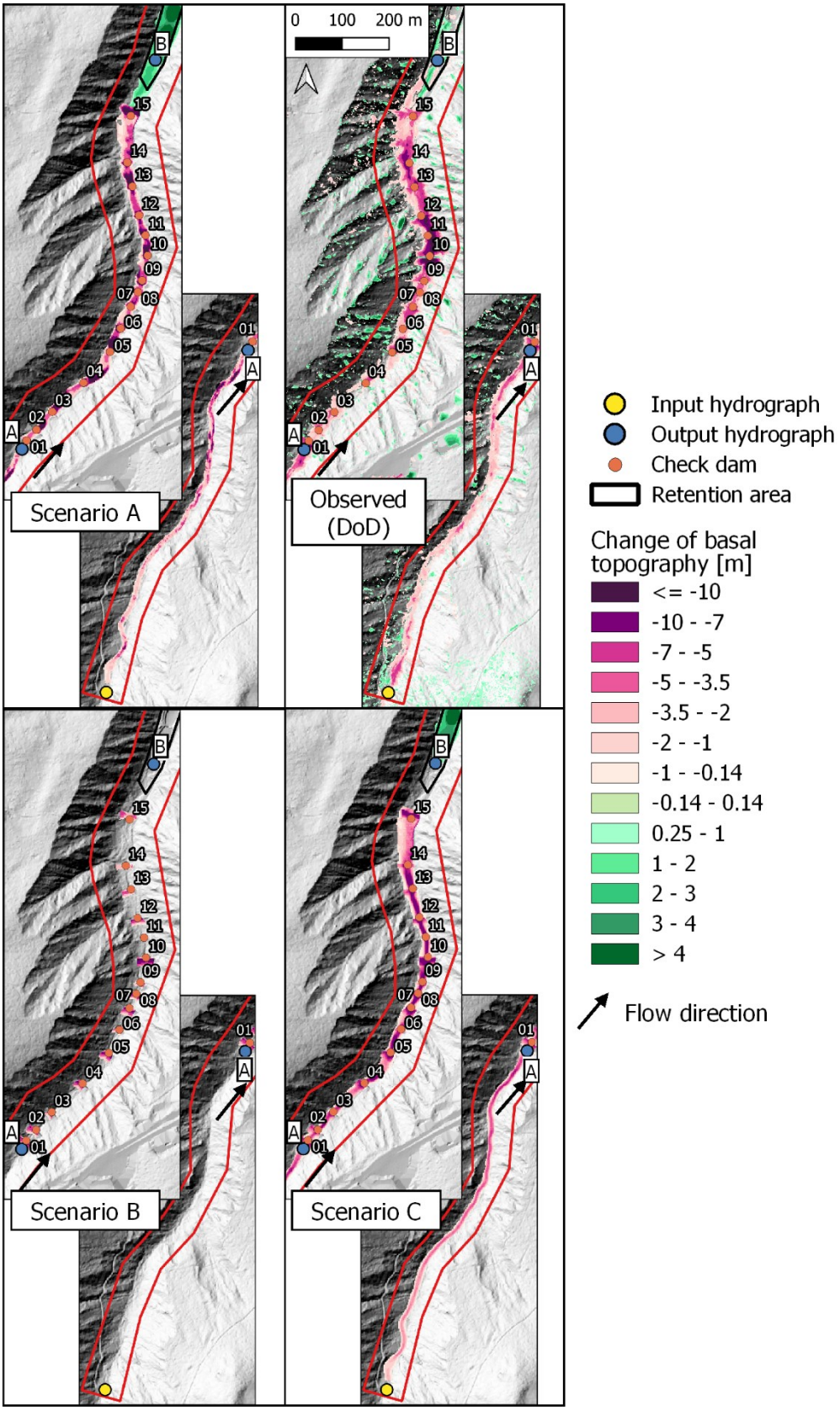

Figure 3.4: maps representing the observed erosion and deposition depths (DoD) and simulated elevation changes respect the basal topography for scenarios A, B and C.

The output hydrographs reported in Figure 3.5 show the discharge (debris and fluid component) and solid concentration variation over time for location A and B highlighted in Figure 3.4. In location A scenarios A and C predicted similar maximum discharges, equal to 107 and 121 m^3s^{-1}, respectively. Instead, scenario B produced the same discharge as the input hydrograph (78 m^3s^{-1}), since entrainment was not permitted. Regarding the volumetric solid concentration, scenario A and C showed a stable value around 0.58, while for scenario B it resulted lower, equal to the input hydrograph (0.5, constant for the whole passage of the debris flow). Regarding the output hydrograph in location B, scenario C predicted the highest discharge equal to 99 m^3s^{-1}, while scenario A and B resulted 75 and 43 m^3s^{-1}, respectively. Scenario A and C exhibited a first surge in the front, followed by a higher peak. The discharge of the front surge of scenario C resulted greater than scenario A as consequence of the mass released in the proximity of output location B. The solid concentration pattern showed a higher value in the front (range 0.6–0.65) and it immediately decreased around 0.55 until 17 min of simulation time. Afterward the solid concentration constantly increased to reach values around 1 at the end of the simulation time. This behaviour is the result of the deposition process caused by the open check dam. The biphasic representation of the flow simulated aggradation of the solid component in this area, while the fluid component slowly separated, flowing downstream. The phenomenon is captured by the increase of the solid concentration towards 1.

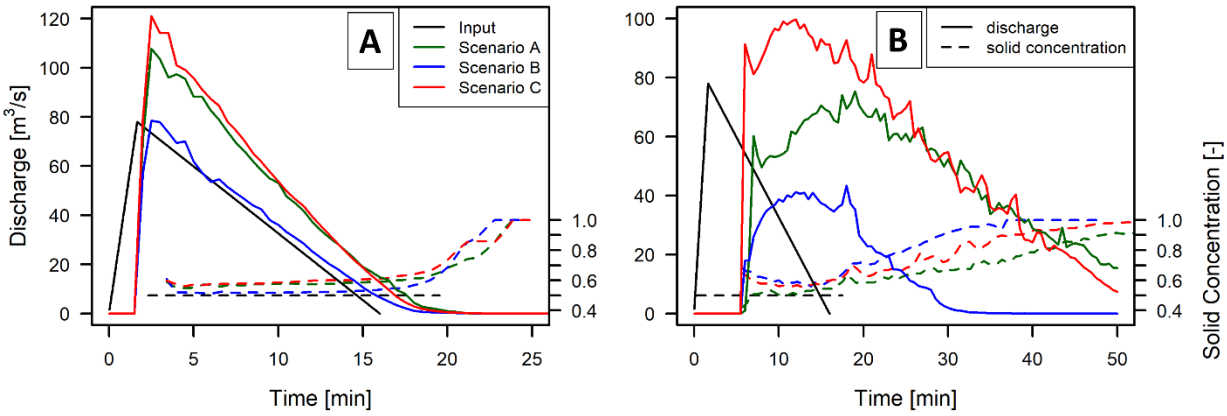

Figure 3.5: Hydrographs representing the total discharge (solid + fluid) and solid concentration over time of the simulation scenarios. The input hydrograph is reported for comparison. The locations are reported in Figure 3.4.

3.5 Discussion

In this study the Rio Rotian debris-flow event that occurred on the 29th October 2018 was reconstructed. The peak discharge was first estimated in the triggering area and then three different scenarios were performed using the simulation model r.avaflow, aiming to reproduce the effects of check dam collapses during the event. The simulation performance were analysed and evaluated using the observed erosion and deposition volumes derived from the DoD map.

The event peak discharge and total volume at section 1 were evaluated with the DoD analysis and confirmed by the equations of Benini (2000) and Marchi and D'Agostino (2004). Some uncertainties still remain in the estimation of the hydrograph shape due to the impossibility of the discharge time pattern evaluation after the peak passage. However, the choice of a linearly shaped hydrograph is also supported by the

observations of two high magnitude debris flows recorded in the triggering area (Simoni et al., 2020). The same pattern has been observed in the routing area by Berti et al. (2000) and Kean et al. (2012). In addition, also varying the discharge pattern, the simulation results in terms of erosion may not vary consistently, since the erosion function is strictly dependent on the flow momentum and its highest value occurs in correspondence of the debris-flow front (Berger et al., 2011; McCoy et al., 2012). Regarding section 2 and 3, their geomorphological conditions did not allow a reliable reconstruction of the peak discharge. In section 2, the channel bed erosion process did not permit a reliable estimation of the debris-flow front. Instead, for section 3 the peak discharge evaluation resulted uncertain because of the large amount of debris deposited. Therefore, the estimated peak discharge in section 2 and 3 (Table 3.1) could not be used for the evaluation of the investigated scenarios.

Regarding the DoD we compared the eroded volumes per channel unit with other observations reported in the literature in order to estimate its magnitude. Regarding Area 1 (natural channel bed) the erosion resulted 31 m^3m^{-1}, which is a high value compared with other studies in the Alps (Marchi and Cavalli, 2007; Marchi and D'Agostino, 2004). For Area 2 (check dam series), erosion resulted 119 m^3 per channel unit length and can be considered as an extreme value for the eastern Alps (Marchi and Cavalli, 2007) and even worldwide (Hungr et al., 2005; Rickenmann and Zimmermann, 1993). However such a high erosion value is the consequence of check dam collapse and is fully comparable, in terms of geomorphological estimation of debris-flow volumes, to that associated to a triggering area. Analysing erosion in Area 2, this occurred predominantly upstream and downstream of the check dam location (Figure 3.4). Deposition process started just downstream of check dam 15 where the channel slope becomes gentler due to the presence of the retention basins (mean channel slope of the first deposit equal to 8.4°). More importantly, we observed that: i) the spatially distributed bed erosion is the dominant mechanism in debris-flow entrainment in the case of check dam failure; ii) this erosive pattern is not particularly different from that obtainable in the absence of check dams and it cannot be expected in a particular reach of the torrent (e.g., always downstream of the collapsed work; Figure 3.4). In fact, the total eroded volume (102,393 m^3) is around five time greater than the volume estimated and released by the collapse of the 15 check dams (22,304m^3) reported in scenario B (a sketch for the calculation of the volume released is reported in Figure 3.3). Therefore, the principal cause of debris-flow growth is represented by bed erosion as consequence of check dams collapse. A similar phenomenon is reported in Benito et al. (1998), where the collapse of retention dams triggered an extreme debris-flow event in the Biescas basin (Spain). Similarly to the Rotian channel, the Biescas debris flow acquired debris from incision into the unconsolidated glacial deposits after the barrier collapse. A similar mechanism of entrainment is also reported in Chen et al. (2015) and Gong et al. (2020), where the collapsed check dams destabilized the channel bed, permitting an intense bed erosion process.

Regarding the simulations, scenarios A and C successfully reproduced the observed erosion volume of the check dam series (relative error ≤ 20%). In particular, in scenario C a simulation representing the effect of check dam collapse was set up, calibrating an erosion coefficient based on the observed eroded volume. A semiautomatic procedure was developed to derive the spatially distributed volume retained by the check

dams. The effect of check dam collapse was then simulated through mass release in the computational domain synchronised with the peak discharge passage. Furthermore, as observed from scenario C, the calibrated C_E coefficient was also appropriate to reproduce the erosion pattern of Area 1 (natural channel bed). Thanks to the DoD map the observed erosion pattern was reproduced as a combination of two smoothed slope dependent erosion functions reported in Baggio et al. (2021). For Area 1, where the erosion process resulted less intense, (channel reach upstream of the check dam series) we validated the function C_{Eexp2} (Eq. 3.5). Instead for Area 2 (channel reach containing the collapsed check dams) the function C_{Eexp6} (Eq. 3.4) represented better the erosion process. Then, it is possible to conclude that the effect of check dam collapse can be calibrated according to the reach erodibility by simulating this intense erosion process similarly to a natural debris- flow channel.

Based on all results, scenario C resulted more precise and then appropriate to simulate check dam collapse than scenario A. However, the simulation setup of scenario A could also be used for check dam collapse simulation, but disregarding real local erosion at the check dam locations and aiming to focus only on the total amount of entrained debris from the channel bed. Accepting this approximation, the simulation setup results easier since it does not require the input on the check dams position and a mask to extract the channel bed area.

The verifications through alternative modelling scenarios also confirmed the outcomes of other studies that highlighted the importance of a careful simulation of debris-flow erosion (Armanini et al., 2009; Gregoretti et al., 2019; Kean et al., 2013). This is always necessary in case the travelling surge suffers a clear modification of its sediment concentration at equilibrium conditions driven by the bed slope, according to Takahashi (2007), or due to the input of supplementary water discharge (e.g. inflow from a tributary branch) or due to the release of supplementary debris (e.g. check dam failure as in our case). For such reasons simulation tools that include the erosion process have to be adopted for the delineation of hazard and risk maps.

In the last decades, attention towards debris-flow structure effectiveness and potential failure consequences has been rising due to their age and lack of maintenance, together with the increasing number of people living in high risk zones (Mazzorana et al., 2014). In particular, different studies pointed out that effectiveness assessment of mitigation structures has to consider potential failures (Chen et al., 2015; Dell'Agnese et al., 2013; Piton et al., 2016). Thanks to our back-analysis two joint scenarios for the simulation of a check dam series collapse were defined and successfully performed. Other studies investigated the debris flow – check dam interaction. Cui and Chen (2021) and Ferrari et al. (2010) analysed the dam break effect on laboratory experiments and successfully reproduced the observed behaviour with numerical models. Chen et al. (2019) and Marchelli and De Biagi (2019) examined the check dam failure condition and debris-flow surge impacting the check dam through simulation models. Sodnik et al. (2013) proposed a qualitative approach for the evaluation of the hazard level in case of check dam failure. In the mentioned studies some limitations result from the investigation on small scale experiments, the use of

single – phase and rigid bed propagation models. The present study, thanks to the availability of a well documented catastrophic event and a specific implementation of the r.avaflow model, overtakes these limitations and it demonstrates a good performance for a complicate real case. The proposed procedure can be directly applied to investigate and assess the potential effects of check dam failure in those torrents where mitigation structures may partially or totally fail. Such a simulation is also capable of driving our decision on maintaining or not ancient check dams in torrents that have been heavily managed in the last centuries (1800 and 1900) and where the erosion control works are in remote wild valleys with difficult access for vehicles and manpower. The results could be used to update the actual debris-flow risk assessment maps (Mazzorana et al., 2009) and help civil authorities in raising residents' awareness of debris-flow events.

3.6 Conclusions

The study described a catastrophic debris-flow event occurred in the Eastern Italian Alps at the end of the Vaia storm (October 2018). The event was characterized by the collapse of 15 check dams, which destabilized the channel bed. The entrained material increased the debris-flow volume causing sever damages in the fan area. Thanks to the LiDAR and field data, the depositional-erosional pattern of the debris flow was successfully reconstructed. Three complementary different scenarios were implemented to simulate the check dam collapse through bed erosion and mass release. For two of the proposed scenarios, a semi-automatic procedure was developed to calculate the mass release in the case of check dam collapse. The adopted mass flow model r.avaflow resulted particularly suitable for this purpose due to its flexibility in introducing the mass within the computational domain. The observed debris-flow entrainment process in the check dam area mainly occurred through bed erosions rather than released masses. In fact, the total eroded volume resulted five times greater than the estimated volume released by the fifteen check dams (scenario B). The results, together with other companion literature findings, suggest that the effect of check dam failures is often over-estimated as to its power in magnifying the damage. The coefficient of erosion calibrated in Baggio et al. (2021) also resulted suitable to predict the eroded volumes as consequence of check dam failure. This scenario could be immediate to implement for an approximate simulation of the effect of check dam failure.

Summarizing all our findings, we can state that, in the lack of a model capable to simulate check dam collapse and debris flow erosion with a unique simulation, the proposed procedure resulted to be suit- able to update the hazard maps in debris-flow channels where mitigation structures are getting old, and to reduce the possible consequences for citizens and infrastructures.

Acknowledgements

This research received funding as part of the project “Bridging the mass-flow modelling with the reality”, from the CARIPARO foundation (2724/2018). The study was additionally funded by Provincia Autonoma di Trento through Accordo di Programma GPR. Authors wish to thank the Mountain Basin Service of the Autonomous Province of Trento (IT) for the post-event data and they are also grateful to the three reviewers for their useful suggestions and comments.

3.7 References

Armanini, A., Fraccarollo, L., Rosatti, G., 2009. Two-dimensional simulation of debris flows in erodible channels. Computers and Geosciences 35, 993–1006. https://doi.org/10.1016/j.cageo.2007.11.008

Armanini, A., 2015. Closure relations for mobile bed debris flows in a wide range of slopes and concentrations. Adv. Water Resour. 81, 75–83. https://doi.org/10.1016/J.ADVWATRES.2014.11.003

Baggio, T., Mergili, M., D’Agostino, V., 2021. Advances in the simulation of debris flow erosion: The case study of the Rio Gere (Italy) event of the 4th August 2017. Geomorphology 381, 107664. https://doi.org/10.1016/j.geomorph.2021.107664

Baggio, T., Mergili, M., Pudasaini, S., Carter, S., Fischer, J., 2018. Simulating snow process chains: avalanche-river interactions with r.avaflow, in: International Snow Science Workshop. Innsbruck, pp. 792–796.

Basin Mountain Service, 2018. Post-event photogrammetric survey of the rio Rotian (original title, in italian: Rilievo fotogrammetrico post evento del rio Rotian.

Benini, G., 2000. Sistemazioni idraulico forestali. UTET — Unione Tipografico-Editrice Torinese, Torino, IT.

Benito, G., Grodek, T., Enzel, Y., 1998. The geomorphic and hydrologic impacts of the catastrophic failure of flood-control-dams during the 1996-Biescas flood (Central Pyrenees, Spain). Zeitschrift fur Geomorphologie 42, 417–437. https://doi.org/10.1127/zfg/42/1998/417

Berger, C., McArdell, B.W., Schlunegger, F., 2011. Direct measurement of channel erosion by debris flows, Illgraben, Switzerland. J. Geophys. Res. Earth Surf. 116, n/a-n/a. https://doi.org/10.1029/2010JF001722

Bernard, M., Boreggio, M., Degetto, M., Gregoretti, C., 2019. Model-based approach for design and performance evaluation of works controlling stony debris flows with an application to a case study at Rovina di Cancia (Venetian Dolomites, Northeast Italy). Science of the Total Environment 688, 1373–1388. https://doi.org/10.1016/j.scitotenv.2019.05.468

Berti, M., Genevois, R., LaHusen, R., Simoni, A., Tecca, P.R., 2000. Debris flow monitoring in the acquabona watershed on the Dolomites (Italian alps). Physics and Chemistry of the Earth, Part B: Hydrology, Oceans and Atmosphere 25, 707–715. https://doi.org/10.1016/S1464-1909(00)00090-3

Borga, M., Stoffel, M., Marchi, L., Marra, F., Jakob, M., 2014. Hydrogeomorphic response to extreme rainfall in headwater systems: Flash floods and debris flows. Journal of Hydrology 518, 194–205. https://doi.org/10.1016/j.jhydrol.2014.05.022

Borga, M., Zaramella, M., 2020. Evento di piena del 27-29 ottobre 2018 sul bacino del Rio Rotian: stima della precipitazione e valutazione della sua severità.

Brasington, J., Langham, J., Rumsby, B., 2003. Methodological sensitivity of morphometric estimates of coarse fluvial sediment transport. Geomorphology 53, 299–316. https://doi.org/10.1016/S0169-555X(02)00320-3

Chen, H.X., Li, J., Feng, S.J., Gao, H.Y., Zhang, D.M., 2019. Simulation of interactions between debris flow and check dams on three-dimensional terrain. Engineering Geology 251, 48–62. https://doi.org/10.1016/j.enggeo.2019.02.001

Chen, X., Cui, P., You, Y., Chen, J., Li, D., 2015. Engineering measures for debris flow hazard mitigation in the

Wenchuan earthquake area. Engineering Geology 194, 73–85. https://doi.org/10.1016/j.enggeo.2014.10.002

Cucchiaro, S., Cavalli, M., Vericat, D., Crema, S., Llena, M., Beinat, A., Marchi, L., Cazorzi, F., 2019a. Geomorphic effectiveness of check dams in a debris-flow catchment using multi-temporal topographic surveys. Catena 174, 73–83. https://doi.org/10.1016/j.catena.2018.11.004

Cucchiaro, S., Cazorzi, F., Marchi, L., Crema, S., Beinat, A., Cavalli, M., 2019b. Multi-temporal analysis of the role of check dams in a debris-flow channel: Linking structural and functional connectivity. Geomorphology 345, 106844. https://doi.org/10.1016/j.geomorph.2019.106844

Cui, P., Chen, J., 2021. Numerical simulation of dam-break mudflow based on the Herschel- Bulkley model, in: EGU. p. 6979.

Dell'Agnese, A., Mazzorana, B., Comiti, F., Von Maravic, P., D'Agostino, V., 2013. Assessing the physical vulnerability of check dams through an empirical damage index. Journal of Agricultural Engineering 44, 9–16. https://doi.org/10.4081/jae.2013.e2

Dowling, C.A., Santi, P.M., 2014. Debris flows and their toll on human life: A global analysis of debris-flow fatalities from 1950 to 2011. Natural Hazards 71, 203–227. https://doi.org/10.1007/s11069-013-0907-4

Ferrari, A., Fraccarollo, L., Dumbser, M., Toro, E.F., Armanini, A., 2010. Three-dimensional flow evolution after a dam break. Journal of Fluid Mechanics 663, 456–477. https://doi.org/10.1017/S0022112010003599

Frank, F., McArdell, B.W., Huggel, C., Vieli, A., 2015. The importance of entrainment and bulking on debris flow runout modeling: Examples from the Swiss Alps. Natural Hazards and Earth System Sciences 15, 2569–2583. https://doi.org/10.5194/nhess-15-2569-2015

Fuchs, S., Heiss, K., Hübl, J., 2007. Towards an empirical vulnerability function for use in debris flow risk assessment. Natural Hazards and Earth System Science 7, 495–506. https://doi.org/10.5194/nhess-7-495-2007

Gentile, F., Tiziana, A.E., Ae, B., Liuzzi, G.T., 2007. Debris-flow risk analysis in south Gargano watersheds (Southern-Italy). https://doi.org/10.1007/s11069-007-9139-9

Gong, X.-L., Chen, K.-T., Chen, X.-Q., You, Y., Chen, J.-G., Zhao, W.-Y., Lang, J., 2020. Characteristics of a Debris Flow Disaster and Its Mitigation Countermeasures in Zechawa Gully, Jiuzhaigou Valley, China. Water 12, 25. https://doi.org/10.3390/w12051256

Gregoretti, C., 2008. Inception Sediment Transport Relationships at High Slopes. J. Hydraul. Eng. 134, 1620–1629. https://doi.org/10.1061/(ASCE)0733-9429(2008)134:11(1620)

Gregoretti, C., Degetto, M., Bernard, M., Boreggio, M., 2018. The debris flow occurred at Ru Secco Creek, Venetian Dolomites, on 4 August 2015: Analysis of the phenomenon, its characteristics and reproduction by models. Frontiers in Earth Science 6, 80. https://doi.org/10.3389/feart.2018.00080

Gregoretti, C., Stancanelli, L.M., Bernard, M., Boreggio, M., Degetto, M., Lanzoni, S., 2019. Relevance of erosion processes when modelling in channel gravel debris flows for efficient hazard assessment. Journal of Hydrology 568, 575–591. https://doi.org/10.1016/j.jhydrol.2018.10.001

Gylfadóttir, S.S., Mergili, M., Jóhannesson, T., Helgason, J.K., Sæmundsson, Þ., Fischer, J.-T., Pudasaini, S.P., 2019. A three-phase mass flow model applied for the simulation of complex landslide–glacier–lake interactions in Iceland., in: Geophysical Research Abstracts.

Hartmann, S., Pedoth, L., Dalla Torre, C., Schneiderbauer, S., 2021. Beyond the Expected-Residual Risk and Cases of Overload in the Context of Managing Alpine Natural Hazards. International Journal of Disaster Risk Science 12, 205–219. https://doi.org/10.1007/s13753-020-00325-3

Hübl, J., Strauss, A., Holub, M., Suda, J., 2005. Structural mitigation measures, in: 3rd Probabilistic Workshop: Technical Systems + Natural Hazards. Wien, pp. 115–126.

Huebl, J., Fiebiger, G., 2005. Debris-fow mitigation measures, in: Debris-Flow Hazards and Related Phenomena. Springer, Berlin, Heidelberg, pp. 445–487.

Hungr, O., Leroueil, S., Picarelli, L., 2014. The Varnes classification of landslide types, an update. Landslides 11, 167–194. https://doi.org/10.1007/s10346-013-0436-y

Hungr, O., McDougall, S., Bovis, M., 2005. Entrainment of material by debris flows, in: Debris-Flow Hazards and Related Phenomena. Springer, Berlin, Heidelberg, pp. 135–158. https://doi.org/10.1007/3-540-27129-5_7

Hungr, O., Morgan, G.C., Kellerhals, R., 1984. Quantitative analysis of debris torrent hazards for design of remedial measures. Canadian Geotechnical Journal 21, 663–677. https://doi.org/10.1139/t84-073

Jakob, M., Hungr, O., Jakob, D., 2005. Debris-flow hazards and related phenomena, Springer.

Johnson, P.A., McCuen, R.H., 1989. Slit dam design for debris flow mitigation. Journal of Hydraulic Engineering 115, 1293–1296. https://doi.org/10.1061/(ASCE)0733-9429(1989)115:9(1293)

Kean, J.W., McCoy, S.W., Tucker, G.E., Staley, D.M., Coe, J.A., 2013. Runoff-generated debris flows: Observations and modeling of surge initiation, magnitude, and frequency. Journal of Geophysical Research: Earth Surface 118, 2190–2207. https://doi.org/10.1002/jgrf.20148

Kean, J.W., Staley, D.M., Leeper, R.J., Schmidt, K.M., Gartner, J.E., 2012. A low-cost method to measure the timing of postfire flash floods and debris flows relative to rainfall. Water Resources Research 48. https://doi.org/10.1029/2011WR011460

Lamb, M.P., Dietrich, W.E., Venditti, J.G., 2008. Is the critical Shields stress for incipient sediment motion dependent on channel-bed slope? J. Geophys. Res. Earth Surf. 113, 2008. https://doi.org/10.1029/2007JF000831

Lanzoni, S., Gregoretti, C., Stancanelli, L.M., 2017. Coarse-grained debris flow dynamics on erodible beds. J. Geophys. Res. Earth Surf. 122, 592–614. https://doi.org/10.1002/2016JF004046

Larsen, M.C., Wieczorek, G.F., Eaton, L.S., Torres-Sierra, H., 2001. Natural Hazards on Aluvial Fans: The Debris Flow and Flash flood disaster of December 1999, Vargas State, Venezuela, in: Sylva, W. (Ed.), Proceedings of the Sixth Caribbean Islands Water Resources Congress. Mayagüez, Puerto Rico, pp. 1–7.

Liu, J., Nakatani, K., Mizuyama, T., 2012. Effect assessment of debris flow mitigation works based on numerical simulation by using Kanako 2D. Landslides 2012 102 10, 161–173. https://doi.org/10.1007/S10346-012-0316-X

Lo, D.O.K., 2000. Review of natural terrain landslide debris-resisting barrier design.

Marchelli, M., De Biagi, V., 2019. Dynamic effects induced by the impact of debris flows on protection barriers. International Journal of Protective Structures 10, 116–131. https://doi.org/10.1177/2041419618798378

Marchi, L., Cavalli, M., 2007. Procedures for the documentation of historical debris flows: Application to the Chieppena Torrent (Italian Alps). Environmental Management 40, 493–503. https://doi.org/10.1007/s00267-006-0288-5

Marchi, L., D'Agostino, V., 2004. Estimation of debris-flow magnitude in the Eastern Italian Alps. Earth Surface Processes and Landforms 29, 207–220. https://doi.org/10.1002/esp.1027

Mazzorana, B., Hübl, J., Fuchs, S., 2009. Improving risk assessment by defining consistent and reliable system scenarios. Natural Hazards and Earth System Science 9, 145–159. https://doi.org/10.5194/nhess-9-145-2009

Mazzorana, B., Trenkwalder-Platzer, H.J., Fuchs, S., Hübl, J., 2014. The susceptibility of consolidation check dams as a key factor for maintenance planning. Österreichische Wasser und Abfallwirtschaft 66, 214–216. https://doi.org/10.1007/s00506-014-0160-4

McCoy, S.W., Kean, J.W., Coe, J.A., Tucker, G.E., Staley, D.M., Wasklewicz, T.A., 2012. Sediment entrainment by debris flows: In situ measurements from the headwaters of a steep catchment. J. Geophys. Res. Earth Surf. 117, n/a-n/a. https://doi.org/10.1029/2011JF002278

McDougall, S., Hungr, O., 2004. A model for the analysis of rapid landslide motion across three-dimensional terrain. Canadian Geotechnical Journal 41, 1084–1097. https://doi.org/10.1139/t04-052

Mergili, M., Fischer, J.T., Krenn, J., Pudasaini, S.P., 2017. R.avaflow v1, an advanced open-source computational framework for the propagation and interaction of two-phase mass flows. Geoscientific Model Development 10, 553–569. https://doi.org/10.5194/gmd-10-553-2017

Mergili, M., Frank, B., Fischer, J.T., Huggel, C., Pudasaini, S.P., 2018. Computational experiments on the 1962 and 1970 landslide events at Huascarán (Peru) with r.avaflow: Lessons learned for predictive mass flow simulations. Geomorphology 322, 15–28. https://doi.org/10.1016/j.geomorph.2018.08.032

Mergili, M., Mergili, M., Jaboyedoff, M., Pullarello, J., Pudasaini, S.P., 2020a. Back calculation of the 2017 Piz Cengalo-Bondo landslide cascade with r.avaflow: What we can do and what we can learn. Natural Hazards and Earth System Sciences 20, 505–520. https://doi.org/10.5194/nhess-20-505-2020

Mergili, M., Pudasaini, S.P., 2021. r.avaflow - The mass flow simulation tool. r.avaflow 2.3 Software. URL https://www.avaflow.org (accessed 4.12.21).

Mergili, M., Pudasaini, S.P., Emmer, A., Fischer, J.T., Cochachin, A., Frey, H., 2020b. Reconstruction of the 1941 GLOF process chain at Lake Palcacocha (Cordillera Blanca, Peru). Hydrology and Earth System Sciences 24, 93–114. https://doi.org/10.5194/hess-24-93-2020

Mizuyama, T., 2008. Structural countermeasures for debris flow disasters. International Journal of Erosion Control Engineering 1, 38–43. https://doi.org/10.13101/ijece.1.38

Mizuyama, T., Kobashi, S., Ou, G., 1992. Prediction of debris flow peak discharge, in: Interpraevent. Bern, Switzerland, pp. 99–108.

O'Brien, J.S., Julien, P.Y., Fullerton, W.T., 1993. Two-dimensional water flood and mudflow simulation. Journal of Hydraulic Engineering 119, 244–261. https://doi.org/10.1061/(asce)0733-9429(1993)119:2(244)

Osti, R., Egashira, S., 2008. Method to improve the mitigative effectiveness of a series of check dams against debris flows. Hydrological Processes 22, 4986–4996. https://doi.org/10.1002/hyp.7118

Papa, M., Egashira, S., Itoh, T., 2004. Critical conditions of bed sediment entrainment due to debris flow. Natural Hazards and Earth System Science 4, 469–474. https://doi.org/10.5194/nhess-4-469-2004

Piton, G., Carladous, S., Recking, A., Tacnet, J.M., Liébault, F., Kuss, D., Quefféléan, Y., Marco, O., 2016. Why do we build check dams in Alpine streams? An historical perspective from the French experience. Earth Surface Processes and Landforms 42, 91–108. https://doi.org/10.1002/esp.3967

Piton, G., Recking, A., 2014. The dynamic of streams equipped with Check Dams, in: River Flow 2014. CRC Press, pp. 1437–1445. https://doi.org/10.1201/b17133-192

Prein, A.F., Rasmussen, R.M., Ikeda, K., Liu, C., Clark, M.P., Holland, G.J., 2016. The future intensification of hourly precipitation extremes. Nature Climate Change 7, 48–52. https://doi.org/10.1038/nclimate3168

Prochaska, A.B., Santi, P.M., Higgins, J.D., Cannon, S.H., 2008. A study of methods to estimate debris flow velocity. Landslides 5, 431–444. https://doi.org/10.1007/s10346-008-0137-0

Pudasaini, S.P., Mergili, M., 2019. A multi-phase mass flow model. Journal of Geophysical Research: Earth Surface 124, 1–23. https://doi.org/10.1029/2019jf005204

Remaître, A., W. J. Van Asch, T., Malet, J.P., Maquaire, O., 2008. Influence of check dams on debris-flow run-out intensity. Natural Hazards and Earth System Science 8, 1403–1416. https://doi.org/10.5194/nhess-8-1403-2008

Rickenmann, D., 1999. Empirical relationships for debris flow. Natural Hazards 19, 47–77.

Rickenmann, D., Weber, D., Stepanov, B., 2003. Erosion by debris flows in field and laboratory experiments. International Conference on Debris-Flow Hazards Mitigation: Mechanics, Prediction, and Assessment, Proceedings 2, 883–894.

Rickenmann, D., Zimmermann, M., 1993. The 1987 debris flows in Switzerland: documentation and analysis. Geomorphology 8, 175–189. https://doi.org/10.1016/0169-555X(93)90036-2

Rodríguez-Morata, C., Villacorta, S., Stoffel, M., Ballesteros-Cánovas, J.A., 2019. Assessing strategies to mitigate debris-flow risk in Abancay province, south-central Peruvian Andes. Geomorphology 342, 127–139. https://doi.org/10.1016/j.geomorph.2019.06.012

Rosatti, G., Begnudelli, L., 2013. Two-dimensional simulation of debris flows over mobile bed: Enhancing the TRENT2D model by using a well-balanced Generalized Roe-type solver. Computers and Fluids 71, 179–195. https://doi.org/10.1016/j.compfluid.2012.10.006

Scheidl, C., Rickenmann, D., McArdell, B.W., 2013. Runout Prediction of Debris Flows and Similar Mass Movements, in: Landslide Science and Practice. Springer Berlin Heidelberg, pp. 221–229. https://doi.org/10.1007/978-3-642-31310-3_30

Simoni, A., Bernard, M., Berti, M., Boreggio, M., Lanzoni, S., Stancanelli, L.M., Gregoretti, C., 2020. Runoff-generated debris flows: Observation of initiation conditions and erosion–deposition dynamics along the channel at Cancia (eastern Italian Alps). Earth Surface Processes and Landforms 45, 3556–3571. https://doi.org/10.1002/esp.4981

Sodnik, J., Kryžanowski, A., Martin, M., Mikoš, M., 2013. Torrential Check Dams as Debris-Flow Sources, in: Landslide and Flood Hazard Assessment. Zagreb, pp. 6–9.

Stecher, M., Mazzorana, B., Hübl, J., 2012. Proposal of risk mitigation strategies based on a conceptual planning approach. A case study conducted in the Gadriabach study site, Vinschgau valley, Italy, in: Interpraevent. Grenoble, pp. 811–820.

Stoffel, M., Tiranti, D., Huggel, C., 2014. Climate change impacts on mass movements - Case studies from the European Alps. Science of the Total Environment 493, 1255–1266. https://doi.org/10.1016/j.scitotenv.2014.02.102

Tacnet, J.-M., Curt, C., Benjamin, R., Richard, D., 2012. Efficiency Assessment for Torrent Protection Works, in: Interpraevent. Grenoble, pp. 821–831.

Takahashi, T., 2007. Debris Flow: Mechanics, Prediction and Countermeasures. Taylor & Francis.

Tseng, W.H., Wang, H.W., Chou, S.C., Kao, Y.L., Shieh, C.L., 2012. Experiments on channel evolution caused by check-dam failure. Journal of Mountain Science 9, 175–184. https://doi.org/10.1007/s11629-012-2252-6

Vagnon, F., 2020. Design of active debris flow mitigation measures: a comprehensive analysis of existing impact models. Landslides 17, 313–333. https://doi.org/10.1007/s10346-019-01278-5

Victoriano, A., Brasington, J., Guinau, M., Furdada, G., Cabré, M., Moysset, M., 2018. Geomorphic impact and assessment of flexible barriers using multi-temporal LiDAR data: The Portainé mountain catchment (Pyrenees). Engineering Geology 237, 168–180. https://doi.org/10.1016/j.enggeo.2018.02.016

Wang, G.L., 2013. Lessons learned from protective measures associated with the 2010 Zhouqu debris flow disaster in China. Natural Hazards 69, 1835–1847. https://doi.org/10.1007/s11069-013-0772-1

Zeng, Q.L., Yue, Z.Q., Yang, Z.F., Zhang, X.J., 2009. A case study of long-term field performance of check-dams in mitigation of soil erosion in Jiangjia stream, China. Environmental Geology 58, 897–911. https://doi.org/10.1007/s00254-008-1570-z

Zhang, F., Yan, B., Feng, X., Lan, H., Kang, C., Lin, X., Zhu, X., Ma, W., 2019. A rapid loess mudflow triggered by the check dam failure in a bulldoze mountain area, Lanzhou, China. Landslides 16, 1981–1992. https://doi.org/10.1007/s10346-019-01219-2

4 Multiscale analysis of surface roughness for the improvement of natural hazard modelling

Natalie Brožová[1,2,4,#], Tommaso Baggio[3,#], Vincenzo D'Agostino[3], Yves Bühler[1,4], and Peter Bebi[1,4]

[#] ***These authors contributed equally to this work***

[1] *Alpine Environment and Natural Hazards, WSL Institute for Snow and Avalanche Research SLF, Davos Dorf, Switzerland*

[1] *Department of Environmental Systems Science, Swiss Federal Institute of Technology (ETH Zurich), Zurich, Switzerland*

[1] *Department of Land, Environment, Agriculture and Forestry, University of Padua, Legnaro, Italy*

[1] *Climate Change, Extremes and Natural Hazards in Alpine Regions Research Center CERC, Davos Dorf, Switzerland*

This chapter has been published in *Natural Hazards and Earth System Sciences* in 2021

4.1 Abstract

Surface roughness influences the release of avalanches and the dynamics of rockfall, avalanches and debris flow, but it is often not objectively implemented in natural hazard modelling. For two study areas, a treeline ecotone and a windthrow-disturbed forest landscape of the European Alps, we tested seven roughness algorithms using a photogrammetric digital surface model (DSM) with different resolutions (0.1, 0.5 and 1 m) and different moving-window areas (9, 25 and 49 m^2). The *vector ruggedness measure* roughness algorithm performed best overall in distinguishing between roughness categories relevant for natural hazard modelling (including shrub forest, high forest, windthrow, snow and rocky land cover). The results with 1 m resolution were found to be suitable to distinguish between the roughness categories of interest, and the performance did not increase with higher resolution. In order to improve the roughness calculation along the hazard flow direction, we tested a directional roughness approach that improved the reliability of the surface roughness computation in channelised paths. We simulated avalanches on different elevation models (lidar-based) to observe a potential influence of a DSM and a digital terrain model (DTM) using the simulation tool Rapid Mass Movement Simulation (RAMMS). In this way, we accounted for the surface roughness based on a DSM instead of a DTM, which resulted in shorter simulated avalanche runouts by 16 %–27 % in the two study areas. Surface roughness above a treeline, which in comparison to the forest is not represented within the RAMMS, is therefore underestimated. We conclude that using DSM-based surface roughness in combination with DTM-based surface roughness and considering the directional roughness is promising for achieving better assessment of terrain in an alpine landscape, which might improve the natural hazard modelling.

4.2 Introduction

Surface roughness is a topographic parameter commonly used to identify and characterise surface features, such as different vegetation types (Stambaugh and Guyette, 2008) and geomorphological characteristics (Cavalli et al., 2008; McKean and Roering, 2004; Nguyen and Fenton, 2005). Quantifying surface roughness is thus central for the estimation of various biophysical characteristics and ecosystem services (Koponen et al., 2004; Wu et al., 2018). With the increasing availability of high-resolution remote sensing data, it is increasingly possible to quantify surface roughness over larger areas and to estimate how related ecosystem services and climate feedbacks change over time (Mina et al., 2017; Myers-Smith et al., 2015; Nel et al., 2014; Palomo, 2017). Surface roughness has effects on one of the most relevant ecosystem services in mountain regions: gravity-driven natural hazards. In particular, the occurrence and runout distance of rockfall, debris flows and snow avalanches are influenced by terrain roughness and land cover (Baroni et al., 2007; May, 2002; Michelini et al., 2017; Teich et al., 2014). In the following sections, we describe the most frequent gravity-driven natural hazards affecting the European Alps, highlighting why it is important to consider surface roughness and land cover when modelling and predicting such phenomena.

Debris flows can be defined as gravity-driven flows consisting of interacting phases, mainly a debris and a fluid phase (Jakob et al., 2005; Pudasaini, 2012; Takahashi, 2000). Approaches to modelling flow propagation are numerous (Frank et al., 2017; Pudasaini and Mergili, 2019). They can represent the flow as a single phase or multiple phases consisting of solid and water components propagating through a given topography (Christen et al., 2010; Rosatti and Begnudelli, 2013). Some of them include a spatial variability of the friction parameters and can even simulate erosion processes (Hungr and McDougall, 2009; Mergili et al., 2017). However, a relatively small number of them consider the presence or absence of forest and the surface roughness (May, 2002). Ishikawa et al. (2000) emphasise the importance of the land cover (especially forests) as an active prevention measure for stabilising slopes and reducing the debris flow runout distance. Tree and shrub parameters are known to influence the velocity and runout distance in different parts of a debris flow fan (Ishikawa et al., 2000; Michelini, 2016). On the other hand, intrinsic physical characteristics and the solid volume concentration of the routing flow are important parameters in determining the interaction between debris flows and surface roughness. In particular, debris flows with a high concentration of the solid component exhibit a strong interaction with forest structure (Michelini et al., 2017). A spatially distributed surface roughness map can increase the reliability of debris flow simulations. This aspect is of particular importance in extreme scenarios where the mass flow can spread outside the main channel path, propagating on other surface types.

Rockfall processes are influenced by topographic parameters (slope and terrain curvature), surface roughness and land cover (Pfeiffer and Bowen, 1989; Wang and Lee, 2010). Surface roughness and land cover influence the contact angle between the rock and the surface, changing the velocity by rolling and sliding (Wang and Lee, 2010) and influencing the runout distance (Caviezel et al., 2019; Dorren et al., 2005; Lopez-Saez et al., 2016). Vegetation decreases the energy of moving rocks and eventually stops them

(Jonsson, 2007). Tree density and size are fundamental characteristics for assessing the protection function of the forest (Dorren et al., 2015).

Surface roughness is an important parameter in relation to snow distribution (Lehning et al., 2011), and it is particularly crucial in preventing weak layers and avalanche formation and release (Schweizer et al., 2003; Viglietti et al., 2010). The supporting force of tree stems and the heterogeneity of the forest snowpack, influenced by crown interception, reduce the release of slab avalanches (Bebi et al., 2009; McClung and Schaerer, 2006; Schneebeli and Bebi, 2004; Teich et al., 2012b). The anchoring effect of the vegetation in snow gliding has been demonstrated in several studies, and the density, height and heterogeneity of vegetation cover are crucial characteristics (Endo, 1983; Feistl et al., 2014; Höller, 2001, 2013). Furthermore, surface roughness has a critical impact on the flow path and runout distance of avalanches (Bühler et al., 2011).

Terrain roughness is increasingly considered an important factor when evaluating vegetation effects on natural hazards and also more generally in large-scale hazard mapping. Moreover, vegetation effects on snow avalanches, rockfall and debris flows are often strongly dependent on the type of vegetation and on potential changes in vegetation over time (Bigot et al., 2009; May, 2002). Digital surface models (DSMs) capture surface characteristics and, depending on the frequency of acquisition, detect land cover changes over time. Distinguishing among different vegetation types and assessing their effects on natural hazards is particularly important for spatially and temporally changing vegetation patterns in mountainous terrain. While the consideration of dense forest cover in natural hazard models is already advanced (Bühler et al., 2018; Feistl et al., 2015), this is clearly not the case for shrub forests, very open forest structures and early successional stages of forest cover, which occur predominantly near treeline or after natural or anthropogenic disturbances (windthrows, bark beetle outbreaks, wildfires and logging operations). Furthermore, treeline ecotones are generally shifting upwards, and natural disturbances are expected to increase in the future, both due to global changes (Harsch et al., 2009; Seidl et al., 2017). Such regions are typical release and transition areas for gravitational hazards like snow avalanches, rockfall, landslides and debris flows. Widespread changes in landscape lead to shifts in vegetation composition (Tasser and Tappeiner, 2002), thus influencing surface roughness. It is necessary to understand which natural hazard processes can be expected with further changes and to map where these natural hazards may occur, as the frequency, intensity and extent of natural hazards may increase with decreasing surface roughness.

Groups of trees and shrubs in treeline ecotones are not usually characterised as forest, even if they influence the release and dynamics of natural hazards (Elliott, 2017). It would thus be useful to improve the characterisation of surface roughness calculated outside and inside mapped forest vegetation and to include lower vegetation, shrub forests and dead wood, which are not classified as forest. Natural disturbances, such as windthrow and bark beetle outbreaks, alter the forest structure and thus change the forest protective function. Such natural disturbances are expected to become more frequent and severe under climate change (Bebi et al., 2017; Seidl et al., 2017), and forest protective functions may be reduced. The protective

functions against snow avalanches, rockfall and debris flows are particularly at risk when a large-scale disturbance occurs and affects forests at the stand level. Windthrow creates a high degree of surface roughness from downed trees, root plates and stumps. In the case of snow avalanches, surface roughness modifies snowpack properties and offers direct support (Schneebeli and Bebi, 2004), which, similarly to forest, may have the ability to hinder the formation of continuous weak layers (Schweizer et al., 2003). Leaving dead wood in place in protection forests after a windthrow event or bark beetle outbreak may thus offer sufficient protection capacity against snow avalanches until the post disturbance vegetation can take over this function (Wohlgemuth et al., 2017). Likewise, increased surface roughness from dead wood may considerably decrease the runout distance of rockfall processes (Fuhr et al., 2015; Bourrier et al., 2012; Ringenbach et al., 2021).

There are many algorithms quantifying surface roughness, indicating the variability of a certain topographic variable (slope, elevation, aspect, curvature and vector dispersion) within a certain area defined by a certain number of neighbouring cells (moving window) (Evans, 1984; Haneberg et al., 2005; Hobson, 1967; Philip and Watson, 1986; Sappington et al., 2007; Smith, 2014). In this study we consider roughness algorithms requiring a digital elevation model (DEM) as input. Surface roughness maps based on the analysis of a DEM are influenced by its resolution (Shepard et al., 2001) and moving-window size (Grohmann et al., 2011). Higher DEM resolutions (<1 m) allow us to see more detailed terrain, but they are usually only available for smaller areas. DEM-based surface roughness algorithms calculate the roughness value by analysing a certain number of neighbourhood cells. In such a sense, most of the roughness indices reported in literature considered the DEM as an isotropic surface. However, the concept of surface anisotropy is of fundamental importance for the investigation of geomorphological features and channelised or dispersed flows (Busse and Jelly, 2020; Insua-Arévalo et al., 2021; Middleton et al., 2020). If the surface shows an anisotropic texture, the flow resistance is directly influenced by obstacles disposed along the flow direction. Since the investigated natural hazards show a predominant diffusion direction identified as the combination of terrain slope and curvature, texture anisotropy has to be taken into account when simulating mass flows (Roy et al., 2016; Viero and Valipour, 2017). Some attempts to calculate the roughness along a given direction have been made, but they have not yet been applied to large-scale hazard mapping (Michelini, 2016; Trevisani and Cavalli, 2016). However, the investigated natural hazards have a predominant diffusion direction identified as the combination of terrain slope and curvature. Some studies implemented the surface roughness along a predefined direction (Michelini, 2016; Trevisani and Rocca, 2015). The direction for which roughness has been computed, usually derived through a GIS algorithm (D8 or D-infinity), is applied to the original or smoothed digital models. However, the direction derived through neighbourhood cell analysis could not be the same as that of the mass flow propagation. Such behaviours may be observed when the routing volumes are extreme, and therefore in some particular situations the propagation direction may be defined by its inertia rather than the topography (Guo et al., 2020). In other cases, the particular mountain topography may force mass flows to affect the opposite hillside of the valley through a runup mechanism (Iverson et al., 2016). Furthermore, the flow direction of banks and channel side features

computed with GIS algorithms do not usually correspond to the mass flow direction. In this situation bank direction can be improved through a smoothing process of the DTM in order to remove gullies and channels from the basal topography. This technique can be easily applicable in the case of regular channels, but it could become more complex when the channel morphology is irregular, since it could oversimplify the basal topography. For such reasons in this study, we propose a novel approach to calculate surface roughness along user-defined lines.

In this study we compare the efficiency of seven widely used algorithms applied to high-resolution remote sensing data in distinguishing among different surface roughness categories in two study areas. We specifically addressed the following research questions. (a) How well can different surface roughness categories be distinguished with the selected algorithms? (b) What is the influence of the DSM resolution and moving-window area on the roughness classification? (c) Is it possible to improve the roughness calculation by introducing a directional roughness along the predominant mass flow direction? (d) How much can a mass flow simulation improve if roughness is properly taken into account?

4.3 Methods

We identified and tested seven algorithms calculating surface roughness in order to understand which algorithm is the most suitable for terrain feature classification. The algorithms were chosen based on a literature review. Only those algorithms that are recognised for their ability to provide an accurate estimation of vegetation cover were selected. We tested these algorithms on two study areas to evaluate their performance in identifying the ground features of interest: biomass on the ground (disturbed forest), rocky surface, short vegetation and forest. We selected algorithms that use a DEM, and we used the digital surface model (DSM), as it represents all the ground features of interest.

We selected two study areas, where a high-resolution DSM (0.1 m), derived by photogrammetry, and high-resolution (0.5 m) lidar data were available and where relevant terrain features of disturbed mountain forest landscapes and treeline ecosystems were represented. To evaluate the effects of different cell resolutions, we tested three DSM resolutions, equal to 0.1, 0.5 and 1 m, resampling the 0.1 m photogrammetric DSM to 0.5 and 1 m (method: mean value). In previous studies the scale of the roughness calculation has been represented as a moving window identified by the number of cells (Grohmann and Riccomini, 2009; Michelini et al., 2017), which can result in different analysed areas (a moving window of 3×3 m with a resolution of 1 m results in an area of 9 m^2, but with a resolution of 2 m the area is 36 m^2). We therefore compared the roughness algorithms (Table 4.1) using different moving-window areas instead of different moving windows (number of cells used). With this moving-window area approach, the number of cells differs according to the DSM resolution, but the analysed area remains the same. The effect of scale was analysed using the smallest moving-window areas in order to preserve the detailed terrain from the high-resolution DSMs. The moving window for different resolutions was approximated to the greater odd number. Using seven different algorithms to calculate roughness with three resolutions (0.1, 0.5 and 1 m) and three moving-window areas (3×3 m, 5×5 m and 7×7 m) resulted in a total of 63 combinations. We

statistically tested (Sect. 2.3) how well these algorithms, in different combinations of spatial resolution and moving-window area, can distinguish between the seven roughness categories presented in Table 4.2.

Table 4.1: Summary of the seven algorithms used to compute the terrain roughness.

Surface roughness algorithm	Abbreviation	Reference
Area ratio	AR	Hobson (1967)
Vector ruggedness measure	VRM	Sappington et al. (2007)
Standard deviation of the profile curvature	SD_PC	Grohmann et al. (2011)
Standard deviation of the residual topography	SD_RT	Grohmann et al. (2011)
Standard deviation of the slope	SD_S	Grohmann et al. (2011)
Terrain ruggedness index	TRI	Riley et al. (1999)
Vector dispersion	VD	Grohmann et al. (2011)

After choosing the best performing algorithm to distinguish between the categories, we tested the difference between using a DSM and a DTM as an input for calculating the surface roughness. We also simulated an avalanche on both the DSM and DTM to observe the influence of the surface roughness on the avalanche runout distance. The surface roughness and its impact on the runout distance of an avalanche are demonstrated when using a DSM, whereas the surface roughness is filtered out when a DTM is used.

Table 4.2: Roughness categories using orthophotos and the vegetation height model (VHM) were selected to evaluate the different surface roughness algorithms.

Roughness category	Braema	Franza
Snow	x	
Very smooth	x	x
Smooth	x	x
Shrub forest	x	
High forest	x	x
Rocky	x	
Windthrow		x

4.3.1 Study areas

The two selected study areas, Braema and Franza, are located in the central and eastern European Alps (Figure 4.1a). Braema (Figure 4.1b) is an example of a treeline ecotone with treeline expansion. Franza (Figure 4.1c) was impacted by the 2018 storm Vaia and is an example of fully wind-thrown forest.

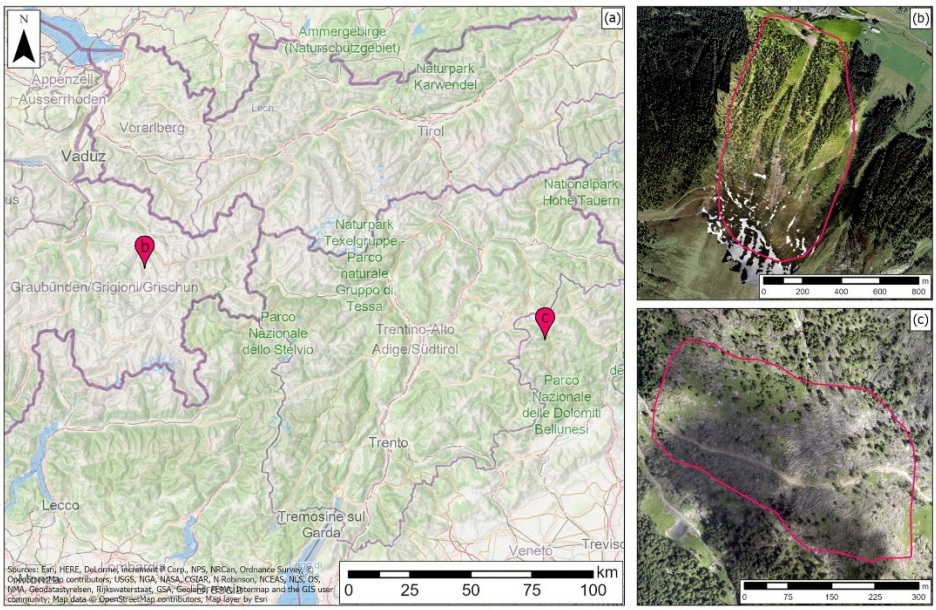

Figure 4.1: (a) Locations of the study areas in the central and eastern European Alps (map source: © OpenStreetMap contributors 2021; distributed under the Open Data Commons Open Database License (ODbL) v1.0.). (b) Braema, located close to Davos (Grisons, Switzerland; orthophoto in the background (© swisstopo, 2021) and orthophoto in the front from the drone flight 2019), and (c) Franza, located in the Dolomites (Veneto, Italy; orthophoto from the drone flight 2019).

4.3.1.1 Braema

The Braema study area is located in south-east Switzerland near Davos (canton Grisons). The elevation varies between 1550 and 2300 m a.s.l., and the aspect is mostly north-eastern. The upper part ranges in slope from 30 to 45∘ and is covered mainly by meadow and rocky terrain. The area is steeper between 2000 and 2200 m a.s.l. (40–45∘), where it is defined by open terrain and sparse vegetation. The study area also includes four valley channels. They are wider and less delineated at higher elevations but become narrower with decreasing elevation. At the lower elevations the banks of these gullies are stabilised by shrub forest dominated by green alder (Alnus viridis). Timber forest occurs below 1900 m a.s.l. on a moderately steep (less than 30∘) to very steep slope (up to 45∘). The dominant tree species is Norway spruce (Picea abies) with admixed European larch (Larix decidua) at high elevations (around 1800–2000 m a.s.l.). Avalanche barriers are present in the upper part of Braema, which served as a reference element for surface roughness in this study (Sect. 3.1).

The area of almost 1 km2 was surveyed on 17 June 2019 using a senseFly eBee+ drone (Lausanne, Switzerland) equipped with an RTK GNSS system for accurate georeferencing (better than 5 cm). The 404 photos were acquired with a SODA camera (focal length 10.6 mm, pixel size 2.4 µm) at a mean flight height of 148 m above ground and an overlap of 60 % (across track) and 70 % (along track), resulting in an average ground sampling distance (GSD) of 3 cm. This imagery was successively processed with the software Metashape (Agisoft LLC, Saint Petersburg, Russia), resulting in a point cloud with an average density of 263 points m−2. The point cloud was then processed into a DSM with a cell size of 0.1 m.

4.3.1.2 Franza

The Franza study area is located in the Dolomites, Italy, near the village of Livinallongo del Col di Lana (Veneto region). The elevation ranges between 1650 and 1950 m a.s.l., and the aspect is south-western. The area extends for 12 ha and includes the Ru de Andraz stream in the lower part. The area was strongly affected by the storm Vaia of 29 October 2018, which uprooted a large part of the forest stand. The fallen trees were left on the ground, and the area was not involved in forest management, except for the forest road, which was cleared of biomass. The remaining forest is just 5 %–10 % of the original forest cover. The central upper part of this area is covered by meadows and young open forests, which were not affected by the storm. The disturbed forest was dominated by Norway spruce (Picea abies) with admixed silver fir (Abies alba). European larch (Larix decidua) was the only tree species to survive the storm. The mean inclination of the area varies between 30 and 40∘.

The area was surveyed using a Phantom 4 drone (DJI, Shenzhen, China) with ground control points for image georeferencing. The drone flight took place on 26 October 2019, and the 971 images were successively processed in Metashape. The mean flight height was 45 m above ground, and the image overlap was greater than 70 %. The result was a DSM with a cell resolution of 0.05 m and a mean point density of 557 points m−2 (ground control point residual error in x, y and z: 3.7 cm), which was resampled to 0.1 m (mean value method) and cropped to 11 ha for this study.

4.3.2 Surface roughness algorithms

In order to describe the roughness, which consists of both geomorphological features and vegetation, we selected and tested seven algorithms using high-resolution DSMs. We selected widely used roughness algorithms already applied in the context of natural hazard modelling (Bühler et al., 2013; Crosta and Agliardi, 2004; Pfeiffer and Bowen, 1989; Veitinger and Sovilla, 2016; Wang and Lee, 2010). They are based on standard deviation and vector dispersion approaches calculated in a certain moving window. We then tested them with different spatial resolutions (0.1, 0.5 and 1 m) and moving-window areas (9, 25 and 49 m^2) on both study areas. The selected algorithms are summarised in Table 4.1.

4.3.2.1 Area ratio

The *area ratio* is the ratio between the real area and the flat area occupied by the square cell of the DSM (Hobson, 1967). The real area is computed using the slope algorithm implemented in GRASS GIS (Horn, 1981; Mitasova, 1985). The final map representing the area ratio is then smoothed using an average value within a moving window defined by the user. The area ratio is close to 1 for flat areas, while it extends up to an infinite value for extremely steep areas. In this study the algorithm was implemented as a shell script and run in the GRASS GIS environment (GRASS Development Team, 2021).

4.3.2.2 Vector ruggedness measure

For the vector ruggedness measure, the unit vector normal to the raster cell is decomposed in the relative x, y and z directions using the slope and the aspect of the cell through standard trigonometric functions (Durrant, 1996; Pincus, 1956). Its measure and computation are fully described in Sappington et

al. (2007). The resultant vector is calculated over a user-defined moving window. The strength of the vector is normalised for the total number of cells included in the moving window. In this study the algorithm was implemented as a raster module in GRASS GIS called r.vector.ruggedness.

4.3.2.3 Standard deviation of slope and profile curvature

The *standard deviation (SD) of the slope* represents the slope standard deviation within a defined moving window (Grohmann et al., 2011). The slope is derived from the DSM using the algorithm r.slope.aspect implemented in GRASS GIS derived from the formula proposed by Horn (1981). With the same approach, the *standard deviation of the profile curvature* (second derivative of the elevation) is computed within a moving window (Grohmann et al., 2011). Here, both algorithms were implemented in a shell script and run in GRASS GIS.

4.3.2.4 Standard deviation of residual topography

The SD of residual topography is computed as the SD of the difference between a smoothed DEM and the original one. The SD is calculated within a moving window defined by the user. This approach is widely used because it can be applied to different data types, such as point clouds (Vetter et al., 2011), satellite imagery (Gille et al., 2000; Schumann et al., 2007) and DEMs (Glenn et al., 2006; Cavalli and Marchi, 2008). In this study we calculated the smoothed DEM as the average value within a moving window 10×10 m independently from the input DEM resolution. The moving window used to compute the smoothed surface is automatically adjusted according to the model resolution. In this study this approach was implemented in a shell script and run in GRASS GIS.

4.3.2.5 Terrain ruggedness index

The *terrain ruggedness index* (*TRI*) is calculated as the mean change in elevation between a centre cell and its neighbours defined by the user (Riley et al., 1999). It represents the absolute variation between the centre cell and the surrounding cells. The index is similar to the average deviation of the centre absolute value, but it differs by the use of the centre cell. In the TRI, the centre cell is used as the reference instead of the average value of the cells within the defined moving window, thus emphasising the roughness. For this reason, TRI is more effective for highlighting the terrain features, especially in a small-scale analysis. In this study the algorithm called r.tri was implemented as a raster module in GRASS GIS, where it is possible to define the size of the moving window.

4.3.2.6 Vector dispersion

Vector dispersion is calculated as the orientation of a three-dimensional surface for the region of interest (Hobson, 1967). The different planes of the DSM are approximated by normal unit vectors, and the relative mean, dispersion and strength are calculated using the methods explained by Fisher (1953) and successively adapted by McKean and Roering (2004). This algorithm measures the degree of dispersion of the unit vectors in a given moving window. Here, the script was implemented as a raster GRASS GIS module called r.roughness.vector (Grohmann et al., 2011). To obtain the vector strength, the direction cosine maps are first calculated Eq. (1) and successively summed for a user-defined moving-window Eq. (2). The vector

strength (R) and vector dispersion (k) are derived with Eqs. (3) and (4), respectively, where N is the number of vectors. The vector dispersion has low values for regular smooth surfaces because the vectors are parallel and the vector strength becomes closer to the number of vectors. This algorithm is sensitive to small-scale variation in elevation and is therefore considered suitable for detecting vegetated areas.

$$x_i = sin\theta_i cos\phi_i y_i = sin\theta_i sin\phi_i z_i = cos\theta_i \quad (1)$$

$$\overline{x} = \sum_{i=1}^{N} x_i \, \overline{y} = \sum_{i=1}^{N} y_i \, \overline{z} = \sum_{i=1}^{N} z_i \quad (2)$$

$$R = \sqrt{\overline{x}^2 + \overline{y}^2 + \overline{z}^2} \quad (3)$$

$$k = (N-1)/(N-R) \quad (4)$$

4.3.3 Design and statistical analysis of roughness categories

Seven different roughness categories (Table 4.2) were chosen using orthophotos from the two study areas (Figure 4.2). In order to distinguish between the categories “very smooth” and “smooth” and between “shrub forest” and “high forest”, we used a vegetation height model (VHM), which we calculated as the difference between the digital surface model and digital terrain model (VHM = DSM − DTM; we used the lidar data described in Sect. 2.5 lidar-based roughness). The “snow” category was selected as the control, since in our case this surface is the smoothest and should therefore have the lowest roughness values. The very smooth category is dominated by features with heights up to 0.5 m, and the smooth category mainly includes features from 0.5 to 1 m height. Both of these categories are dominated by lower vegetation, which is not considered important for the interaction with natural hazards. Shrub forest is mainly composed of green alder and smaller trees between 3 and 5 m tall, while the high forest category has a minimum tree height of 10 m.

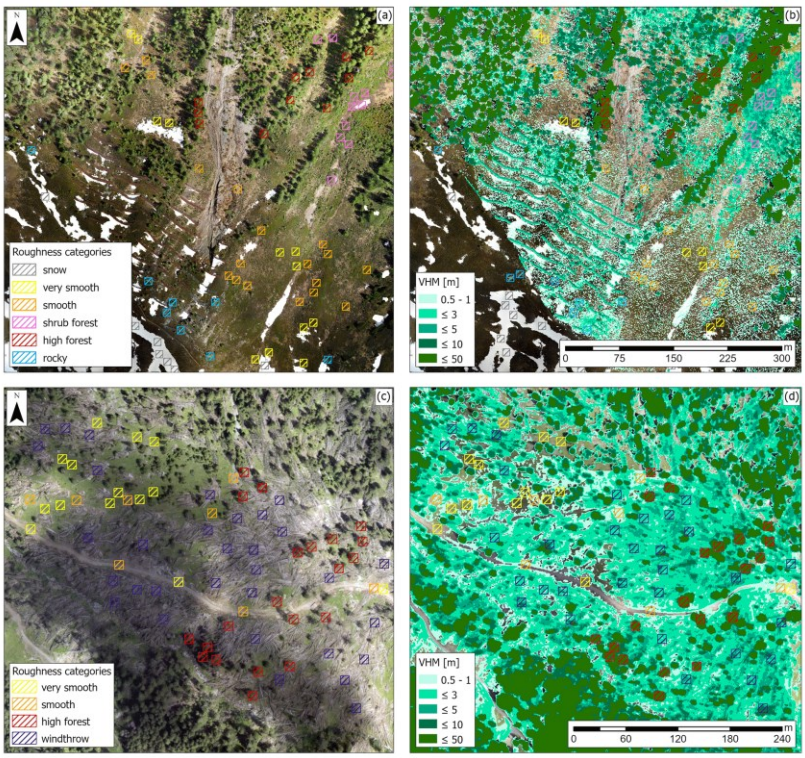

Figure 4.2: Roughness categories were selected based on the orthophoto alone (a) and (c) (drone flights, 2019) and with the vegetation height model (VHM, produced as the difference between the DSM and DTM provided by the Federal Office of Topography for Braema (© swisstopo, 2018) and Veneto region for Franza; b and d). The Braema study area (Grisons, Switzerland) is shown in (a) and (b), and the Franza study area (Veneto, Italy) is shown in (c) and (d).

Control areas of 10×10 m were manually selected using the orthophotos in order to extract the calculated roughness values and compare these values for different categories. The number of values extracted per category depended on the spatial resolution. A higher spatial resolution (0.1 m) results in 10 000 values per feature, a medium resolution (0.5 m) results in 400 values per feature and a lower resolution (1 m) results in 100 values per feature. We randomly sampled all the values to obtain 1000 values per roughness category for analysis. We statistically analysed (paired Wilcoxon test) the algorithms to determine the overlapping distribution of pairs of roughness categories. The tested algorithm in the corresponding resolution and moving window was able to distinguish between the roughness categories in cases where there was a significant difference (p value < 0.05) between the categories. In order to obtain a classification based on threshold values for a technical purpose, we analysed the kernel density distribution between the roughness categories (Table 4.2), after evaluating the best-performing algorithm, to determine the point of minimum overlap. We used the overlap function (overlapping package; Pastore, 2018; Pastore and Calcagnì, 2019) implemented in R (R Core Team, 2021). This intersection is the threshold between two roughness categories.

4.3.4 Directional roughness

Since mass flows have a propagation direction, one of our aims was to improve the roughness calculation along the expected direction of diffusion. For this purpose, we modified the SD of residual topography algorithm to test the roughness improvement along open slopes, valleys and gullies. The directional

roughness is computed as the SD of the residual topography where only a subset of the neighbourhood cells are analysed for 16 directions. The roughness direction is identified using a manually designed polyline. In accordance with the direction given by the polylines, the algorithm computes the SD of six or four cells, without considering the central cell value of the moving window (the resolution used was 1 m, and the cell moving-window area was 9 m^2). We calculated the directional roughness for the Braema study area only. In order to better understand the effects of the directional roughness, we manually identified four transects (Figure 4.3) and compared the directional and non-directional roughness.

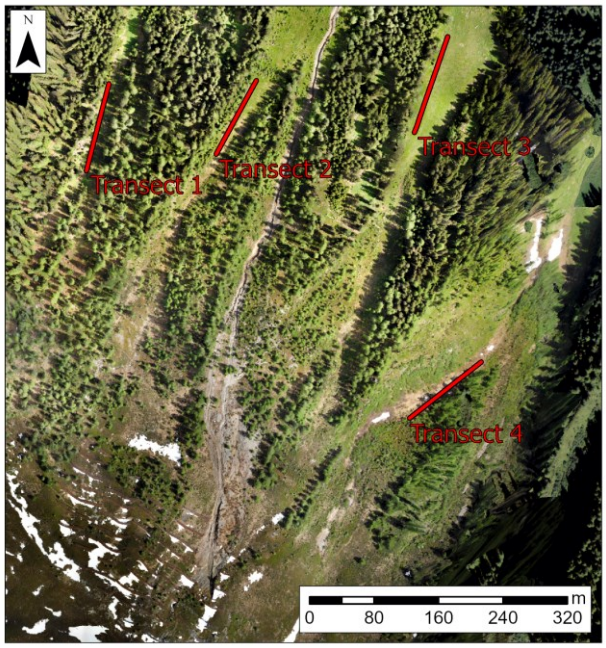

Figure 4.3: Four transects within gullies in the Braema study area (Grisons, Switzerland; orthophoto from the drone flight, 2019). The surface roughness was analysed using non-directional and directional SD of residual topography.

4.3.5 Lidar-based roughness

For the best performing algorithm, we compared the terrain roughness from the DSM and a lidar-based DTM. Lidar data were acquired in July 2019 (>35 points m−2) for Franza and in August 2015 for Braema (>18 points m−2). Regarding the Franza study area, the DSM and DTM were already produced for the Veneto region as a raster layer at the final resolution of 0.5 m. The lidar survey of the Braema area was acquired with an LMS-Q 780 and was part of a larger surveying campaign and was provided by the Federal Office of Topography. The final DEM products were resampled to a resolution of 0.5 m.

Based on the results of the roughness algorithm evaluation, we calculated the terrain roughness for the DTM and the DSM using the vector ruggedness measure algorithm (moving-window area of 49 m^2 and cell size of 0.5 m). We then plotted the results to highlight the differences in terrain roughness.

4.3.6 Case study: snow avalanche modelling

To investigate the importance of terrain roughness on the numerical simulation results, we implemented a snow avalanche simulation. We performed a total of four simulations using two types of terrain morphology

(the lidar-derived DTM and the DSM) for both of the study areas. The simulation tool that we applied is the snow avalanche module of RAM (Christen et al., 2010), version 1.7.20. We identified one release area for each study area based on topographic and vegetation analysis (terrain slope, curvature and land cover). The release depth was homogeneous and we set it to 1 m, accounting for a total volume of 1457.9 m^3 (Braema) and 284.8 m^3(Franza). We used the automatically calculated friction values for different topographic conditions based on the return period (30 years) and volume (small and tiny for Braema and Franza, respectively), as described in the RAMMS user manual (Bartelt et al., 2017). The forested areas are based on the forest characteristics specified in Swiss law (Brändli and Speich, 2007) and delineated using an orthophoto. We determined the runout distance manually as the projected run length in the main flow of the avalanche, where the maximum flow depth of the simulated avalanche drops to zero (Brožová et al., 2020). We also evaluated the maximum flow height over the simulation duration.

4.4 Results

4.4.1 Roughness classification and algorithm evaluation

Four of the seven selected roughness algorithms were found to be suitable for distinguishing the investigated vegetation types and other land-cover categories, as shown in Figure 4.4, without any overlapping pairs. However, there were important differences according to the spatial resolution and the moving-window area considered for the analysis. With only 4 of 441 possible pairs of overlapping distributions (red arrows in Figure 4.4), the algorithms generally distinguished better between categories if applied using the lowest resolution of 1 m compared with applications using higher resolutions of 0.5 m (16 overlapping out of 441 pairs) and 0.1 m (9 of 441 pairs). In the lowest resolution, only the area ratio, SD of slope and vector dispersion algorithms showed overlapping distributions in some of the categorisation, and only the vector dispersion algorithm failed in two moving-window sizes (9 and 49 m^2) in comparison to higher resolutions, where there was only one failure (Figure 4.4). Overall, we found the best differentiation between the roughness of different land-cover categories for the largest considered moving-window area of 49 m^2 in combination with the resolution of 1 m (no pairs of overlapping distribution) compared with other combinations of smaller moving-window areas of 9 or 25 m^2.

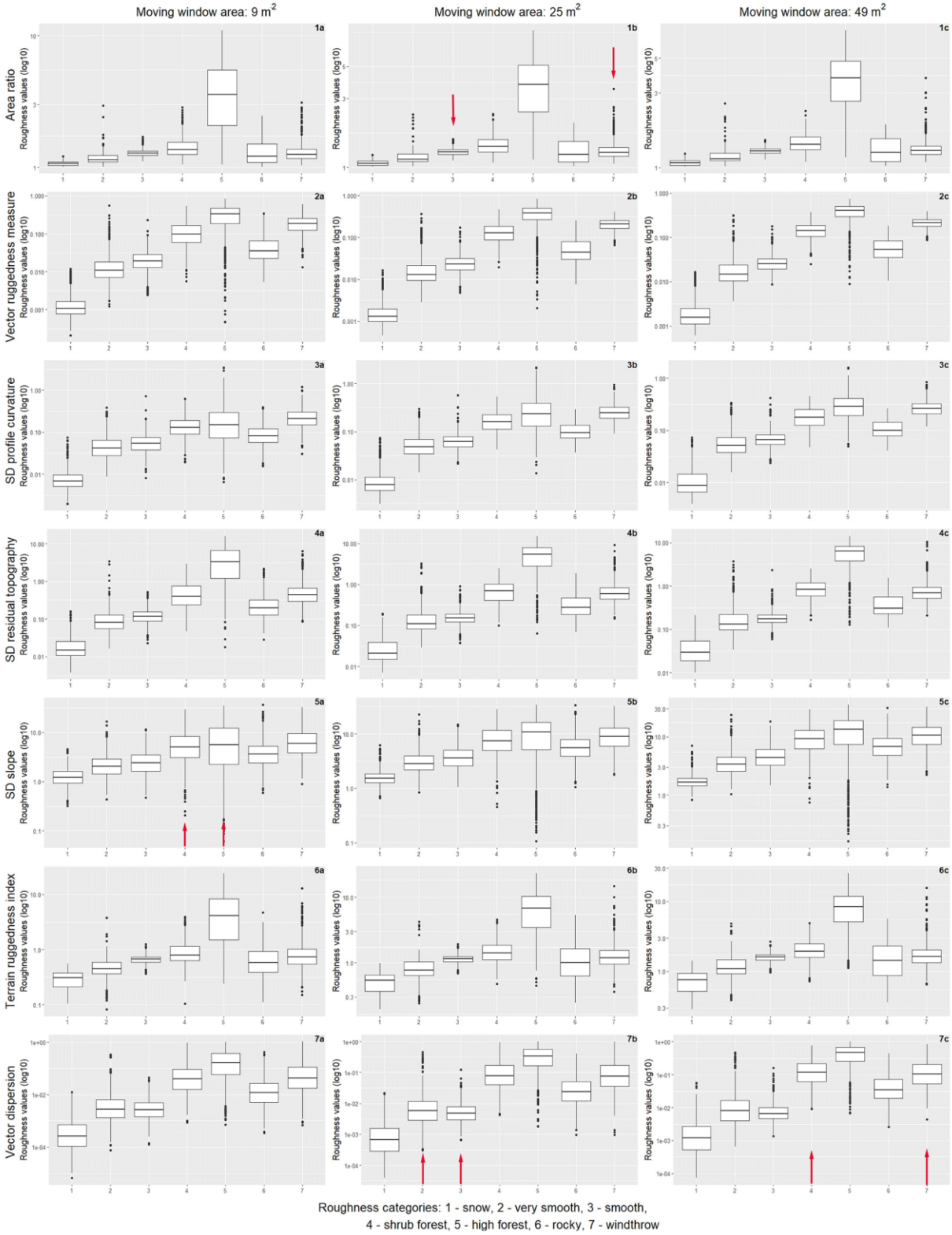

Figure 4.4: Distribution of roughness values according to different roughness categories (1 – snow, 2 – very smooth, 3 – smooth, 4 – shrub forest, 5 – high forest, 6 – rocky, 7 – windthrow) for seven algorithms (area ratio, vector ruggedness measure, SD of profile curvature, SD of residual topography, SD of slope, terrain ruggedness index and vector dispersion) for the spatial resolution of 1 m. Red arrows show the overlapping distribution for a pair of categories that the given algorithm fails to distinguish.

The best performing algorithm without any significantly overlapping distributions of pairs in all spatial resolutions (0.1, 0.5 and 1 m) and all moving-window areas (9, 25 and 49 m^2) was vector ruggedness measure. Other algorithms that performed well in distinguishing the roughness categories were SD of profile curvature, SD of residual topography and SD of slope. SD of slope had one overlapping distribution of roughness values for the category shrub forest and high forest with a resolution of 1 m and a moving-window area of 9 m^2. SD of residual topography did not distinguish between very smooth and smooth when combined with a resolution of 0.1 m and a moving-window area of 9 m^2 or between shrub forest and windthrow (resolution of 0.5 m and moving-window area of 25 m^2). SD of profile curvature did not accurately differentiate between the categories high forest and windthrow (resolution of 0.1 m and moving-window area of 49 m^2 and resolution of 0.5 m and moving-window area of 25 m^2) and between the categories very smooth and smooth (resolution of 0.5 and moving-window area of 25 m^2). The algorithms vector dispersion (4 pairs of overlapping distribution), terrain ruggedness index (6 pairs) and area ratio (13 pairs) were overall less efficient in distinguishing between different roughness and land-cover categories.

Surface roughness calculated with the seven different algorithms and normalised using the same colour range (Figure 4.5 and Figure 4.9 in Appendix, for the Braema and Franza study areas) revealed important differences in the ability to identify specific terrain and vegetation types. As visible for the overall best performing combination of resolution and moving window (1 m and 49 m^2) in Figure 4.5, all algorithms distinguished accurately between high vegetation (forest) and other vegetation types. Nevertheless, some of the algorithms (vector dispersion, SD of residual topography, terrain ruggedness index and area ratio) failed to detect the avalanche barriers correctly and falsely identified them as rather smooth. Also, small gullies were not clearly separated with some of the algorithms and were particularly poorly visible with the algorithms SD of profile curvature and SD of slope, whereas they were successfully identified with moderate roughness values by the other algorithms. Smooth surfaces were visualised with lower roughness values (darker blue in Figure 4.5) by algorithms like vector ruggedness measure, SD of residual topography and vector dispersion (panels 2, 4 and 7 in Figure 4.5). Other algorithms (panels 1, 3, 5 and 6 in Figure 4.5) assigned these smooth surfaces rather high roughness values (lighter blue to cyan blue in Figure 4.5).

The vector ruggedness measure algorithm showed the least overlapping of pairs and was found to be the best performing algorithm for our application. We determined the intersecting points within the densities of neighbouring roughness categories (Table 4.3), which may be used as thresholds for surface classification based on roughness.

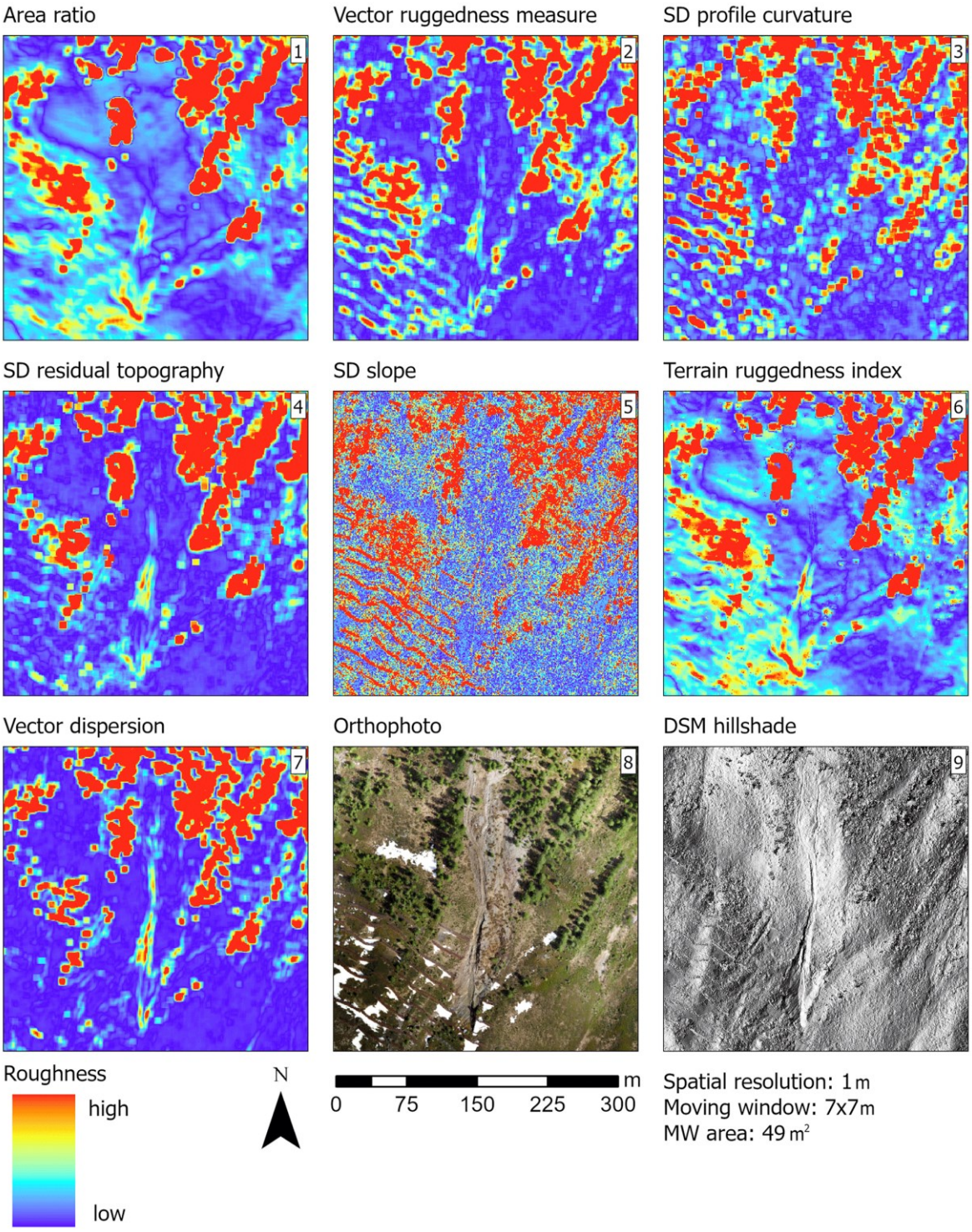

Figure 4.5: Calculated surface roughness in the study area Braema using the seven investigated algorithms: area ratio (1), vector ruggedness measure (2), SD of profile curvature (3), SD of residual topography (4), SD of slope (5), terrain ruggedness index (6) and vector dispersion (7). The same area is presented as an orthophoto (8) (drone flight, 2019) and in DSM hillshade (9) (© swisstopo). All algorithms were calculated based on the overall best performing combination of spatial resolution (1 m) and neighbourhood (moving window 7×7 m). To improve the visualisation and compare the roughness maps, we normalised them with the 25th percentile as the minimum value and the 75th percentile as the maximum one.

Table 4.3: Thresholds of roughness values between roughness categories calculated using the vector ruggedness measure algorithm, with 1 m resolution and a moving-window area of 49 m2.

Roughness category	Threshold value
Snow to very smooth	0.006
Very smooth to smooth	0.017
Smooth to rocky	0.037
Rocky to shrub forest	0.089
Shrub forest to windthrow	0.171
Windthrow to high forest	0.301

4.4.2 Directional roughness

The analysed surface roughness within gullies and valleys in the study area using the SD residual topography algorithm showed lower values for directional roughness than the non-directional one. The calculated roughness in the mass flow direction of propagation differed significantly from values calculated without using the direction ($p<0.05$, Wilcoxon test; Figure 4.6 and 4.7). In particular, for some transect parts the non-directional values were twice as large as for the directional ones. In other parts, the two roughness maps were almost equal. However, the non-directional roughness never exceeded values of the directional roughness within the selected transects.

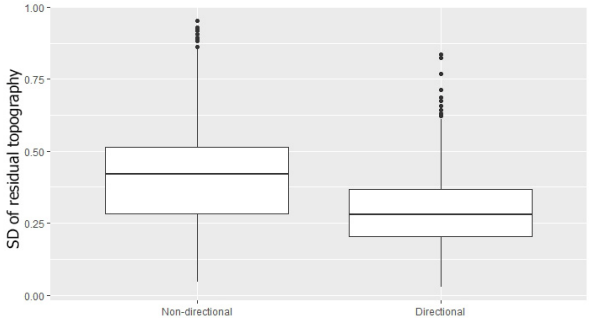

Figure 4.6: Surface roughness values calculated using non-directional and directional SD of residual topography. Using direction in the calculation of the surface roughness within the gullies resulted in values significantly lower ($p<0.05$) than those calculated with the non-directional method.

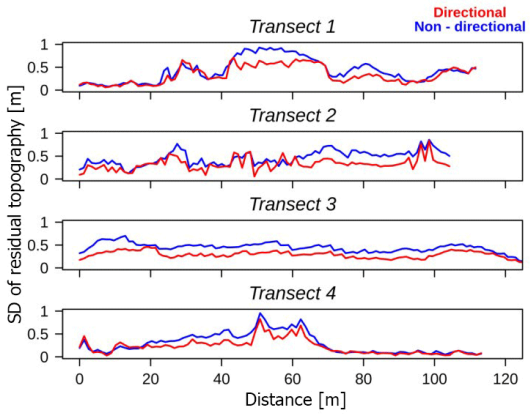

Figure 4.7: Analysis of the four transects from the Braema study area using the SD of residual topography algorithm (red) or without (blue) direction in the calculation.

4.4.3 Case study: snow avalanche modelling

Calculated surface roughness differed strongly when a DSM was used as input data instead of a DTM (Figure 4.12). In dense forest and in a windthrow area, the calculated surface roughness was overestimated, and it depicted mostly the tree crowns or branches of the fallen logs. Surface roughness calculated from the DSM considered the uppermost surface features, in comparison to calculations based on the DTM, where only terrain was considered and all the surface features were filtered out. The DTM-derived roughness values were thus lower overall compared with the DSM-derived values, in particular in the presence of forest vegetation and in the windthrow areas (Figure 4.12).

The roughness difference between DSM and DTM has important implications for the numerical simulation of gravitational mass movements, as illustrated in the avalanche simulation based on lidar data. Simulations performed using the DSM resulted in a 25 % (Braema) and 14 % (Franza) shorter runout distance and a more dispersed flow pattern than those based on the DTM (Figure 4.8 and 4.13). When using the DSM, we identified the interaction between the snow mass and the features on and above the ground, such as sparse forest and the wind-thrown areas. The maximum flow height based on the DSM was therefore 0.4 and 0.2 m greater for Braema and Franza, respectively, compared with values based on the DTM. Using the DSM, the runout distance decreased by 112 m in Braema and by 20 m in Franza. As shown in Figure 4.8, the snow mass did not impact the forested areas, and there was no tree destruction in the simulation. However, there was a visible interaction between the avalanche and the sparse trees in the runout area in the simulation based on the DSM.

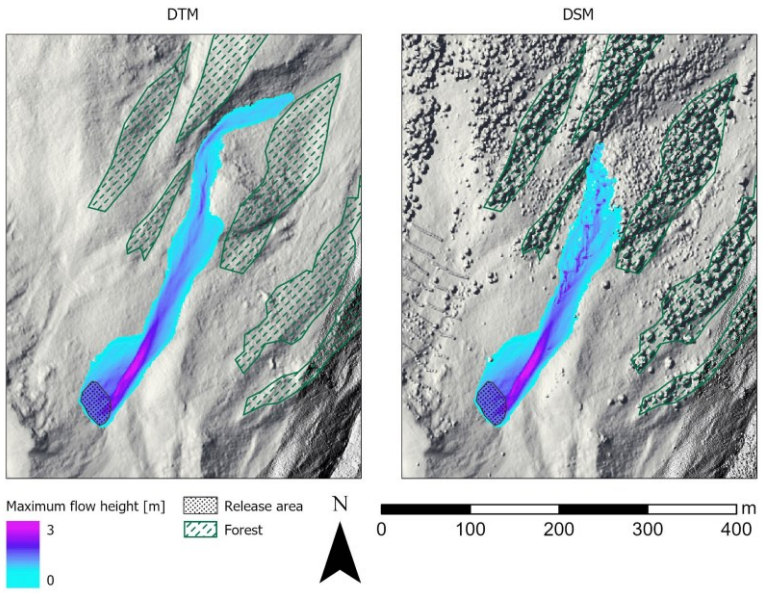

Figure 4.8: Avalanche simulation output (maximum flow height) in the Braema study area. The avalanche runout distance was 112 m greater when the DTM was used as the input model for the simulation than when the DSM was used (visualised are the hillshades calculated from the terrain and surface model swissALTI3D; © swisstopo, 2018). The maximum flow height was 0.4 m greater when the DSM was used, as a result of the interaction with the roughness features.

4.5 Discussion

4.5.1 Roughness classification and algorithm evaluation

We tested seven algorithms for calculating surface roughness, with three spatial resolutions and three moving-window areas, for terrain classification. The best performing algorithm was the vector ruggedness measure, which distinguished between the roughness categories in an accurate way for all of our tested resolutions (0.1, 0.5 and 1 m) and moving-window areas (9, 25 and 49 m2). However, the performance did not increase with higher resolution. This is probably due to the scale of our features of interest. Features in our study areas like shrubs, rocks, standing or fallen trees, and also gullies are usually in the scale of metres. These features are not that detailed as the higher resolutions of 0.1–0.5 m might be able to distinguish them. SD of profile curvature, SD of residual topography and SD of slope were also accurate in distinguishing between the roughness categories. The fewest errors across all algorithms occurred with the resolution of 1 m, where only area ratio, SD of slope and vector dispersion did not correctly classify some of the roughness categories (one error for area ratio and SD slope and two errors for vector dispersion). The lowest spatial resolution (1 m) delivered the best results, offering a reliable basis for roughness classification on larger scales. DEMs with higher resolutions, such as 0.1 and 0.5 m, are not as widespread as the 1 m resolution DEMs that are commonly available for large areas of the Alpine region. Moreover, interpretations of analysis based on data from larger areas will not be affected by potential errors in DEMs (Riley, 1999). The best performing combination of spatial resolution and moving-window area was 1 m and 49 m2 (with no pairs of overlapping distributions), which was the lowest resolution and the largest moving-window area in our analysis. The use of higher-resolution models (<1 m) had no additional advantage in our study, which is in line with findings from other studies (López-Vicente and Álvarez, 2018; Yang et al., 2014). Moreover, this result is relevant to large-scale risk evaluation and analysis, since digital models with a resolution <1 m are not so frequent. In our study, we could not find a relationship between the size of the roughness features (in metre scale) and the size of the moving-window area. The best performing moving-window area was analysed as the largest tested, 49 m2, in combination with the 1 m resolution.

All the tested algorithms had at least one combination of spatial resolution and moving-window area without a pair of overlapping distributions. The most suitable algorithm for an investigation thus depends on its purpose and the land-cover types involved. In two of the tested combinations of resolution and moving-window area (0.1 m and 49 m2, 0.5 m and 25 m2), the algorithm SD of curvature failed to distinguish between windthrow areas and high forest. With some of the combinations, three of the algorithms (area ratio, SD of residual topography and vector dispersion) did not distinguish between shrub forest and windthrow, due to the similar height and structure of these categories. If an extensive evaluation of different resolutions and moving windows is not realistic in an investigation, we suggest using the roughness algorithm vector ruggedness measure because it showed the best performance overall in

distinguishing between the roughness categories, in particular with the 1 m resolution DSM and a moving-window area of 49 m2.

The most common difficulties were in distinguishing between rocky and smooth or very smooth terrain. The algorithm area ratio failed in all combinations for the spatial resolutions of 0.1 and 0.5 m, with overlapping distributions for rocky and smooth terrains and for rocky and very smooth terrain in all three combinations of 0.5 m resolution. The algorithm terrain ruggedness index also failed in distinguishing between rocky and very smooth or smooth terrain in all combinations of 0.5 m resolution. Both of these algorithms assigned higher roughness values to the categories very smooth and smooth compared with the other algorithms. Grohmann et al. (2011) also found that area ratio showed higher values for the smooth slope of a scarp, highlighting a major disadvantage of this algorithm in that smooth steep slopes can be classified as rough. The algorithms vector dispersion, SD of residual topography, terrain ruggedness index and area ratio could not detect the avalanche barriers in the study site Braema. This might be due to small width (less than 1 m) of these objects together in combination with the relatively large moving-window area (49 m^2). Such issues might play an important role for choosing the right algorithm in natural hazard mapping.

After finding the best-performing algorithm (vector ruggedness measure), we calculated thresholds for distinguishing between the roughness categories, which may be further used in roughness classifications of other areas. These categories are a novelty in the literature, and they can be considered a preliminary proposal. However, these values must be applied carefully, as they were assigned using the vector ruggedness algorithm based on the 1 m resolution DSM and moving-window area of 49 m^2. One should also be as well cautious when defining the roughness categories since, for example, the surface of snow can be highly variable (Bühler et al., 2016). In our study, the snow surface consisted of remaining snow patches in summer and was very smooth, as shown with the lowest distribution of roughness values (Figure 4.4). We therefore propose further validation of such values over larger areas and different landscapes.

4.5.2 Surface roughness in natural hazard modelling

The assessment of surface roughness can lead to better estimation of potential avalanche release areas (Bühler et al., 2018), as well as improving avalanche simulations by including areas with high roughness values (such as RAMMS additional friction areas). In Bühler et al. (2018) the model input for large-scale avalanche release area delineation is a DTM, from which vegetation and other features are removed. Forests are handled as a binary layer so that potential release areas covered with dense forests are excluded (Bühler et al., 2018). This approach may, however, underestimate the protection function of sparse and young forests that are not officially classified as forest but influence the natural hazard dynamics for modelling purposes. In the case of avalanches, fallen logs after a windthrow event may support the snow and contribute to the stabilisation of the whole snowpack, similar to the function of shrub forests or young forests (Bebi et al., 2009; McClung and Schaerer, 2006; Schneebeli and Bebi, 2004; Teich et al., 2012a; Wohlgemuth et al., 2017). However, in the case of avalanches or debris flows releasing above the forest, fallen trees may

be entrained rather than slowing or stopping the avalanche/debris flow, as in the case for young forests (Ishikawa et al., 2000; Michelini et al., 2017; Teich et al., 2013). In debris flow simulations, surface roughness is an important input parameter in extreme scenarios, in which the flow may spread outside the main channel, flooding different terrains such as roads, rocky areas, and young and old forests (May, 2002). In this case appropriate models have to be selected with friction parameters that can be spatially distributed to include the influence of roughness (Hungr and McDougall, 2009; Mergili et al., 2017). Additionally, roughness classification can quantify surfaces affected by a land-use change (e.g. wind-thrown forest or shallow landslides), identifying new potential sediment source areas such as shallow landslides (Huebl and Fiebiger, 2007). Terrain roughness and its classification can increase both the accuracy of natural hazard simulations and the preliminary identification of potentially dangerous areas that require accurate evaluation.

4.5.3 Directional roughness

In order to further improve the applicability of roughness categories, we implemented a directional surface roughness approach. This approach helped us to better represent the surface roughness along the mass flow direction, with results that were substantially different from values assigned from a topographical point of view. Normally, gullies are considered rough using a non-directional algorithm, but they can be smoother in the direction of the dominant natural hazard flow. The directional surface roughness approach, which was available for all the tested algorithms using standard deviation, yielded lower values for roughness along the flow direction. In our study area Braema, this resulted in a more realistic assignment of channelised gully roughness, which would be categorised as very rough in a standard roughness map. Implementing directional roughness thus seems to result in more realistic results. A further improvement for surface roughness within gullies would be an automatic identification of gullies and an application of the directional algorithm automatically for a buffer area along the gullies, therefore improving the roughness maps.

4.5.4 Applications for natural hazard assessment

In our study we classified relevant land-cover types of mountain forests and treeline ecotones of the southern and central Alps. The classes represent land cover characterised by features that influence mass flow propagation in different ways. The derived roughness maps or classes could be directly used in order to improve the reliability of simulation models. Since we analysed two alpine areas, our results are also relevant for similar ecosystems characterised by coniferous forests. However, comparable analysis and a verification of the classification would be necessary in order to further generalise our results. Similarly, this would be required for the classification of other disturbed forest stands (e.g. after a bark beetle outbreak or wildfires), since different disturbances with different intensities create particular structures that most likely have unique patterns of surface roughness (Franklin et al., 2002; Hansen et al., 2016; Waldron et al., 2013).

Moreover, the surface roughness classification and the selected roughness algorithm included the identification and analysis of a forest damaged by a wind storm: the Franza case study. The forest protection

function is altered when a forest is disturbed. Therefore, there is a need for practitioners to assess the protection capacity of the remaining structures on the ground for natural hazard mapping. In the case of snow avalanches, the very small number of avalanches observed after these disturbances indicates that fallen logs contribute to increased terrain roughness and thus to the conservation of a considerable protective function against avalanches, at least for the first 2 decades after a disturbance event such as windthrow (Wohlgemuth et al., 2017). In the same way, early successional stages of post-disturbance development can provide effective protection in avalanche release zones. However, these structures are usually not classified as forest stands, since in most of cases they do not match the minimum criteria defined by the authorities (i.e. density, mean height: Brändli and Speich, 2007; FAO, 2015; INFC, 2005), so these structures might not be included in the definition of potential avalanche release areas. Fallen deadwood can also provide a residual protective function for rockfall. Thanks to the higher impact probability compared with standing trees, the flexibility of the logs on the ground in disturbed forest areas can reduce the rock velocity and absorb kinetic energy (Bourrier et al., 2012; Ringenbach et al., 2021). This is especially the case in the first phase after a disturbance, when the decaying processes have not yet reduced the wood strength (Amman, 2006). Therefore, in this study we included in the surface roughness analysis and classification these land cover types (disturbed forests, young forests and shrubs) that are usually not adequately evaluated for natural hazard modelling.

The analysis of surface roughness could therefore serve as a good proxy to evaluate some of the temporal hazard evolution in disturbed forests, but it has some limitations as well. By analysing surface roughness over time, one could additionally observe landscape transformations and changes in vegetation (natural or anthropogenic) that affect surface roughness and consequently natural hazard processes. In particular, by calculating surface roughness for different vegetation types, snow gliding could be easily modelled and predicted for different land-use scenarios. This could improve the identification of areas exposed to natural hazards and aid in the implementation of protection measures (Leitinger et al., 2008). In the case of old disturbed forest, a roughness time-series analysis might not distinguish between the roughness of old fallen logs, lower vegetation and tree regeneration. After years of decomposition, the fallen logs become less supportive, decrease in height, are moved and even decompose completely (Bebi et al., 2015; Wohlgemuth et al., 2017). A comprehensive overview of the decay process over a longer period after a disturbance (more than 20 years) would be helpful to understand the function of time and the remaining protection capacity after a disturbance such as windthrow. However, considerable variability across different environmental gradients may occur, and every area should therefore be handled individually, especially if elements of risk exist. Thus, a combination of calculated surface roughness and field investigations may be necessary in such areas (e.g. wind-thrown forest or large landslides), where an accurate evaluation of the ground features cannot be performed by a DEM survey alone.

Surface roughness further influences the estimation of avalanche release areas and avalanche propagation. Even small-scale topographic roughness can have an influence on the runout distance of ground-releasing processes, as in the case of wet snow avalanches (Sovilla et al., 2012). This is also important for small

avalanches with small release depths and a shallower snowpack (McClung, 2001), since very large snow depths can bury the surface roughness and therefore smoothen the surface (Veitinger et al., 2014). Using DSMs could improve the surface roughness estimation, as demonstrated with the vector ruggedness measure algorithm in our study. It had no pairs of overlapping distributions for all the roughness categories, and it accurately assigned high roughness values to higher vegetation, avalanche barriers and other land-cover categories. In comparison, the DTM-based approach generally underestimated the surface roughness (Brožová et al., 2020). The case study, applying numerical avalanche modelling to a DSM and a DTM, showed that surface roughness plays a decisive role in the avalanche runout distance and the flow path. However, in the case of high and dense forests, the surface roughness classification based on DSM is limited. The surface roughness values calculated from the DSM represent the tree crowns, which are classified as rough. But the crowns usually do not interact with an avalanche flow (except powder snow avalanches). Therefore, DTMs should be applied to calculate the surface roughness within dense forests, and DSMs should only be applied for open areas, where roughness may still interact with the hazard process but is not included in the forest classification. In this way, areas with increased roughness outside of defined forest areas could be detected and included within the hazard modelling. In the case of avalanches, the RAMMS simulation tool (Christen et al., 2010) offers a possibility to add an area with increased friction parameters. A smart combination of DSM and DTM data may result in better estimation of the surface roughness faced by the gravitational mass movement.

4.6 Conclusions

Our study shows that DEMs with a spatial resolution of 1 m, which are becoming increasing available, are well suited for use with roughness algorithms for natural hazard terrain classification and that higher spatial resolutions (0.1–0.5 m) do not necessarily improve the terrain surface roughness classification.

From our tested algorithms, vector ruggedness measure showed the best performance in distinguishing between different roughness categories. However, depending on the study area and relevant land-cover types, it is also possible to use other algorithms, with careful choice of spatial resolution and moving-window area. In order to avoid overestimation of terrain roughness for natural hazard applications in study areas where mass flow is continuously confined, we suggest applying the directional roughness approach. This improvement is available for any of the algorithms using a standard deviation, e.g. SD of residual topography.

Considering terrain roughness with an appropriate algorithm and in a specific spatial context may improve the generation of forest layers applied for large-scale hazard indication mapping. In particular, smaller protection forest stands, which are currently underrated and poorly investigated, could be better represented.

Finally, using DTMs in combination with DSMs may further improve the modelling of natural hazards. In fact, based on very descriptive surface roughness maps, practitioners could identify and successively

analyse areas where the implementation of protection measures is necessary to mitigate potential hazard consequences for people and infrastructure.

Code and data availability

The code for computing the terrain roughness is available at the following link: https://github.com/TommBagg/terrain_roughness_GRASS.git (last access: 11 November 2021) (DOI: https://doi.org/10.5281/zenodo.5675833, Baggio, 2021).

Data are available from the corresponding author on request.

Author contributions

NB conceptualised the research, performed the statistical analysis and RAMMS simulations, and wrote the manuscript. TB conceptualised the research, implemented the terrain roughness algorithms in code and wrote the manuscript. VD'A reviewed the manuscript and suggested the directional algorithm. YB reviewed the manuscript and structured the lidar roughness computation and RAMMS simulations. PB defined the research structure and reviewed the manuscript.

Acknowledgements

The authors wish to thank Lorenzo Martini (TESAF Department) for providing the photogrammetric survey (drone flight) of the Franza study area and Melissa Dawes for finalising our manuscript and improving the language clarity and quality of a previous version of the paper.

This research has been supported by the Fondazione Cassa di Risparmio di Padova e Rovigo (grant no. 2724/2018) and the Swiss Federal Institute for Forest, Snow and Landscape Research (SwissForestLab, CCAMM, and Swiss cantonal building insurance (KGV) grant).

4.7 Appendix

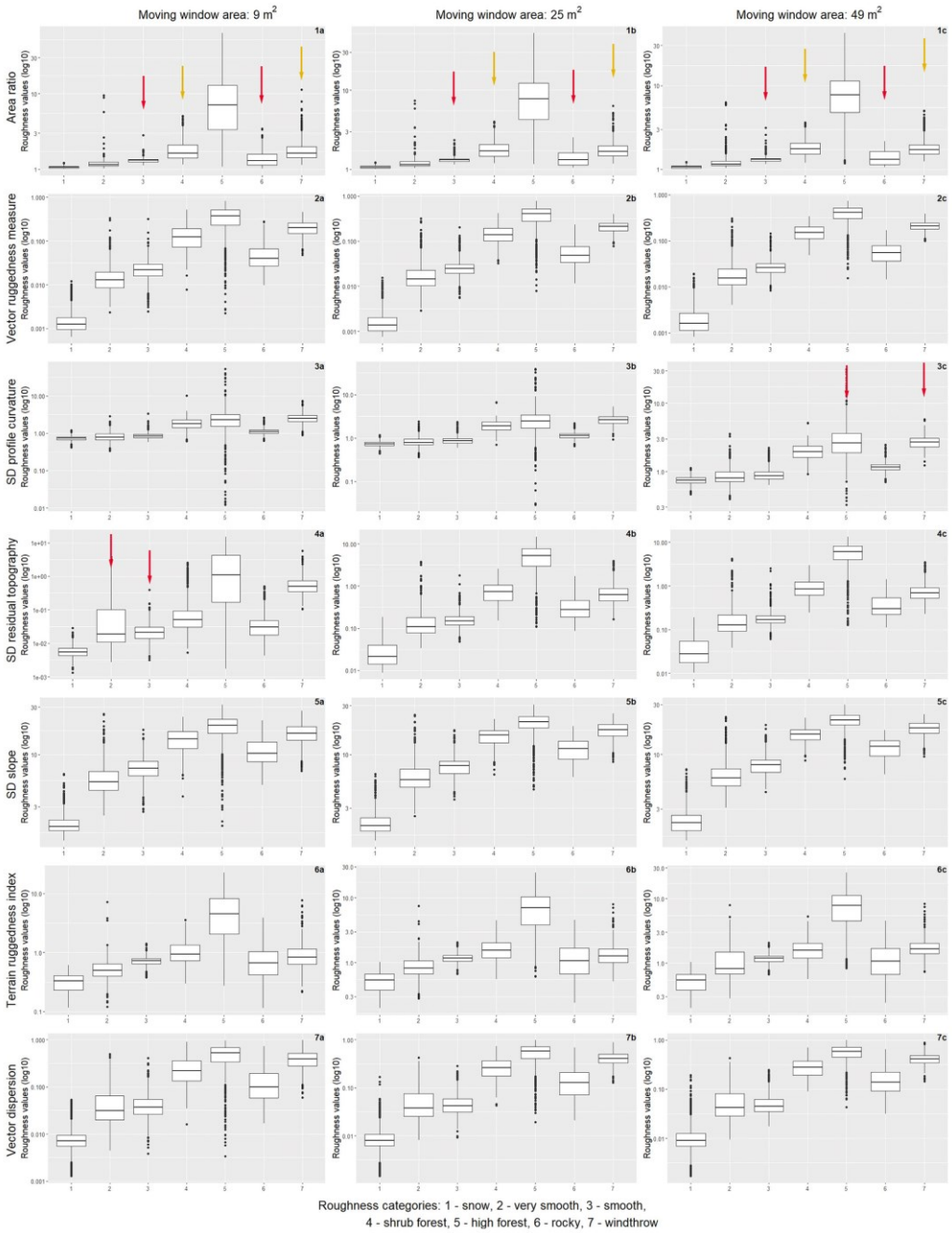

Figure 4.9: Distribution of roughness values according to different roughness categories (1 – snow, 2 – very smooth, 3 – smooth, 4 – shrub forest, 5 – high forest, 6 – rocky, 7 – windthrow) for seven algorithms (area ratio, vector ruggedness measure, SD of profile curvature, SD of residual topography, SD of slope, terrain ruggedness index and vector dispersion) for the spatial resolution of 0.1 m. Red and yellow arrows show the overlapping distribution for a pair of categories that the given algorithm fails to distinguish.

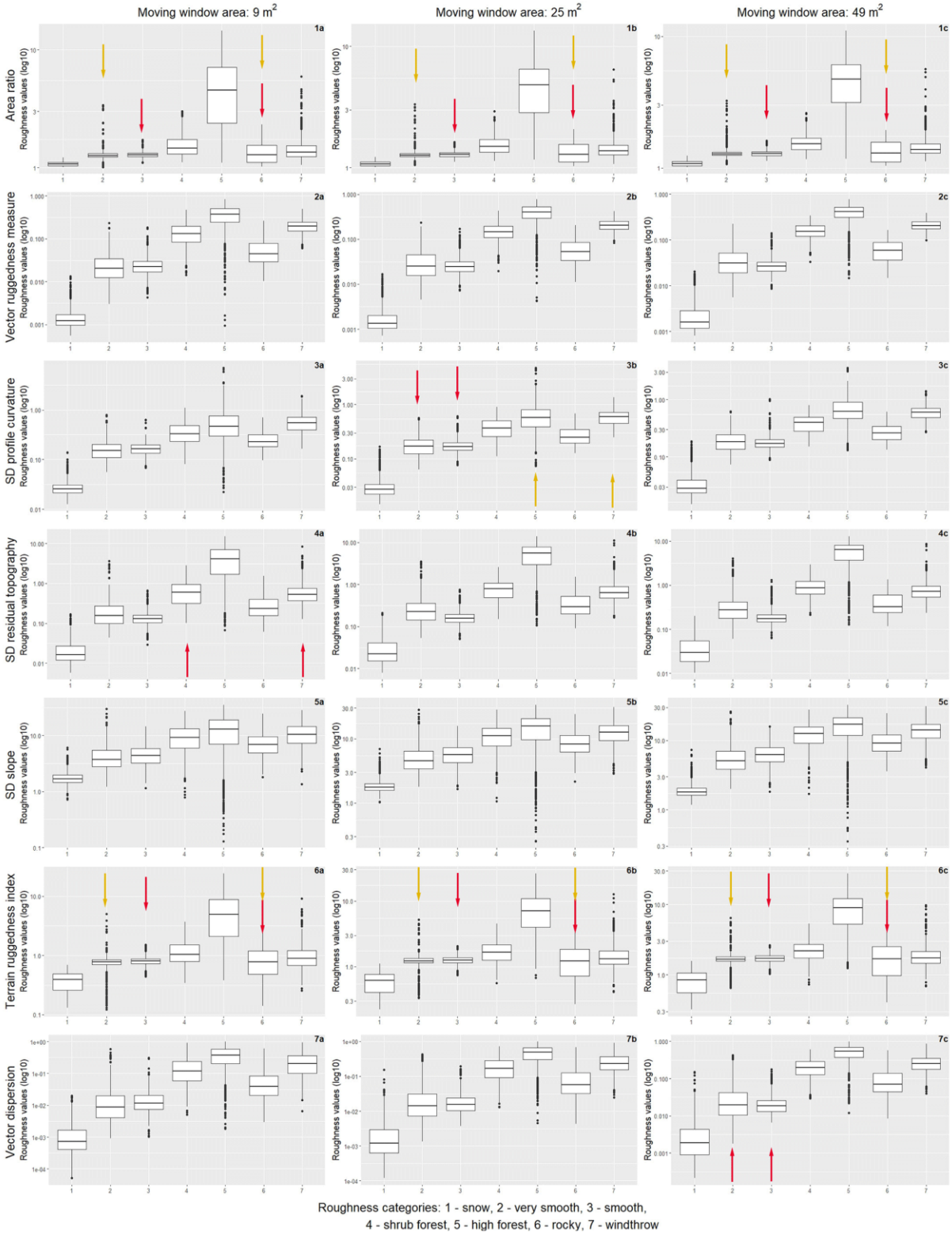

Figure 4.10: Distribution of roughness values according to different roughness categories (1 – snow, 2 – very smooth, 3 – smooth, 4 – shrub forest, 5 – high forest, 6 – rocky, 7 – windthrow) for seven algorithms (area ratio, vector ruggedness measure, SD of profile curvature, SD of residual topography, SD of slope, terrain ruggedness index and vector dispersion) for the spatial resolution of 0.5 m. Red and yellow arrows show the overlapping distribution for a pair of categories that the given algorithm fails to distinguish.

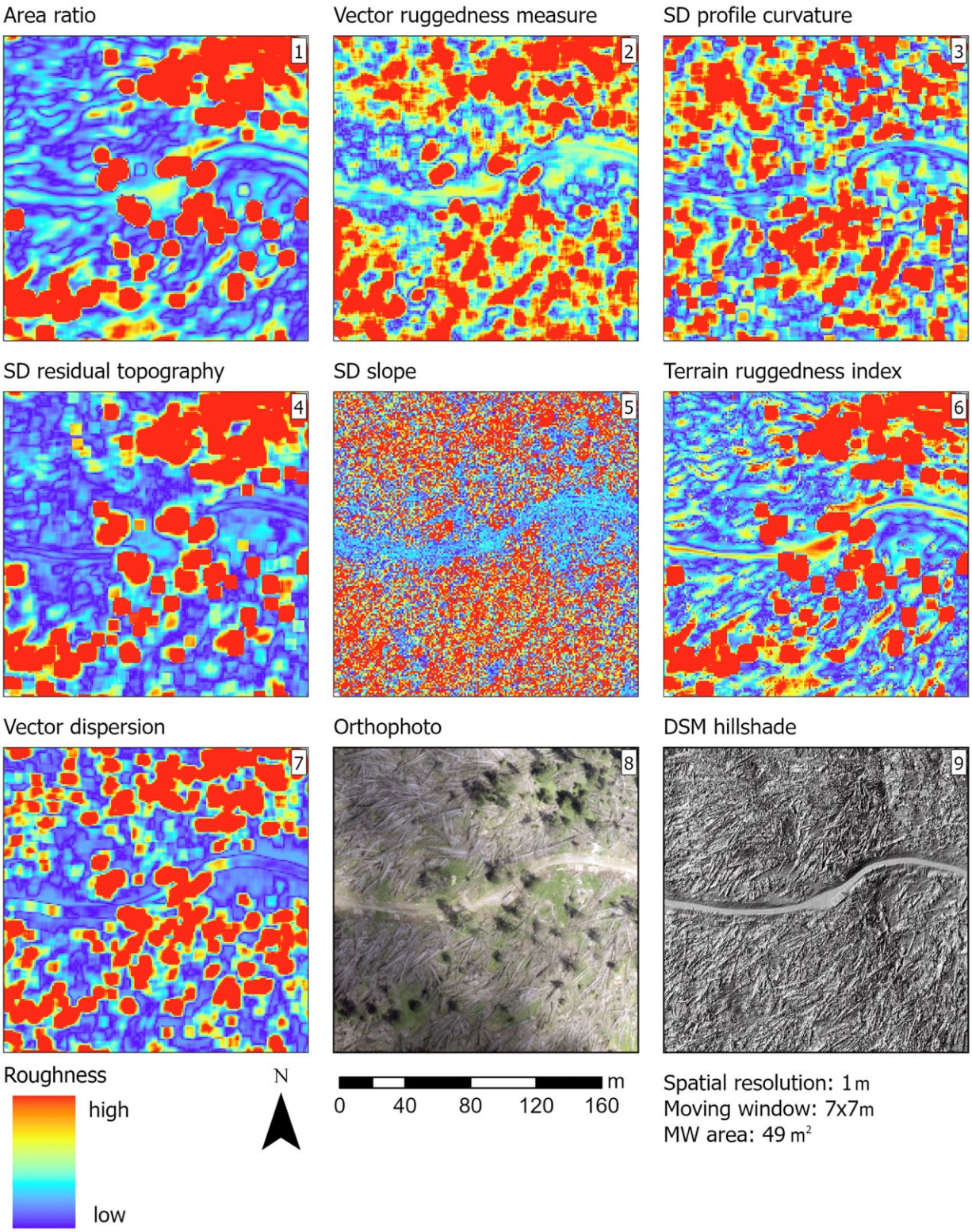

Figure 4.11: Calculated surface roughness in the study area Franza using the seven investigated algorithms: area ratio (1), vector ruggedness measure (2), SD of profile curvature (3), SD of residual topography (4), SD of slope (5), terrain ruggedness index (6) and vector dispersion (7). The same area is presented as an orthophoto (8) (drone flight, 2019) and in DSM hillshade (9) (lidar data provided by the region Veneto). All algorithms were calculated based on the overall best performing combination of spatial resolution (1 m) and neighbourhood (moving window 7×7 m). To improve the visualisation and compare the roughness maps, we normalised them with the 25th percentile as the minimum value and the 75th percentile as the maximum one.

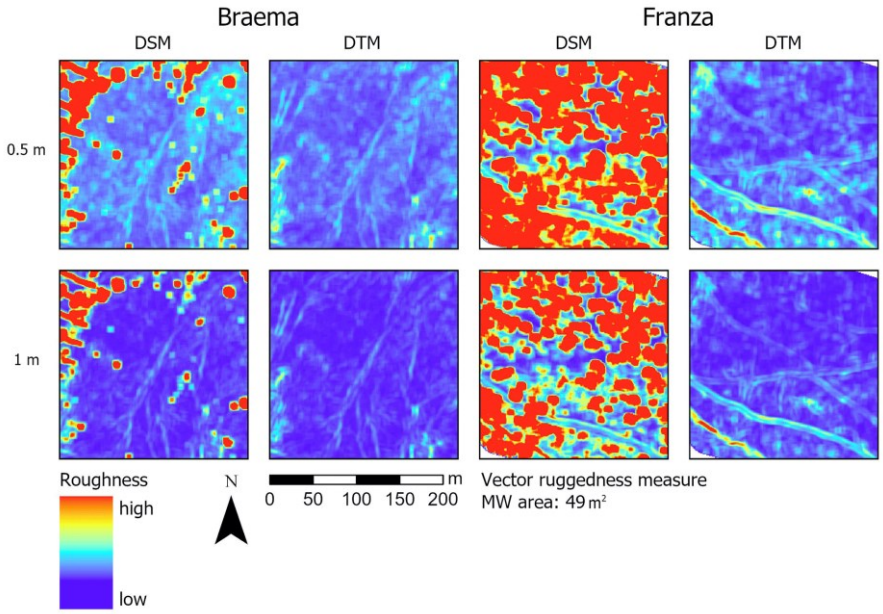

Figure 4.12: Calculated surface roughness in the two study areas Braema and Franza, using DSM and DTM (© swisstopo for Braema, region Veneto for Franza) and the vector ruggedness measure algorithm.

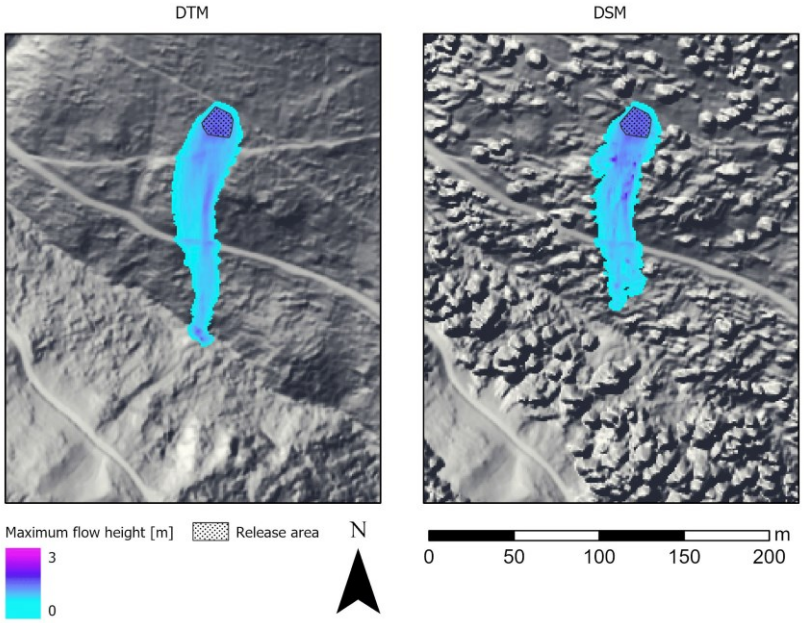

Figure 4.13: Avalanche simulation output (maximum flow height) in the Franza study area. The avalanche runout distance was 20 m longer when the DTM was used as the input model for the simulation than when the DSM was used (lidar data provided by the region Veneto). The maximum flow height was 0.2 m greater when the DSM was used, as a result of the interaction with the roughness features.

4.8 References

Amman, M.: Schutzwirkung abgestorbener Bäume gegen Naturgefahren, PhD thesis, Eidgenössische Forschungsanstalt für Wald, Schnee und Landschaft, ETH Zürich, Zurich, Switzerland, 240 pp., 2006.

Baggio, T.: TommBagg/terrain_roughness_GRASS: Roughness calculation in GRASS, v1.0, Zenodo [code], https://doi.org/10.5281/zenodo.5675833, 2021.

Baroni, C., Armiraglio, S., Gentili, R., and Carton, A.: Landform-vegetation units for investigating the dynamics and geomorphologic evolution of alpine composite debris cones (Valle dell'Avio, Adamello Group, Italy), Geomorphology, 84, 59–79, https://doi.org/10.1016/j.geomorph.2006.07.002, 2007.

Bartelt, P., Bühler, Y., Christen, M., Deubelbeiss, Y., Salz, M., Schneider, M., and Schumacher, L.: A numerical model for snow avalanches in research and practice, RAMMS User Manual v. 1.7. 0 Avalanche, WSL Institute for Snow and Avalanche Research SLF, Davos, 104 pp., 2017.

Bebi, P., Kulakowski, D., and Rixen, C.: Snow avalanche disturbances in forest ecosystems-State of research and implications for management, Forest. Ecol. Manag., 257, 1883–1892, https://doi.org/10.1016/j.foreco.2009.01.050, 2009.

Bebi, P., Putallaz, J. M., Fankhauser, M., Schmid, U., Schwitter, R., and Gerber, W.: Die Schutzfunktion in Windwurfflächen, Schweizerische Zeitschrift fur Forstwes., 166, 168–176, https://doi.org/10.3188/szf.2015.0168, 2015.

Bebi, P., Seidl, R., Motta, R., Fuhr, M., Firm, D., Krumm, F., Conedera, M., Ginzler, C., Wohlgemuth, T., and Kulakowski, D.: Changes of forest cover and disturbance regimes in the mountain forests of the Alps, Forest. Ecol. Manag., 388, 43–56, https://doi.org/10.1016/j.foreco.2016.10.028, 2017.

Bigot, C., Dorren, L. K. A., and Berger, F.: Quantifying the protective function of a forest against rockfall for past, present and future scenarios using two modelling approaches, Nat. Hazards, 49, 99–111, https://doi.org/10.1007/s11069-008-9280-0, 2009.

Bourrier, F., Dorren, L., and Berger, F.: Full scale tests on rockfall impacting trees felled transverse to the slope, in: Interpraevent, Grenoble, pp. 643–650, available at: http://www.interpraevent.at (last access: 3 November 2020), 2012.

Brändli, U. B. and Speich, S.: Swiss NFI glossary and dictionary, Birmensdorf, Swiss Federal Research Institute WSL, available at: https://www.lfi.ch/glossar/glossar-en.php (last access: 17 November 2020), 2007.

Brožová, N., Fischer, J. T., Bühler, Y., Bartelt, P., and Bebi, P.: Determining forest parameters for avalanche simulation using remote sensing data, Cold Reg. Sci. Technol., 172, 102976, https://doi.org/10.1016/j.coldregions.2019.102976, 2020.

Bühler, Y., Christen, M., Kowalski, J., and Bartelt, P.: Sensitivity of snow avalanche simulations to digital elevation model quality and resolution, Ann. Glaciol., 52, 72–80, https://doi.org/10.3189/172756411797252121, 2011.

Bühler, Y., Kumar, S., Veitinger, J., Christen, M., Stoffel, A., and Snehmani: Automated identification of potential snow avalanche release areas based on digital elevation models, Nat. Hazards Earth Syst. Sci., 13, 1321–1335, https://doi.org/10.5194/nhess-13-1321-2013, 2013.

Bühler, Y., von Rickenbach, D., Stoffel, A., Margreth, S., Stoffel, L., and Christen, M.: Automated snow avalanche release area delineation – validation of existing algorithms and proposition of a new object-based approach for large-scale hazard indication mapping, Nat. Hazards Earth Syst. Sci., 18, 3235–3251, https://doi.org/10.5194/nhess-18-3235-2018, 2018.

Busse, A. and Jelly, T. O.: Influence of Surface Anisotropy on Turbulent Flow Over Irregular Roughness, Flow Turbul. Combust., 104, 331–354, https://doi.org/10.1007/s10494-019-00074-4, 2020.

Cavalli, M. and Marchi, L.: Characterisation of the surface morphology of an alpine alluvial fan using airborne LiDAR, Nat. Hazards Earth Syst. Sci., 8, 323–333, https://doi.org/10.5194/nhess-8-323-2008, 2008.

Cavalli, M., Tarolli, P., Marchi, L., and Dalla Fontana, G.: The effectiveness of airborne LiDAR data in the recognition

of channel-bed morphology, Catena, 73, 249–260, https://doi.org/10.1016/j.catena.2007.11.001, 2008.

Caviezel, A., Demmel, S. E., Ringenbach, A., Bühler, Y., Lu, G., Christen, M., Dinneen, C. E., Eberhard, L. A., von Rickenbach, D., and Bartelt, P.: Reconstruction of four-dimensional rockfall trajectories using remote sensing and rock-based accelerometers and gyroscopes, Earth Surf. Dynam., 7, 199–210, https://doi.org/10.5194/esurf-7-199-2019, 2019.

Christen, M., Kowalski, J., and Bartelt, P.: RAMMS: Numerical simulation of dense snow avalanches in three-dimensional terrain, Cold Reg. Sci. Technol., 63, 1–14, https://doi.org/10.1016/j.coldregions.2010.04.005, 2010.

Crosta, G. B. and Agliardi, F.: Parametric evaluation of 3D dispersion of rockfall trajectories, Nat. Hazards Earth Syst. Sci., 4, 583–598, https://doi.org/10.5194/nhess-4-583-2004, 2004.

Dorren, L., Berger, F., Frehner, M., Huber, M., Kühne, K., Métral, R., Sandri, A., Schwitter, R., Thormann, J.-J., and Wasser, B.: Das neue NaiS-Anforderungsprofil Steinschlag, Schweizerische Zeitschrift fur Forstwes., 166, 16–23, https://doi.org/10.3188/szf.2015.0016, 2015.

Dorren, L. K. A., Berger, F., Le Hir, C., Mermin, E., and Tardif, P.: Mechanisms, effects and management implications of rockfall in forests, For. Ecol. Manag., 215, 183–195, https://doi.org/10.1016/j.foreco.2005.05.012, 2005.

Durrant, A.: Vectors in physics and engineering, CRC Press, Taylor & Francis Group, Boca Raton, 310 pp., ISBN 978-0-2037-3439-1, 1996.

Elliott, G. P.: Treeline Ecotones, in: International Encyclopedia of Geography: People, the Earth, Environment and Technology, edited by: Richardson, D., Castree, N., Goodchild, M. F., Kobayashi, A., Liu, W., and Marston, R. A., John Wiley & Sons, Ltd, Oxford, UK, 10 pp., https://doi.org/10.1002/9781118786352, 2017.

Endo, Y.: Glide Processes of a Snow Cover as a Release Mechanism of an Avalanche on a Slope Covered with Bamboo Bushes, Low Temp. Sci., 32, 39–68, 1983.

Evans, I.: Correlation Structures and Factor Analysis in the Investigation of Data dimensionality: Statistical Properties of the Wessex Land Surface, England, in: Proceeding of the international symposium on spatial data handling, Zurich, Switzerland, 20–25 August 1984, vol. 2, pp. 98–116., 1984.

FAO: Forest Resources Assessment 2015, Terms and Definitions, Rome, available at: https://www.fao.org/forestry/fra (last access: 30 March 2020), 2015.

Feistl, T., Bebi, P., Dreier, L., Hanewinkel, M., and Bartelt, P.: Quantification of basal friction for technical and silvicultural glide-snow avalanche mitigation measures, Nat. Hazards Earth Syst. Sci., 14, 2921–2931, https://doi.org/10.5194/nhess-14-2921-2014, 2014.

Feistl, T., Bebi, P., Christen, M., Margreth, S., Diefenbach, L., and Bartelt, P.: Forest damage and snow avalanche flow regime, Nat. Hazards Earth Syst. Sci., 15, 1275–1288, https://doi.org/10.5194/nhess-15-1275-2015, 2015.

Fisher, R. A.: Dispersion on a sphere, Proc. R. Soc. London. Ser. A. Math. Phys. Sci., 217, 295–305, 1953.

Frank, F., McArdell, B. W., Oggier, N., Baer, P., Christen, M., and Vieli, A.: Debris-flow modeling at Meretschibach and Bondasca catchments, Switzerland: sensitivity testing of field-data-based entrainment model, Nat. Hazards Earth Syst. Sci., 17, 801–815, https://doi.org/10.5194/nhess-17-801-2017, 2017.

Franklin, J. F., Spies, T. A., Pelt, R. Van, Carey, A. B., Thornburgh, D. A., Berg, D. R., Lindenmayer, D. B., Harmon, M. E., Keeton, W. S., Shaw, D. C., Bible, K., and Chen, J.: Disturbances and structural development of natural forest ecosystems with silvicultural implications, using Douglas-fir forests as an example, Forest. Ecol. Manag., 155, 399–423, https://doi.org/10.1016/S0378-1127(01)00575-8, 2002.

Fuhr, M., Bourrier, F., and Cordonnier, T.: Protection against rockfall along a maturity gradient in mountain forests, Forest. Ecol. Manag., 354, 224–231, https://doi.org/10.1016/j.foreco.2015.06.012, 2015.

Gille, S. T., Yale, M. M., and Sandwell, D. T.: Global correlation of mesoscale ocean variability with seafloor roughness from satellite altimetry, Geophys. Res. Lett., 27, 1251–1254, https://doi.org/10.1029/1999GL007003, 2000.

Glenn, N. F., Streutker, D. R., Chadwick, D. J., Thackray, G. D., and Dorsch, S. J.: Analysis of LiDAR-derived topographic information for characterizing and differentiating landslide morphology and activity, Geomorphology, 73, 131–148, https://doi.org/10.1016/j.geomorph.2005.07.006, 2006.

GRASS Development Team: Geographic Resources Analysis Support System (GRASS) Software, Version 7.8, available at: http://grass.osgeo.org (last access: 10 January), 2021.

Grohmann, C. H. and Riccomini, C.: Comparison of roving-window and search-window techniques for characterising landscape morphometry, Comput. Geosci., 35, 2164–2169, https://doi.org/10.1016/j.cageo.2008.12.014, 2009.

Grohmann, C. H., Smith, M. J., and Riccomini, C.: Multiscale analysis of topographic surface roughness in the Midland Valley, Scotland, IEEE Trans. Geosci. Remote Sens., 49, 1200–1213, https://doi.org/10.1109/TGRS.2010.2053546, 2011.

Guo, J., Yi, S., Yin, Y., Cui, Y., Qin, M., Li, T., and Wang, C.: The effect of topography on landslide kinematics: a case study of the Jichang town landslide in Guizhou, China, Landslides, 17, 959–973, https://doi.org/10.1007/s10346-019-01339-9, 2020.

Haneberg, W. C., Creighton, A. L., Medley, E. W., and Jonas, D. A.: Use of LiDAR to assess slope hazards at the Lihir gold mine, Papua New Guinea, in: Proceedings of International Conference on Landslide Risk Management, edited by: Hungr, O., Fell, R., Couture, R., and Eberhard, E., Vancouver, 31 May–3 June 2005, 2005.

Hansen, W. D., Chapin, F. S., Naughton, H. T., Rupp, T. S., and Verbyla, D.: Forest-landscape structure mediates effects of a spruce bark beetle (Dendroctonus rufipennis) outbreak on subsequent likelihood of burning in Alaskan boreal forest, Forest. Ecol. Manag., 369, 38–46, https://doi.org/10.1016/j.foreco.2016.03.036, 2016.

Harsch, M. A., Hulme, P. E., McGlone, M. S., and Duncan, R. P.: Are treelines advancing? A global meta-analysis of treeline response to climate warming, Ecol. Lett., 12, 1040–1049, https://doi.org/10.1111/j.1461-0248.2009.01355.x, 2009.

Hobson, R. D.: FORTRAN IV programs to determine the surface roughness in topography for the CDC 3400 computer, Comput. Contrib. State Geol. Surv. Kansas, 14, 1–28, 1967.

Höller, P.: Snow gliding and avalanches in a south-facing, in: Soil-vegetation-atmosphere Transfer Schemes and Large-scale Hydrological Models: Proceedings of an International Symposium (Symposium S5) Held During the Sixth Scientific Assembly of the International Association of Hydrological Sciences (IAHS), Maastricht, the Netherlands, 18–27 July 2001, No. 270, p. 355–358, 2001.

Höller, P.: Snow gliding on a south-facing slope covered with larch trees, Ann. For. Sci., 71, 81–89, https://doi.org/10.1007/s13595-013-0333-5, 2013.

Horn, B. K. P.: Hill shading and the reflectance map, in Proceeding of the IEEE, pp. 14–47, available at: https://ieeexplore.ieee.org/stamp/stamp.jsp?tp=&arnumber=1456186 (last access: 26 March 2020), 1981.

Huebl, J. and Fiebiger, G.: Debris-flow mitigation measures, in Debris-flow Hazards and Related Phenomena, Springer, Berlin, 445–487, ISBN 3-540-20726-0, 2007.

Hungr, O. and McDougall, S.: Two numerical models for landslide dynamic analysis, Comput. Geosci., 35, 978–992, https://doi.org/10.1016/j.cageo.2007.12.003, 2009.

INFC: Inventario nazionale delle foreste e dei serbatoi di carbonio, available at: https://www.sian.it/inventarioforestale/ (last access: 30 March 2020), 2005.

Insua-Arévalo, J. M., Tsige, M., Sánchez-Roldán, J. L., Rodríguez-Escudero, E., and Martínez-Díaz, J. J.: Influence of the microstructure and roughness of weakness planes on the strength anisotropy of a foliated clay-rich fault gouge, Eng. Geol., 289, 106186, https://doi.org/10.1016/j.enggeo.2021.106186, 2021.

Ishikawa, Y., Mizuhara, K., and Ashida, S.: Effect of density of trees on drag exerted on trees in river channels, J. For. Res., 5, 271–279, https://doi.org/10.1007/BF02767121, 2000.

Iverson, R. M., George, D. L., and Logan, M.: Debris flow runup on vertical barriers and adverse slopes, J. Geophys. Res.-Earth, 121, 2333–2357, https://doi.org/10.1002/2016JF003933, 2016.

Jakob, M., Hungr, O., and Jakob, D.: Debris-flow hazards and related phenomena, edited by: Blonde, P., Springer, Berlin, 795 pp., ISBN 3-540-20726-0, available at: https://link.springer.com/content/pdf/10.1007/b138657.pdf (last access: 27 November 2018), 2005.

Jonsson, M. J. O.: Energy absorption of trees in a rockfall protection forest, PhD thesis, Swiss Federal Institute of

Technology, Zurich, 209 pp., 2007.

Koponen, P., Nygren, P., Sabatier, D., Rousteau, A., and Saur, E.: Tree species diversity and forest structure in relation to microtopography in a tropical freshwater swamp forest in French Guiana, Plant Ecol., 173, 17–32, https://doi.org/10.1023/B:VEGE.0000026328.98628.b8, 2004.

Lehning, M., Grünewald, T., and Schirmer, M.: Mountain snow distribution governed by an altitudinal gradient and terrain roughness, Geophys. Res. Lett., 38, 1–5, https://doi.org/10.1029/2011GL048927, 2011.

Leitinger, G., Höller, P., Tasser, E., Walde, J., and Tappeiner, U.: Development and validation of a spatial snow-glide model, Ecol. Modell., 211, 363–374 https://doi.org/10.1016/j.ecolmodel.2007.09.015, 2008.

Lopez-Saez, J., Corona, C., Eckert, N., Stoffel, M., Bourrier, F., and Berger, F.: Impacts of land-use and land-cover changes on rockfall propagation: Insights from the Grenoble conurbation, Sci. Total Environ., 547, 345–355, https://doi.org/10.1016/j.scitotenv.2015.12.148, 2016.

López-Vicente, M. and Álvarez, S.: Influence of DEM resolution on modelling hydrological connectivity in a complex agricultural catchment with woody crops, Earth Surf. Process. Landforms, 43, 1403–1415, https://doi.org/10.1002/esp.4321, 2018.

May, C. L.: Debris flows through different forest age classes in the central Oregon Coast Range, J. Am. Water Resour. Assoc., 38, 1097–1113., 2002.

McClung, D. and Schaerer, P.: The avalanche handbook, third edn., edited by: Ummel Hoster, C., in: The mountaineers books, Seattle, WA, ISBN 0-89886-809-2, available at: https://books.google.it/books?hl=it&lr=&id=0Bpscs7Gqb8C&oi=fnd&pg=PA6&dq=The+avalanche+handbook&ots=vXt8PraiDb&sig=5rP0r0NvfZK8-IeKckmYAgrkLt8 (last access: 21 September 2020), 2006.

McClung, D. M. M.: Characteristics of terrain, snow supply and forest cover for avalanche initiation caused by logging, Ann. Glaciol., 32, 223–229, 2001.

McKean, J. and Roering, J.: Objective landslide detection and surface morphology mapping using high-resolution airborne laser altimetry, Geomorphology, 57, 331–351, https://doi.org/10.1016/S0169-555X(03)00164-8, 2004.

Mergili, M., Fischer, J.-T., Krenn, J., and Pudasaini, S. P.: r.avaflow v1, an advanced open-source computational framework for the propagation and interaction of two-phase mass flows, Geosci. Model Dev., 10, 553–569, https://doi.org/10.5194/gmd-10-553-2017, 2017.

Michelini, T.: Analisi Sperimentale Delle Scabrezze Di Superficie E Di Fondo Per La Modellazione Dinamica Dei Flussi Torrentizi E Della Caduta Massi, available at: http://paduaresearch.cab.unipd.it/9407/1/Tesi_Tamara_Michelini.pdf (last access: 26 February 2021), 2016.

Michelini, T., Bettella, F., and D'Agostino, V.: Field investigations of the interaction between debris flows and forest vegetation in two Alpine fans, Geomorphology, 279, 150–164, https://doi.org/10.1016/j.geomorph.2016.09.029, 2017.

Middleton, M., Nevalainen, P., Hyvönen, E., Heikkonen, J., and Sutinen, R.: Pattern recognition of LiDAR data and sediment anisotropy advocate a polygenetic subglacial mass-flow origin for the Kemijärvi hummocky moraine field in northern Finland, Geomorphology, 362, 107212, https://doi.org/10.1016/j.geomorph.2020.107212, 2020.

Mina, M., Bugmann, H., Cordonnier, T., Irauschek, F., Klopcic, M., Pardos, M., and Cailleret, M.: Future ecosystem services from European mountain forests under climate change, J. Appl. Ecol., 54, 389–401, https://doi.org/10.1111/1365-2664.12772, 2017.

Mitasova, H.: Cartographic aspects of computer surface modelling, PhD thesis, Slovak Technical University, Bratislava, 1985.

Myers-Smith, I. H., Elmendorf, S. C., Beck, P. S. A., Wilmking, M., Hallinger, M., Blok, D., Tape, K. D., Rayback, S. A., Macias-Fauria, M., Forbes, B. C., Speed, J. D. M., Boulanger-Lapointe, N., Rixen, C., Lévesque, E., Schmidt, N. M., Baittinger, C., Trant, A. J., Hermanutz, L., Collier, L. S., Dawes, M. A., Lantz, T. C., Weijers, S., JØrgensen, R. H., Buchwal, A., Buras, A., Naito, A. T., Ravolainen, V., Schaepman-Strub, G., Wheeler, J. A., Wipf, S., Guay, K. C., Hik, D. S., and Vellend, M.: Climate sensitivity of shrub growth across the tundra biome, Nat. Clim. Change., 5, 887–891, https://doi.org/10.1038/nclimate2697, 2015.

Nel, J. L., Le Maitre, D. C., Nel, D. C., Reyers, B., Archibald, S., van Wilgen, B. W., Forsyth, G. G., Theron, A. K., O'Farrell, P. J., Kahinda, J.-M. M., Engelbrecht, F. A., Kapangaziwiri, E., van Niekerk, L., and Barwell, L.: Natural Hazards in a Changing World: A Case for Ecosystem-Based Management, edited by: Magar, V., PLoS One, 9, e95942, https://doi.org/10.1371/journal.pone.0095942, 2014.

Nguyen, H. T. and Fenton J. D.: Identification of roughness for flood routing in compound channels, Proc. 31st Congress, Int. Assoc. Hydraulic Engng and Res., Seoul, Korea, 11–16 September 2005, 2005.

O'Brien, J. S., Julien, P. Y., and Fullerton, W. T.: Two-Dimensional Water Flood and Mudflow Simulation, J. Hydraul. Eng., 119, 244–261, https://doi.org/10.1061/(asce)0733-9429(1993)119:2(244), 1993.

Palomo, I.: Climate change impacts on ecosystem services in high mountain areas: A literature review, Mt. Res. Dev., 37, 179–187, https://doi.org/10.1659/MRD-JOURNAL-D-16-00110.1, 2017.

Pastore, M.: Overlapping: a R package for estimating overlapping in empirical distributions, J. Open Source Softw., 3, 1023, https://doi.org/10.21105/joss.01023, 2018.

Pastore, M. and Calcagnì, A.: Measuring distribution similarities between samples: A distribution-free overlapping index, Front. Psychol., 10, 1–8, https://doi.org/10.3389/fpsyg.2019.01089, 2019.

Pfeiffer, T. J. and Bowen, T. D.: Computer simulation of rockfalls, Bull.-Assoc. Eng. Geol., 26, 135–146, https://doi.org/10.2113/gseegeosci.xxvi.1.135, 1989.

Philip, G. M. and Watson, D. F.: A method for assessing local variation among scattered measurements, Math. Geol., 18, 759–764, https://doi.org/10.1007/BF00899742, 1986.

Pincus, H. J.: Some vector and arithmetic operations on two-dimensional orientation variates, with applications to geological data, J. Geol., 64, 553–556, https://doi.org/10.1086/626391, 1956.

Pudasaini, S. P.: A general two-phase debris flow model, J. Geophys. Res.-Earth Surf., 117, 1–28, https://doi.org/10.1029/2011JF002186, 2012.

Pudasaini, S. P. and Mergili, M.: A Multi-Phase Mass Flow Model, J. Geophys. Res.-Earth Surf., 124, 1–23, https://doi.org/10.1029/2019jf005204, 2019.

R Core Team: R: A language and environment for statistical computing, R Found. Stat. Comput., available at: http://www.r-project.org (last access: 28 January), 2021.

Riley, S.: Index that quantifies topographic heterogeneity, Intermt. J. Sci., 5, 23–27, 1999.

Riley, S. J., DeGloria, S. D., and Elliot, R.: A terrain ruggedness index that quantifies topographic heterogeneity, Intermt. J. Sci., 5, 23–27, 1999.

Ringenbach, A., Caviezel, A., Lu, G., Christen, M., Bebi, P., and Bartelt, P.: Rockfall experiments in forests: Influence of rock-shape and deadwood, in Interpraevent, in: 14th Congress INTERPRAEVENT, Bergen, Norway, 31 May to 2 June 2021, 2021.

Rosatti, G. and Begnudelli, L.: Two-dimensional simulation of debris flows over mobile bed: Enhancing the TRENT2D model by using a well-balanced Generalized Roe-type solver, Comput. Fluids, 71, 179–195, https://doi.org/10.1016/j.compfluid.2012.10.006, 2013.

Roy, S. G., Koons, P. O., Osti, B., Upton, P., and Tucker, G. E.: Multi-scale characterization of topographic anisotropy, Comput. Geosci., 90, 102–116, https://doi.org/10.1016/j.cageo.2015.09.023, 2016.

Sappington, J. M., Longshore, K. M., and Thompson, D. B.: Quantifying landscape ruggedness for animal habitat analysis: a case study using bighorn sheep in the Mojave Desert, J. Wildlife Manage., 71, 1419–1426, https://doi.org/10.2193/2005-723, 2007.

Schneebeli, M. and Bebi, P.: HYDROLOGY | Snow and Avalanche Control, in: Encyclopedia of Forest Sciences, pp. 397–402, https://doi.org/10.1016/B0-12-145160-7/00271-4, 2004.

Schumann, G., Matgen, P., Hoffmann, L., Hostache, R., Pappenberger, F., and Pfister, L.: Deriving distributed roughness values from satellite radar data for flood inundation modelling, J. Hydrol., 344, 96–111, https://doi.org/10.1016/j.jhydrol.2007.06.024, 2007.

Schweizer, J., Jamieson, J. B. and Schneebeli, M.: Snow avalanche formation, Rev. Geophys., 41, 1016, https://doi.org/10.1029/2002RG000123, 2003.

Seidl, R., Thom, D., Kautz, M., Martin-Benito, D., Peltoniemi, M., Vacchiano, G., Wild, J., Ascoli, D., Petr, M., Honkaniemi, J., Lexer, M. J., Trotsiuk, V., Mairota, P., Svoboda, M., Fabrika, M., Nagel, T. A., and O Reyer, C. P.: Forest disturbances under climate change, Nat. Clim. Change, 7, 395–402, https://doi.org/10.1038/NCLIMATE3303, 2017.

Shepard, M. K., Campbell, B. A., Bulmer, M. H., Farr, T. G., Gaddis, L. R., and Plaut, J. J.: The roughness of natural terrain: A planetary and remote sensing perspective, J. Geophys. Res., 106, 32777–32795, https://doi.org/10.1029/2000JE001429, 2001.

Smith, M. W.: Roughness in the Earth Sciences, Earth-Science Rev., 136, 202–225, https://doi.org/10.1016/j.earscirev.2014.05.016, 2014.

Sovilla, B., Sonatore, I., Bühler, Y., and Margreth, S.: Wet-snow avalanche interaction with a deflecting dam: field observations and numerical simulations in a case study, Nat. Hazards Earth Syst. Sci., 12, 1407–1423, https://doi.org/10.5194/nhess-12-1407-2012, 2012.

Stambaugh, M. C. and Guyette, R. P.: Predicting spatio-temporal variability in fire return intervals using a topographic roughness index, Forest. Ecol. Manag., 254, 463–473, https://doi.org/10.1016/j.foreco.2007.08.029, 2008.

swisstopo: swissALTI3D – Das hoch aufgelöste Terrainmodell der Schweiz, Swiss Federal Office of Topography, Bern, Switzerland, 2018.

swisstopo: SWISSIMAGE – Das digitale Orthofotomosaik der Schweiz, Swiss Federal Office of Topography, Bern, Switzerland, 2021.

Takahashi, T.: Initiation and flow of various types of debris-flow, in: Debris-flow Hazards Mitigation: Mechanics, Prediction, and Assessment, Proceedings 2nd International Debris-flow hazards mitigation Conference, Taipei, Taiwan, 16–18 August 2000, 15–25, 2000.

Tasser, E. and Tappeiner, U.: Impact of land use changes on mountain vegetation, Appl. Veg. Sci., 5, 173–184, https://doi.org/10.1111/j.1654-109X.2002.tb00547.x, 2002.

Teich, M., Marty, C., Gollut, C., Grêt-Regamey, A., and Bebi, P.: Snow and weather conditions associated with avalanche releases in forests: Rare situations with decreasing trends during the last 41 years, Cold Reg. Sci. Technol., 83, 77–88, https://doi.org/10.1016/j.coldregions.2012.06.007, 2012a.

Teich, M., Bartelt, P., Grĕt-Regamey, A., and Bebi, P.: Snow avalanches in forested terrain: Influence of forest parameters, topography, and avalanche characteristics on runout distance, Arct, Antarct. Alp. Res., 44, 509–519, https://doi.org/10.1657/1938-4246-44.4.509, 2012b.

Teich, M., Techel, F., Caviezel, P., and Bebi, P.: Forecasting forest avalanches: A review of winter 2011/12, Int. Snow Sci. Work., Grenoble Chamonix Mont Blanc, 7–11 October 2013, 324–330, 2013.

Teich, M., Fischer, J.-T., Feistl, T., Bebi, P., Christen, M., and Grêt-Regamey, A.: Computational snow avalanche simulation in forested terrain, Nat. Hazards Earth Syst. Sci., 14, 2233–2248, https://doi.org/10.5194/nhess-14-2233-2014, 2014.

Trevisani, S. and Cavalli, M.: Topography-based flow-directional roughness: potential and challenges, Earth Surf. Dynam., 4, 343–358, https://doi.org/10.5194/esurf-4-343-2016, 2016.

Trevisani, S. and Rocca, M.: MAD: Robust image texture analysis for applications in high resolutiongeomorphometry, Comput. Geosci., 81, 78–92, https://doi.org/10.1016/j.cageo.2015.04.003, 2015.

Veitinger, J. and Sovilla, B.: Linking snow depth to avalanche release area size: measurements from the Vallée de la Sionne field site, Nat. Hazards Earth Syst. Sci., 16, 1953–1965, https://doi.org/10.5194/nhess-16-1953-2016, 2016.

Veitinger, J., Sovilla, B., and Purves, R. S.: Influence of snow depth distribution on surface roughness in alpine terrain: a multi-scale approach, The Cryosphere, 8, 547–569, https://doi.org/10.5194/tc-8-547-2014, 2014.

Vetter, M., Höfle, B., Hollaus, M., Gschöpf, C., Mandlburger, G., Pfeifer, N., and Wagner, W.: Vertical vegetation structure analysis and hydraulic roughness determination using dense ALS point cloud data – a voxel based

approach, in: International Archives of the Photogrammetry, Remote Sensing and Spatial Information Sciences, Volume XXXVIII-5/W12, 2011ISPRS Calgary 2011 Workshop, Calgary, Canada, 29–31 August 2011, 265–270, 2011.

Viero, D. P. and Valipour, M.: Modeling anisotropy in free-surface overland and shallow inundation flows, Adv. Water Resour., 104, 1–14, https://doi.org/10.1016/j.advwatres.2017.03.007, 2017.

Viglietti, D., Letey, S., Motta, R., Maggioni, M., and Freppaz, M.: Snow avalanche release in forest ecosystems: A case study in the Aosta Valley Region (NW-Italy), Cold Reg. Sci. Technol., 64, 167–173, https://doi.org/10.1016/j.coldregions.2010.08.007, 2010.

Waldron, K., Ruel, J. C., and Gauthier, S.: Forest structural attributes after windthrow and consequences of salvage logging, Forest. Ecol. Manag., 289, 28–37, https://doi.org/10.1016/j.foreco.2012.10.006, 2013.

Wang, I. T. and Lee, C. Y.: Influence of slope shape and surface roughness on the moving paths of a single rockfall, World Acad. Sci. Eng. Technol., 65, 1021–1027, https://doi.org/10.5281/zenodo.1059436, 2010.

Wohlgemuth, T., Schwitter, R., Bebi, P., Sutter, F., and Brang, P.: Post-windthrow management in protection forests of the Swiss Alps, Eur. J. Forest. Res., 136, 1029–1040, https://doi.org/10.1007/s10342-017-1031-x, 2017.

Wu, J., Yang, Q., and Li, Y.: Partitioning of terrain features based on roughness, Remote Sens., 10, 1–21, https://doi.org/10.3390/rs10121985, 2018.

Yang, P., Ames, D. P., Fonseca, A., Anderson, D., Shrestha, R., Glenn, N. F., and Cao, Y.: What is the effect of LiDAR-derived DEM resolution on large-scale watershed model results?, Environ. Model. Softw., 58, 48–57, https://doi.org/10.1016/j.envsoft.2014.04.005, 2014.

5 Assessment indices for snow avalanche protection of wind-disturbed forests

Tommaso Baggio[1*], Natalie Brožová[2,3,4], Alexander Bast[2,4], Peter Bebi[2,4], Vincenzo D'Agostino[1]

[1] *Department of Land, Environment, Agriculture and Forestry, University of Padua, Legnaro, Italy*

[2] *Alpine Environment and Natural Hazards, WSL Institute for Snow and Avalanche Research SLF, Davos Dorf, Switzerland*

[3] *Department of Environmental Systems Science, Swiss Federal Institute of Technology (ETH Zurich), Zurich, Switzerland*

[4] *Climate Change, Extremes and Natural Hazards in Alpine Regions Research Center CERC, Davos Dorf, Switzerland*

This chapter is currently under review in the journal *Ecological Engineering*

5.1 Abstract

Windstorms are natural disturbances predicted to increase in frequency in the future, with a consequent increased risk of damage to forests. Such damages change the forest structure and, therefore, their protection capacity. Previous studies analysed post-event conditions and the recovery time of abated forest within study areas <10 ha, not accounting for larger spatial scales. In this study, we propose a new methodology to provide tools for spatial assessment and monitoring of forests affected by windstorms over large areas and previously devoted to protect against snow avalanches. Four indices have been used (vegetation height model, surface roughness, stored volume height and adapted tree parameters) of which the latter two have been specifically developed for this goal. We selected and periodically recorded two windthrow areas using photogrammetric surveys (deriving dense point clouds) to assess the performance of the proposed indices and to investigate the long-term changes in protection effects (Disentis, CH) and the influence of snow cover (Franza, IT). Stored volume height and the adapted tree parameters resulted as being the best indices to capture the forest conditions and standing trees, respectively. The stored volume height was further used to estimate forest protection in the presence of the snow cover, providing hazard assessment against snow avalanches considering the observed snow depth. Analysing the Disentis (CH) area, we concluded that the minimum level of protection capacity occurs ten years after the storm event. After 29 years, the forest protective capacity against natural hazards increased again as the forest recovery slowly proceeded. However, special attention should be paid to gaps between growing trees that may be critical for potential avalanche formation as the wood decays. This study provided new insights into the long-term protection efficiency of windthrow forests, proposing two new indices to spatially assess and monitor their evolution.

Keywords: windthrow; avalanche spatial indices; snow avalanche; forest protection; hazard assessment

5.2 Introduction

Protection forests are forested areas with designated protection against natural hazards (Brang et al., 2001). In the Alpine region, forests protect against different hazards such as snow avalanches, rockfalls, shallow landslides and debris flows (Getzner et al., 2017). They stabilize the soil and reduce surface runoff limiting sediment transport (Chandler et al., 2018; Hegg et al., 2005), and the runout distance of mass flow phenomena (May, 2002; Michelini et al., 2017). Regarding snow avalanches, forests reduce the formation of homogeneous snowpack and potentially weak layers with altered microclimate (Moeser et al., 2015), and stabilize snowpack by tree stems (McClung and Schaerer, 2006). In the case of rockfall, trees and shrubs reduce the runout distance and bounce height of falling rocks (Dorren et al., 2005; Rammer et al., 2015).

However, once protection forests are significantly disturbed, their protective function may decrease or even lower to zero if the forest is completely destroyed (Berger and Rey, 2004). As a result, damaged forests may not provide sufficient protection against successive natural hazards. A study of the remaining post-disturbance protective effects and the time of forest recovery is therefore of fundamental importance to adequately assess the protective function over time. Furthermore, since forest disturbances are expected to increase in the future due to climate change (IPCC, 2021), the interactions between natural hazards and disturbed forests will be a topic of high relevance in mountainous regions (Bebi et al., 2017; Paine et al., 1998). Wildfires, snow avalanches, shallow landslides, insect outbreaks and storms are natural disturbances typical for European forests which may affect extensive areas of protection forests. In particular, storms with critical wind speeds produce severe and extended damage to European forests (Gardiner et al., 2010; Schiesser et al., 1997; Seidl et al., 2014). Such storms have shown an increasing trend in frequency and magnitude in the last decades due to legacies of former land use and climate change (Gardiner et al., 2010; Seidl et al., 2011). A good example is the Vaia storm that occurred in October 2018, and which is considered one of the largest wind disturbances observed on southern side of the European Alps in recent times (Motta et al., 2018).

After a storm event, the fallen trees can provide residual protection against natural hazards (Schönenberger, 2002b). Such protection gradually decreases due to breakage processes and wood decay (Wohlgemuth et al., 2017). Natural regeneration is progressively established during the degradation period, and after a certain period, new trees protect against natural hazards. Between biomass degradation and natural regeneration, a minimum of protection capacity may occur (Wohlgemuth et al., 2017). Identification of the residual protection and its temporal evolution together with the growth of natural regeneration are major processes for hazard evaluation and management of disturbed forests in populated mountain areas. The assessment of residual protection, the time of minimum level of protection and period of forest recovery is particularly significant in the case of protection forests against snow avalanches affected by disturbance. Some studies investigated the avalanche protection of wind-disturbed forest through aerial and field data (Schönenberger et al., 2005; Wohlgemuth et al., 2017). They analysed the damaged trees characteristics

(dislocation of lying trunks, logs stability and stem height above ground) and the regeneration rate (sapling density, species composition and protection efficacy) in a maximum period of 24 years since the windstorm at different sites in the Swiss Alps. Results reported a considerably small number of observed snow avalanches and rockfall events, while a higher frequency of shallow landslides and debris flows have been recorded (Bebi et al., 2019; Wohlgemuth et al., 2017). The reported studies investigated the change of different forest parameters of areas <10 ha, Schönenberger, 2002a).However, a spatial quantification method applicable at a regional scale to assess disturbed forest's temporal development for snow avalanche protection over larger areas is still lacking.

The spatial quantification of windthrow forests is crucial for assessing the protection capacity since the pre-event forests can have different stand characteristics (density, basal area, mean height, species composition etc.). On the other hand, forests with the same characteristics could be affected by storms in different ways depending on the prevailing wind direction and local topography. The resulting irregular surface is characterized by spaces between trees where a variable snow volume could be stored, contributing to snow cover stabilization and avoiding the formation of weak layers and therefore hindering the release of snow avalanches. An index evaluating the spatial distribution and characteristics of the biomass on the ground would be helpful to monitor both the current state of different windthrow areas and their temporal changes. This index should also be appropriate to monitor felled forest in winter conditions (presence of snow cover) and the changing probability of avalanche release in relation to the snow cover. Furthermore, the index should be computed using data available for large areas. Data derived from high-resolution LiDAR scans (Light Detection and Ranging) are becoming more frequent in the last decade, even for large areas (Niculiță, 2020). Different regions of the European Alps are already covered by LiDAR surveys since these are becoming more economically accessible to civil authorities (Doneus and Briese, 2011). The raw product of LiDAR surveys is a point cloud that is commonly processed to deduce digital elevation models (i.e. digital surface or terrain model). Forest elements such as trees, shrubs, lying stems and stumps could be identified and extracted for specific analysis (Burt et al., 2019; Dassot et al., 2011). For areas <10 ha, it is even possible to increase the digital surface model resolution up to a few centimetres adopting the photogrammetric technique (analysis of pictures recorded with unmanned aerial systems, UAVs) (Colomina and Molina, 2014).

Based on the state-of-the-art and gaps in knowledge, the objectives of this research are to: (i) define and select indices to assess the avalanche protection capacity of windthrow areas, (ii) assess the temporal change in protection capacity after a wind disturbance, and (iii) evaluate the snow cover influence on potential avalanche formation conditions in windthrow areas. We investigated two study areas affected by storm disturbance to address the objectives. Temporal changes were observed at a long-term study area Disentis, where high-resolution datasets in several timesteps were available. High-resolution data capturing the topography with and without snow cover at Franza study area allowed the seasonal analysis. Using these datasets, we developed and tested two indices to evaluate temporal and seasonal changes of protection capacity against snow avalanches.

5.3 Material and methods

5.3.1 Study areas

Two study areas were selected to achieve the reported objectives: Disentis and Franza (Figure 5.1). The Disentis area was affected by the storm Vivian in 1990 and surveyed in 1991, 2001, 2009 and 2019, resulting in four high-resolution photogrammetric datasets. We used this time series to analyse the characteristics of the biomass immediately after the storm event and in the next 29 years. The Franza study site was impacted by the storm Vaia in 2018 and was surveyed three times. The resulting photogrammetric datasets consist of two snow-free seasons and one with snow cover. At the Franza study area, we investigated the effect of snow cover smoothing relevant for possible avalanche formation and the short-term changes of biomass on the ground. Using these datasets, we developed and tested two indices to evaluate the temporal and seasonal changes of protection capacity against snow avalanches of forests disturbed by windstorms.

Within each study area, we manually defined plots representing potential release areas (PRAs) for snow avalanches to spatially analyse their temporal evolution and the effect of snow cover on the protection capacity. To identify the PRAs, we used topographical variables as slope, plan curvature, and presence of effective vegetation, using the thresholds from literature. Slope angle was selected in the range of 28−55° (Bühler et al., 2013; Schweizer et al., 2003). We calculated plan curvature to separate concave from convex areas to identify ridges and then split or merge PRAs (Maggioni and Gruber, 2003). In addition, we considered effective vegetation to be 1.5 times higher than the maximum snow cover for a given return period (Saeki and Matsuoka, 1969). Furthermore, the relation between gap width and crown cover density has been evaluated as combination of crown coverage, gap length, and slope angle (Bebi et al., 2021; Frehner et al., 2005; Schneebeli and Bebi, 2004).

Every PRA was analysed with indices assessing: the vegetation height model (VHM), surface roughness, stored volume height and adapted tree parameters (see section 2.2).

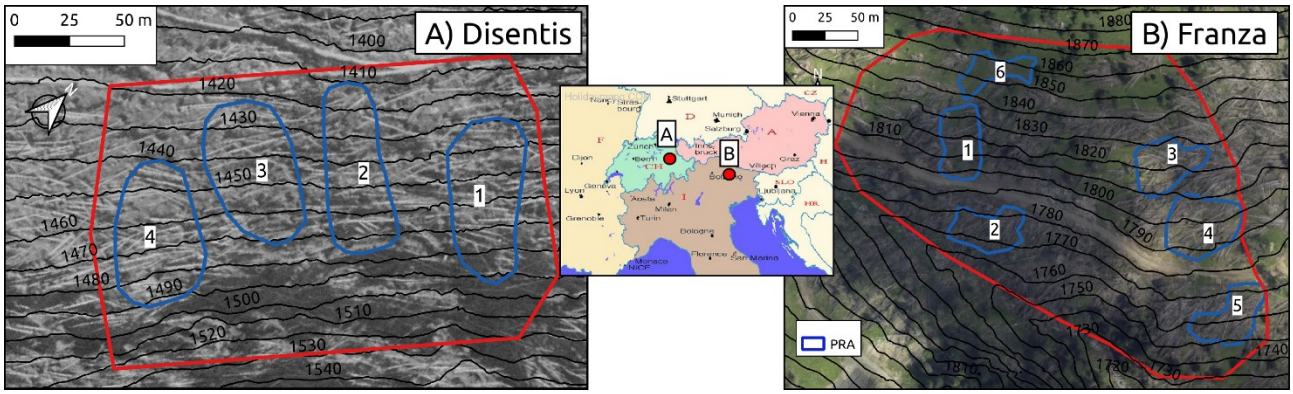

Figure 5.1: Location and aerial images of the two study areas near Disentis (A) and Franza (B). The solid red lines highlight the study sites. The identified potential release areas (PRAs) are outlined in blue. In the background, aerial orthophoto showing the post-event conditions, captured in 1990 and 2019 for Disentis and Franza, respectively. Please note the northing (A).

5.3.1.1 Disentis

The Disentis study area is located in the Swiss Alps, canton Grisons, and it stretches over 2.14 ha. The elevation ranges between 1420 and 1560 m a.s.l, the aspect is north-west, and the slope is inclined between 30° and 50°. The site is in the low-subalpine zone of the Central Alps (Ellenberg and Leuschner, 2010), characterized by a mean annual temperature of 4 °C and mean annual precipitation of 1250 mm (Schönenberger et al., 2005). From a topographical point of view, the area is characterized by different zones of potential release or transit areas of snow avalanches. The Vivian storm occurred in February 1990, severely damaging the site, and affecting all the trees. Two-thirds of the trees were broken, and one third uprooted (Schönenberger, 2002b), and the site remained untouched to provide a monitoring research site (WSL). The pre-storm stand was formed by pure 110−150 years old Norway spruce (*Picea abies*). Full callipering of the study area resulted in 363 stems ha^{-1} and 487 m^3ha^{-1} in 1972. We manually identified four potential release areas within the study site (Figure 5.1A).

Site conditions were recorded by different photogrammetric surveys in 1991, 2001, 2009, and 2019. In 1991, 2001 and 2009 aerial photographs were taken by the Swiss Federal Office of Topography (swisstopo; colour, scale ~1:4'000). Analytical photogrammetry methods were performed by Frey and Thee (2002) and Bebi et al. (2015). The 2019 survey was recorded using a Mavic 2 Pro with ground control points (GCP) acquired with a Stonex GNSS, and pictures were processed with Agisoft Metashape software (Agisoft LLC, St Petersburg, Russia). The derived dense point clouds and digital surface models (DSM) were the input data for the following analyses (for specific information, see Table 5.1). The Digital Terrain Model (DTM) was acquired by a LiDAR survey in 2019 from the Swiss Federal Office of Topography with the resolution of 0.5 m (swisstopo).

5.3.1.2 Franza

The Franza study area is located in the Dolomites, Veneto Region, Italy (Figure 5.1B). The elevation ranges between 1650 and 1950 m a.s.l. facing southwest. The site in the subalpine zone of the Eastern Alps, is characterized by a mean annual temperature of 5 °C and a mean annual precipitation of 1100 mm (Barbi et al., 2013). The site covers 4.24 ha, and the slope inclination is between 25°−40°. The storm Vaia severely hit the area in October 2018, destroying most of the forest stand (mainly by uprooting). The site was not involved in the forest management operation, and the fallen trees were left on the ground. However, the road was cleared from biomass. Around 5–10% of the original forest cover was not damaged. Meadows and young open forests cover the northern part of the area, not affected by the storm. The disturbed forest was dominated by Norway spruce (*Picea abies*) with admixed silver fir (*Abies alba*) and European larch (*Larix decidua*), which was the only tree species resisting the storm.

We captured the site conditions in 2019 and twice in 2020 with three drone flights. The derived dense point clouds and the digital surface models (DSM) served as input data for our following analyses (for specific information, see Table 5.1). Drone images were processed with the image processing software Agisoft Metashape (Agisoft LLC, St Petersburg, Russia). Ground control points were measured with a Topcon

HiPer V GNSS while images were captured with a Dji Phantom 4 drone. Regarding the DTM, it was acquired by the Veneto Region in July 2019 with a LiDAR survey.

Table 5.1: Technical information of the photogrammetric surveys involving the Franza and Disentis study areas. The DTM (digital terrain model derived through LiDAR campaigns). GCP stands for ground control point, DSM for digital surface model and DTM for digital terrain model.

Study area	*Date*	*GCP (n°)*	*GCP accuracy (x,y,z residual error, [m])*	*Point density [n° m^{-2}]*	*DSM resolution [m]*	*DTM (LiDAR) date, resolution [m]*
Disentis (CH)	21/08/1991	*NA*	*NA*	22.5	0.20	2019, 0.50
	10/05/2001	*NA*	*NA*	22.5	0.20	2019, 0.50
	17/08/2009	*NA*	*NA*	22.5	0.20	2019, 0.50
	18/06/2019	10	0.147	680.2	0.10	2019, 0.50
Franza (IT)	26/10/2019	12	0.037	557.3	0.05	2019, 0.50
	29/10/2020	15	0.044	1500	0.05	2019, 0.50
	18/12/2020	11	0.103	1410	0.10	2019, 0.50

5.3.2 Indices

We analysed the identified potential release areas with four different indices to assess the forest protection capacity over time and evaluate the snow cover effect. Vegetation height models (*VHM*) and surface roughness models (*SR*) are common indices to study the height of the biomass concerning ground and surface variability within a specific moving window, respectively (Grohmann et al., 2011). To improve the characterisation of windthrow areas, we developed the stored volume height (*SVH*) index and the adapted tree parameters (*ATP*). We used the reported datasets to test the efficiency of the proposed indices and, at the same time, investigate the temporal evolution of windthrow areas and the effect of snow cover.

5.3.2.1 Vegetation height model (VHM)

The *vegetation height model* (*VHM*) was calculated as the difference between DSM and DTM. For each area, we used the same DTM (derived from the LiDAR survey) since no topographical changes like mass movements were observed within the identified PRAs. To calculate the *VHM* for every survey, we used DSMs derived from each photogrammetric survey to capture the changing surface. The adopted DSM resolution is reported in Table 5.1, while the DTM resolution was interpolated from the original value of 0.5 m to the DSM resolution adopting a bicubic method (Brovelli et al., 2004). We then extracted the cell values within every identified PRAs. To accurately analyse the developments in vegetation height, we performed the *VHM* analysis for the Disentis study area only because of the availability of a long time series (29 years). Identification of the canopy height was not possible using the photogrammetric technique in winter conditions, so it was not performed at the Franza site.

5.3.2.2 Surface roughness (SR)

We further tested the performance of the *surface roughness* (*SR*) to detect the change of windthrow areas over time and with the presence of snow cover. We used the algorithm Vector Ruggedness Measure

(Sappington et al., 2007) to compute *surface roughness*. The input data was the photogrammetric-derived DSM. The resolution and moving window size were 1 m and 7×7, respectively (Brožová et al., 2021). We resampled the DSM with a mean value method to obtain the desired resolution. The resulting raster map was analysed, extracting the cell values within the identified PRAs.

5.3.2.3 Stored volume height (SVH)

The *stored volume height* index (*SVH*) was based on the calculation of the volume between two layers. We used the high-resolution DSM as the first layer and the second one was derived using the highest point of the original DSM to smooth the original surface. The final map conceptually represented a good proxy for the necessary volume of snow required to fill the rough surface (resulting from the felled trees) to obtain an entirely smooth surface. We derived the volume for a given PRA, and calculated a normalized height (*SVH*) by dividing the volume by the area.

We report the algorithm to compute *SVH* in a flowchart (Figure 5.2). We used the functions implemented in the "lidR" package (Roussel et al., 2020) to analyse and process point clouds in R (R Core Team, 2021). First, the outliers were removed, using the Statistical Outliers Algorithm SOR (Rusu and Cousins, 2011), with the number of neighbours equal to 8 and multiplier equal to 3. Next, we classified the dense cloud (photogrammetrically derived) into two classes: high vegetation (represented by trees and their crowns) and the rest (product 1 in Figure 5.2). We used the Cloth Simulation Filtering algorithm (Zhang et al., 2016) to separate the two classes using a cloth resolution of 0.5 m, a classification threshold of 3.0 m and activating the steep slope function. We removed the points from the point cloud classified as high vegetation, and calculated a DSM with a cell resolution of 0.5 m taking the maximum elevation value within the grid cell (product 2 in Figure 5.2). The algorithm then computed the difference between the DSM and DTM, obtaining the low vegetation height model (LVHM, product 3). From this layer, we calculated a smooth surface (product 5 in Figure 5.2), firstly resampling the LVHM to a resolution of 2.5 m (method: highest value, product 4) and then interpolating it to the original resolution of 0.5 m (method: bilinear). Finally, we computed the smooth difference as the difference between the smooth surface and the LVHM (product 6). Summing up the values of the smooth difference layer within a PRA, we calculated the volume necessary to smooth the original surface (product 7 in Figure 5.2). Then, by dividing the volume for the PRA extension, we calculated the *SVH*. *SVH* can be considered as the mean value of snow height necessary to fill the irregular surface of a given PRA. The presented algorithm was implemented in R language (Baggio, 2021) and it is freely available.

The algorithm removed points representing high vegetation to avoid extreme values of the smoothed difference surrounding standing trees. If the points had not been removed, the *SV* for a given PRA would result in an excessive value. The *stored volume height* approach was designed to assess the irregularity of the biomass felled by the storm, not including higher vegetation.

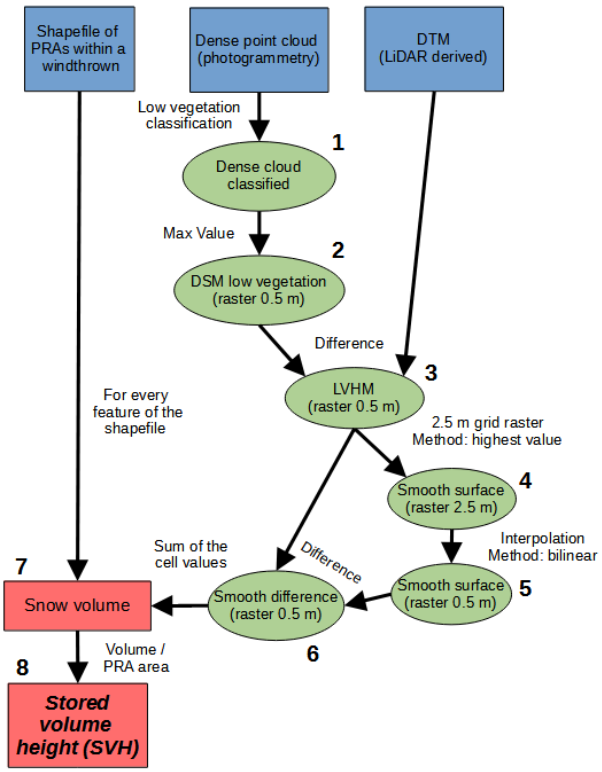

Figure 5.2: Flowchart of the stored volume height algorithm: blue polygons represent input data; the raster or point cloud data are in green; numeric values are in red. DTM stands for digital terrain model.

5.3.2.4 Adapted tree parameters (ATP)

For the identified PRAs at the Disentis site, we analysed the forest parameters of tree density and crown cover. The tree and crown identification algorithm was implemented in R (R Core Team, 2021) using the functions of the "lidR" package (Roussel et al., 2020). The input data were the dense point cloud and LiDAR-derived DTM. We first removed the outlier points with the SOR function (Rusu and Cousins, 2011) and then normalized the point cloud with the DTM. We identified the treetops using the *lmf* algorithm (Popescu and Wynne, 2004) based on a local maximum filter. We applied a circular fixed moving window of 7×7 m, and the height threshold for tree segmentation equal to 1.5 times the maximum snow depth (the calculated 30 years return period maximum snow depth in Disentis was 2.50 m (Frey and Thee, 2002). We identified the crown area based on the Silva et al. (2016) algorithm, adopting default parameters. In such a way, the identified tree height was referred to the ground level. In the case of windthrow areas, we assumed that snow accumulates on the fallen biomass layer and not directly on the ground. Therefore, the height of a standing tree should be referred to the height of the biomass on the ground. For this reason, we delineated a circular buffer area around every identified tree crown of 4 m. We calculated the mean height with respect to the ground for each of these buffer areas (equal to the biomass height above the ground, $H_{ground\ biomass}$, Figure 5.3B). The corrected tree height ($H_{tree\ corrected}$) was the difference between the original height with respect to ground level (H_{tree}) and the mean height of the fallen biomass surrounding the tree ($H_{ground\ biomass}$),

as shown in Figure 5.3B. Finally, we considered tree presence within a given PRA, if $H_{tree\ corrected}$ resulted greater than 1.5 times the maximum snow depth in a return period of 30 years. Dividing the number of trees and total crown area by the relative PRA extent, we obtained the tree density and cover percentage, respectively. The algorithm to derive the reported *adapted tree parameters* from a point cloud was implemented in R language (Baggio, 2021) and it is freely available.

Furthermore, we assessed the presence of critical gaps within the forest cover as a potential cause of snow avalanche release areas. The gap length was evaluated within the identified PRAs along the maximum slope. We adopted the thresholds reported in Schneebeli and Bebi (2004) for the critical gap identification (Figure 5.3A). The delineation was based on a function between gap length and crown cover density for different classes of slope steepness.

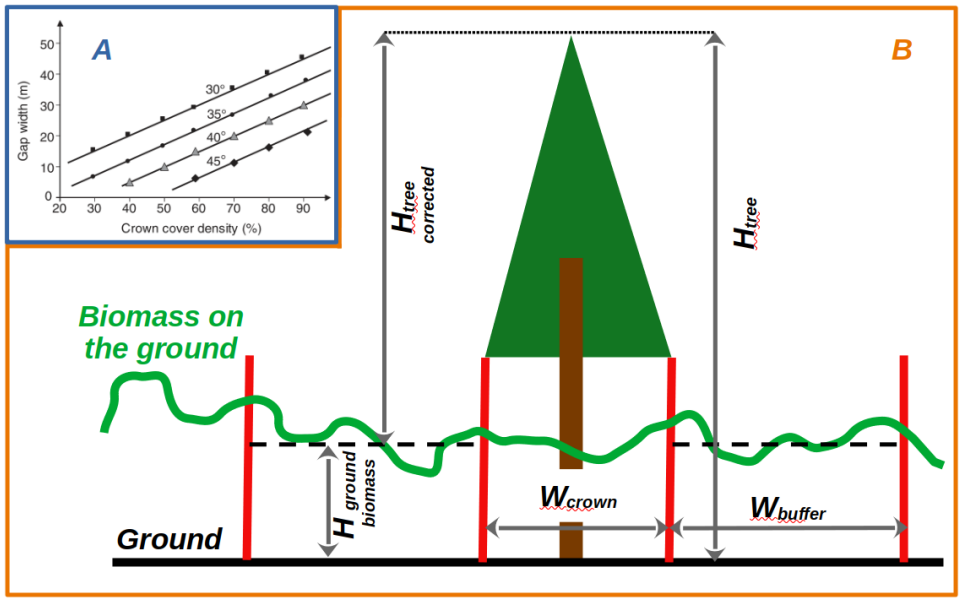

Figure 5.3: A) Relations between gap width and crown cover density for critical gap identification (source: Schneebeli and Bebi, 2004). B) Sketch of a standing tree in a windthrow area with the reported measures used to improve the calculation of tree height in accordance with the biomass on the ground.

5.3.3 Additional analysis

To accurately assess the performance of the *SVH* index and the variation in biomass height we computed for the Franza study area, the DEM of Difference (DoD). DoD is the difference between two elevation models, and in this case, we used two DSM maps without snow cover. To accurately compute the DoD map, we adopted the minimum level of detection method (Brasington et al., 2003) estimated as the DoD error. The DoD error results from the following equation $\delta u_{DoD} = \sqrt{\delta u_1^2 + \delta u_2^2}$, where δu_1 and δu_2 are the errors of the photogrammetric derived surveys. The errors associated to every survey are reported in Table 5.1.

During the photogrammetric survey of the Franza area on the 18th December 2020, we measured the height of the snow cover. The height was measured perpendicular to the surface using a ruler. We collected six

measurements in different locations of the study area, characterized by the absence of felled trees. We surveyed five values for every measurement: four at the vertices of an imaginary square with 1 m sides and one in the middle. The five values were averaged to derive a single measurement for the given location.

To estimate the necessary amount of snow to smooth the irregular surface created by the biomass on the ground, we fitted a linear model between snow depth and the values of *SVH* observed in October 2020 and December 2020 for the Franza study area. The objective of the analysis was to extrapolate a threshold in snow depth for which the *SVH* values observed in October 2020 for PRA 1-5 (windthrow areas) lowered towards the *SVH* of PRA 6 (meadow area, Figure 5.1B).

5.4 Results

5.4.1 Temporal change: Disentis

We observed a temporal change in forest protection capacity during 29 years at the Disentis site by using all four indices: *vegetation height model (VHM)*, *surface roughness (SR)*, *stored volume height (SVH)* and *adapted tree parameters (ATP)*. Similar trends were noticed when using the three indices (*VHM*, *SR* and *SVH*) with an observed minimum in 2001 (Figure 5.4). However, the *adapted tree parameters* index showed a minimum one year after the disturbance in 1991 (Figure 5.4 and Figure 5.5). According to the *ATP,* there were almost no trees one year after the disturbance (Table 5.2). Furthermore, it is important to observe the variability between the identified PRAs in 1991 for the three indices reported in Figure 5.4. The mean *VHM* ranged between 1.41 and 2.50 m, the mean *SR* between 0.116 and 0.198 and the *SVH* index between 0.735 and 0.973 m.

Nineteen years after the storm event, all the indices (*VHM*, *SR*, *SVH* and *ATP*) showed an increase with greater values compared to the first survey (immediately after the disturbance). In 2009, there were some trees up to 14 m in height. However, variability between different PRAs was observed and particularly PRA 3 had only a few trees (Figure 5.5 and Table 5.2).

For the fourth survey (in 2019), *surface roughness* and *stored volume height* slightly increased compared to the previous years. The only exception involved the *surface roughness* of PRA 1, which showed a decreasing trend in the last nine years. The *stored volume height* values resulted similar between the four PRAs, while *surface roughness* values showed a higher variability. Instead, *VHM* showed a constantly increasing trend since the minimum observed in 2001. However, the increase of *VHM* values at PRA 3 resulted in lower than the other PRAs. Similarly, the index *ATP* showed an increasing number of trees with some variability per PRA, with the fewest trees in PRA 2 (Figure 5.5 and Table 5.2).

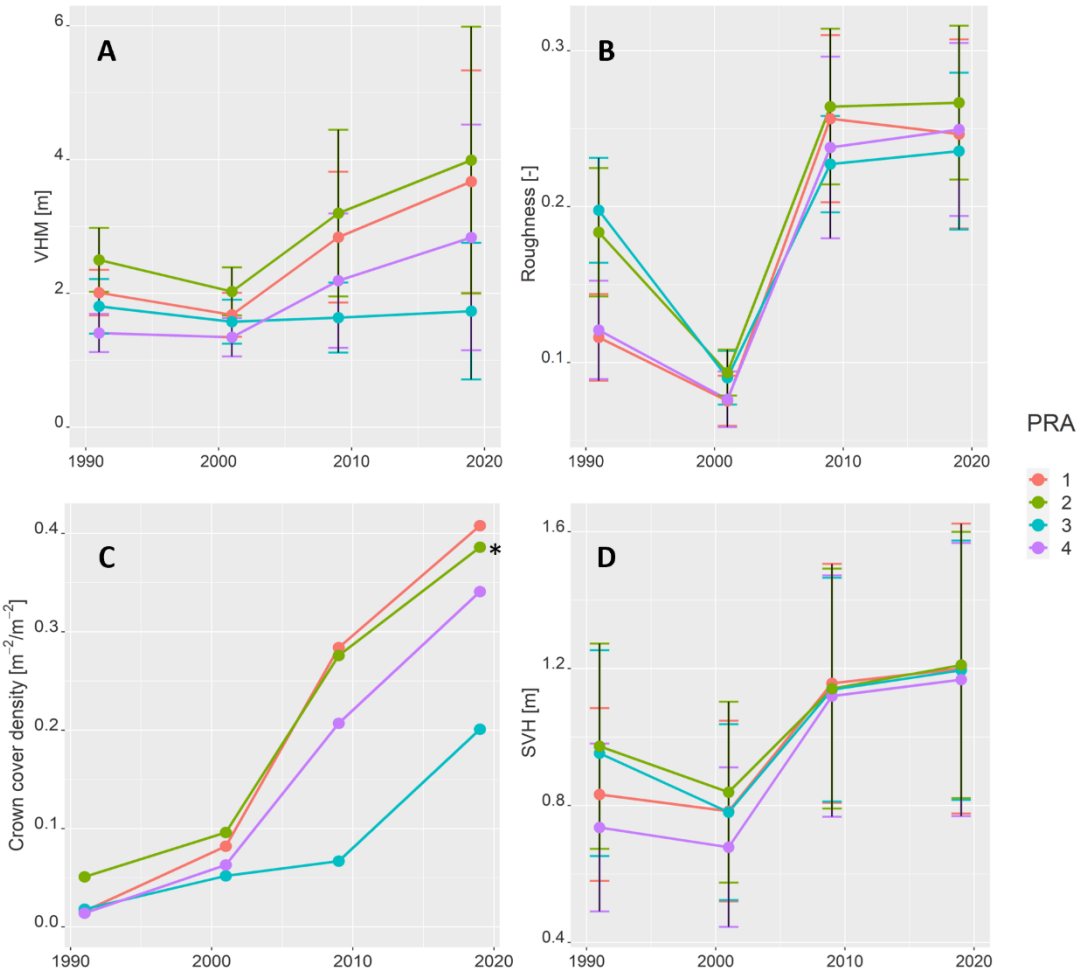

*Figure 5.4: Plots showing the mean value of the four investigated indices for every PRA and photogrammetric survey of the Disentis study site: (A) Vegetation height model (VHM), (B) surface roughness, (C) crown cover density, and (D) stored volume height. The locations of the PRAs are reported in Figure 5.1. The symbol * in the (C) plot means the absence of critical gaps as defined in Schneebeli and Bebi (2004).*

Table 5.2: Tree density per potential release areas PRA and date of photogrammetric survey of the Disentis study area.

	Tree density [n°/ha]			
PRA	1991	2001	2009	2019
1	4.8	38.3	76.6	71.8
2	15.5	51.6	56.8	51.6
3	4.6	27.5	32.1	64.1
4	4.7	37.7	51.8	70.7

Regarding the *adapted tree parameters*, the analysis showed 1 to 3 standing trees per PRA immediately after the storm (in 1991), while crown cover density was between1.6–5.1%. The trends of the number of trees and crown cover increased over time for all the PRAs. Instead, PRA 1 and 2 showed a slight decreasing trend of tree density between 2009 and 2019 (Table 5.2). The major increment of tree density occurred between 1991and 2001 (Table 5.2) and for the crown cover density between 2001 and 2009 (Figure 5.4C). In 2019 (29 years after the storm), the mean tree density of the four PRAs resulted as 64.5 trees ha^{-1} and the crown cover density as 33.4%. These vary between 20.1 trees ha^{-1} and 20.7% regarding the tree and crown cover density, respectively. Twenty-nine years after the storm, we identified the presence of critical gaps (section 2.2.4) in three PRAs (PRA 1, 3 and 4), which might be prone to avalanche formation. Only PRA 2 showed a full recovery without critical gaps in 2019 (Figure 5.4). The identified PRAs showed different recovery patterns in forest protection capacity even if the pre-event conditions were similar.

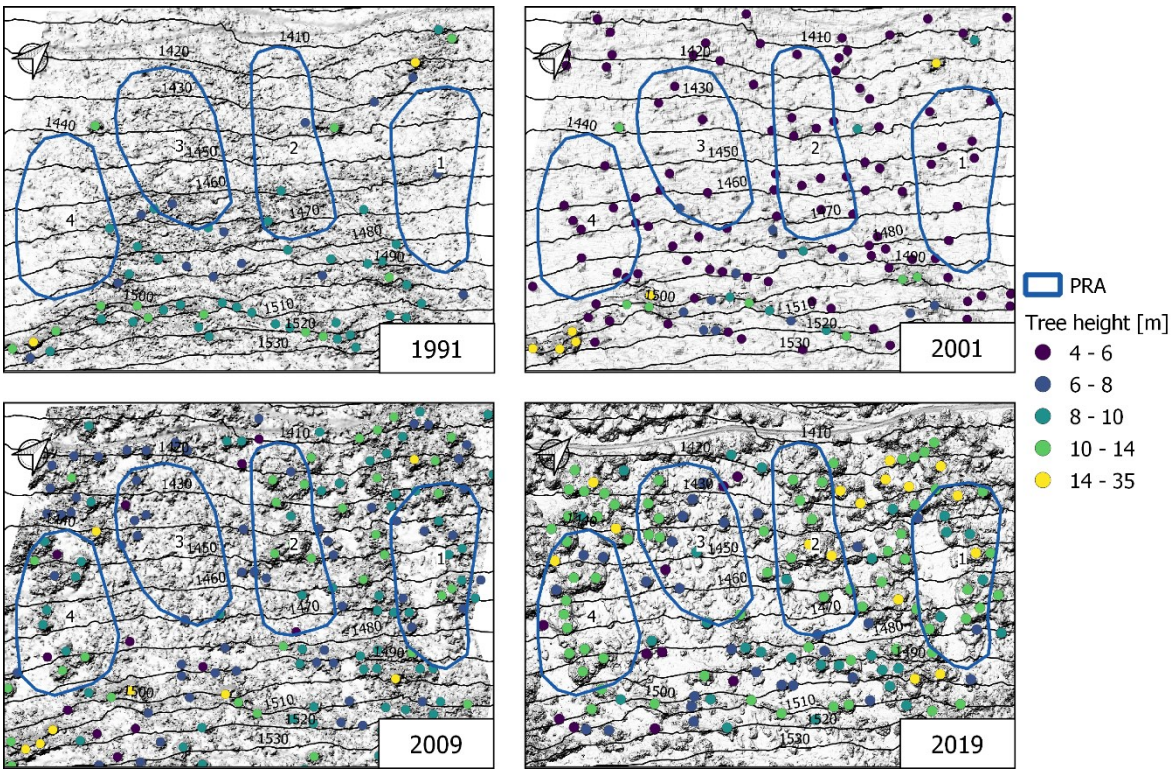

Figure 5.5: Maps of the calculated tree positions at the Disentis study site, based on the algorithm "adapted tree parameters" described in section 2.2.4, for the years 1991, 2001, 2009, and 2019. The different coloured dots represent the tree height [m] with respect to the ground level. In the background, we plotted the hillshade view of the DSM photogrammetry-derived survey. The elevation difference between contour lines is 10 m. The solid blue lines depict the PRAs.

5.4.2 Snow influence and short temporal change: Franza

In Franza study area, the values for *surface roughness* and *stored volume height* differed depending on the date of the data acquisition (Figure 5.6). The difference between October 2019 and October 2020 (both surveys without snow cover) showed a decreasing trend in *surface roughness*. On the contrary, the *stored volume height* showed an increased between the same dates, except for PRA 2 (Figure 5.6B).

From the DoD map of PRA 3 (Figure 5.7), we could visually assess that most of the stems did not move during the 2019/2020 winter season (difference between the DSM acquired in October 2019 and October 2020). However, the fine biomass, as needles and small branches, broke down, thus reducing the elevation values as identifiable from the crowns of felled trees (Figure 5.7). This process resulted in new spaces between logs that slightly increased the amount of snow required to smooth the irregular surface. This process was captured by the *SVH* (increasing trend), while the *SR* did not capture the change in stem structure (decreasing trend, Figure 5.6A).

SVH and *SR*, calculated in December 2020 with snow cover, resulted lower than the previous survey without snow cover (October 2021). The snow depth measured the same day as the photogrammetric survey was 0.85 m (mean of six measurements taken in different locations of the study area). Considering the snow cover, the *stored volume height* of PRA 1-5 surveyed in December 2020 (mean value of 0.68 m) resulted higher than the grassland control area of PRA 6 (equal to 0.15 m). The mean percentage decrease of stored volume in the PRAs (excluding PRA 6) was 18% (with a range of 14 – 25%). Hypothesizing a decreasing linear trend of the *SVH* index as a function of snow depth, we derived a linear model using the *SVH* values recorded in October 2020 and December 2019 for PRA 1-5, obtaining a coefficient of -0.18 per meter of snow. Adopting the fitted model to estimate the snow depth necessary to decrease the *SVH* of PRA 1-5 toward the mean *SVH* value of PRA 6 (recorded in October 2020), we calculated a value of 3.35 m. This value may represent the snow depth necessary to smooth the rough surface generated by the biomass on the ground for which snow avalanches may be released.

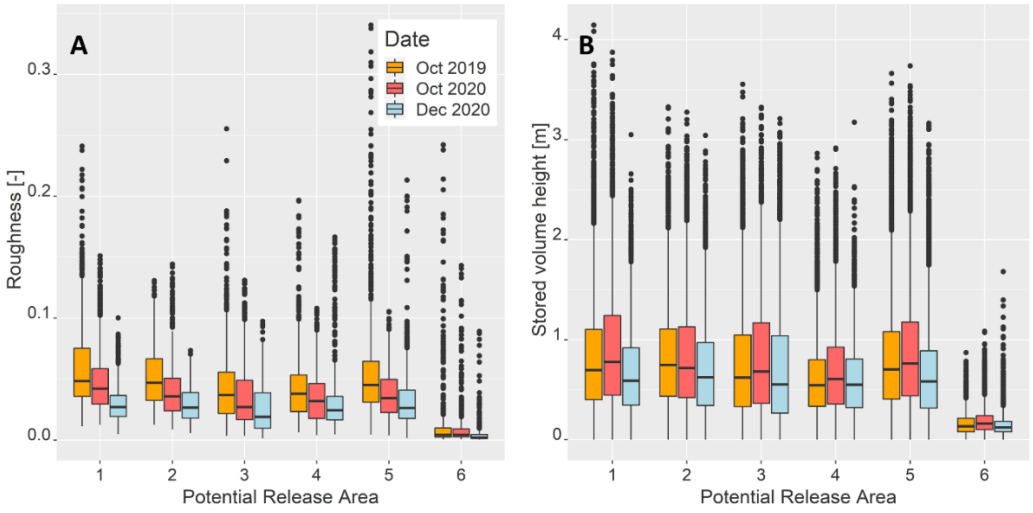

Figure 5.6: raster point analysis of potential release areas (PRAs) of the Franza site for surface roughness (SR) (A) and stored volume height (SVH) (B).

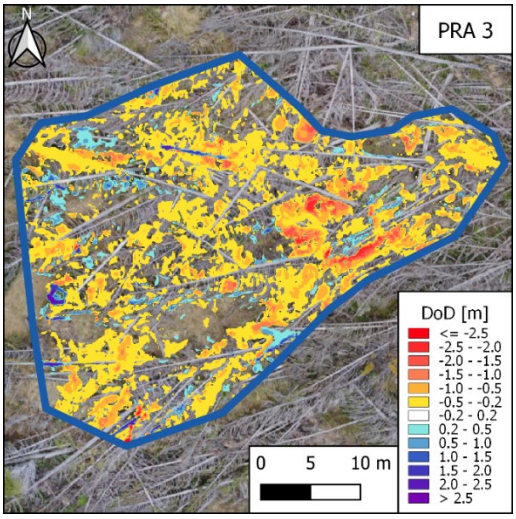

Figure 5.7: Digital elevation model of Difference (DoD) map of the potential release area 3 (PRA 3) within the Franza study area. PRA location is shown in Figure 5.1B.

5.5 Discussion

5.5.1 Indices

The protection capacity of forests affected by storm events in terms of temporal development and snow cover influence was assessed using four indices. The *stored volume height* index, representing snow volume needed to fill the space to create a smooth surface, resulted suitable to investigate both the temporal change and the effect of snow cover of areas affected by wind disturbance. The index performed a direct spatial estimation of the volume left by trees and crowns on the ground, examining the difference between the original DSM and a smoothed DSM. Moreover, *SVH* did not consider trees above a certain height in order to not deviate the estimation of the dominant fallen biomass. The *stored volume height* index resulted in more suitable with respect to *surface roughness* estimating forest protection against snow avalanches after a disturbance. This finding is supported by the results from the Franza study area results, where the breakage process increased the free volume between the tree stems (Figure 5.7). The *stored volume height* captured this aspect as observed by the increasing trend between the surveys of October 2019 and October 2020 (Figure 5.6B).

Regarding the *adapted tree parameters*, we developed an automatic procedure to identify standing trees and extract the related crown area and tree density. The procedure identifies trees emerging from a certain threshold above the mean height of the biomass surrounding the target tree. Thanks to the availability of LiDAR data, different algorithms have been developed in the last years to automatically identify and segment trees (Burt et al., 2019; Popescu and Wynne, 2004). The common reference surface for tree height estimation is the ground, usually derived from the last return of the laser signal (Mkaouar et al., 2018). This approach is appropriate for biomass estimation or growth rate calculation (Qi et al., 2019; Zhao et al., 2018). Differently, the reference surface for snow avalanches should be at the point of avalanche formation. In the

case of windthrow areas, the reference surface is expected to be above the biomass layer deposited on the ground, where weak layers may develop (Schweizer et al., 2003). In this sense, the proposed *ATP* index (Figure 5.3) satisfactorily identifies trees emerging from the reference surface for snow avalanches considering only the trees that potentially provide an effective protection.

5.5.2 Temporal change

The investigated indices (Figure 5.4), were consistent to assess the minimum level of forest protection capacity in Disentis in 2001, 11 years after the storm event. Already 19 years after the storm (in 2009), the protection capacity resulted higher than one year after the event, and it further increased 29 years later (the performed analyses were in accordance as shown in Figure 5.4). The increase in forest protection identified by the adopted indices after the 2001 survey is mainly due to the growth of shrubs and young trees, as observed in the study of Wohlgemuth et al. (2017). Regarding the growing forest, the tree and crown cover density are crucial indices for assessing forest protection and identifying gaps (Frehner et al., 2005; Schneebeli and Bebi, 2004). Therefore, the trees are identified only if their height exceeds a threshold value with respect to the surrounding surface (Figure 5.3B). Analysing values of the *adapted tree parameter* (Figure 5.5), we found one PRA (from the total of four), showing no critical gaps 29 years after the disturbance according to the thresholds reported by Frehner et al. (2005). However, the extent of the original PRAs was reduced by the forest cover 19 years after the storm and further in the following 10 years. Consequently, the extent of PRAs and the related avalanche volume decreased with time after disturbance. Accordingly, Teich et al. (2014) highlighted the increase of small snow avalanches stopping within sparse/young forests. Furthermore, even a slow forest recovery contributed to forest protection capacity in stabilizing the snowpack to some extent. In general, a few small gaps could be found between young trees, which might be prone to avalanche formation. The identification and evaluation of such small gaps and forest parameters are of great interest in order to reliably simulate possible snow avalanches (Brožová et al., 2020). Evaluation of the low vegetation merits particular attention, which does not always provide an adequate protection on steep slopes as it might be compressed by the snow cover (Feistl et al., 2014). Nevertheless, no avalanches were observed in the uncleared windthrow study area of Disentis (Wohlgemuth et al., 2017), even with a cumulated snow cover depth of 1.65 m during the 1998/1999 winter season (Frey and Thee, 2002).

Regarding the short-term temporal changes at the Franza site, the DoD map (Figure 5.7) showed that most of the fine biomass (needles and small branches) fell on the ground or broke (Radtke et al., 2009), leaving more space to store the snow between the lying stems and consequently increasing the snowpack stability. In this case, the protection capacity against snow avalanches slightly increased two years after the windstorm compared to one year after. However, such a small increase in protection capacity is expected to rapidly decrease within the next ten years, as observed at the Disentis study area.

5.5.3 Snow cover

Regarding the influence of snow on terrain smoothing, we obtained promising results investigating the *stored volume height* with and without snow cover. The index decreased for every PRA compared to the absence of snow. However, the *SVH* values of PRA affected by windthrow were noticeably higher than a smooth PRA, meaning that more snow could be accumulated without the risk of releasing an avalanche (for the December 2020 survey of the Franza site). After the storm event at Franza, the abated protection forest showed a good function in storing and supporting snow cover, considering the snow depth and *stored volume height* values observed in winter conditions. The protection is expected to be sufficient also with a snow depth greater than that of the December 2020 survey (0.85 m measured on meadow next to the forest). The extrapolation of the fitted linear model calculated a snow depth value of 3.35 m necessary to smooth the observed surface of windthrow areas toward the same level as meadow areas. This value of snow depth is expected to reduce over the years due to *SVH* decrease as observed for the Disentis area, where the minimum was observed ten years after the storm event. However, the estimation is approximate since the model is based only on one survey representing winter conditions. Additional validations are necessary to correctly establish a robust relationship between snow depth and *stored volume height* to improve the predictability for the potential formation of snow avalanches depending on the snow depth.

5.5.4 Applications and limitations

The investigated study areas Disentis and Franza highlighted the spatial and temporal variation of the protection capacity of windthrow areas concerning snow avalanches. Considering the relatively low intra-site variability of pre-storm forest characteristics and topographical conditions, we observed different values for the tested indices between the PRA at both sites. In Disentis, the differences regarded the natural regeneration of trees (index: *adapted tree parameters*) and the decay of deadwood (index: *stored volume height*). One particular PRA showed a forest cover with no critical gaps 29 years after the event, while for other PRAs the tree growth rate was lower and critical gaps exist. Even if some areas present small gaps, the likelihood of triggering snow avalanches is expected to be low due to the rough surface generated by shrubs and young trees. This example of site variability shows the need for an accurate evaluation of the post-disturbance forest protection capacity. For this purpose, the study reports a new spatially distributed index to evaluate the residual protection capacity of forests (*SVH*) affected by storms together with an algorithm to automatically identify the presence of remaining or new trees (and the related crown extent) emerging from the biomass on the ground (*ATP*). The combination of *SVH* and *ATP* improves the knowledge of the dynamics in windthrow areas supporting and integrating previous studies (Bebi et al., 2015; Frey and Thee, 2002; Schönenberger et al., 2005; Wohlgemuth et al., 2017). The indices can potentially be used over large regions covered by LiDAR or photogrammetric surveys. They have the potential to identify areas with lower protection capacity supporting decision-making on the establishment of necessary technical measures. Further studies and control areas are desirable to adequately assess the

indices quality and accuracy, especially considering different forest characteristics such as density, age structure, species composition and disturbance intensity.

The methods reported in this study may also be used to assess protection capacity against rockfall of windthrow forests. Felled trees have a great capacity to influence rockfall runout distance (Olmedo et al., 2015). Lying stems increased *surface roughness*, consequently enlarging the probability of impacting obstacles and decreasing the associated energy (Ringenbach et al., 2021). Moreover, the tree identification algorithm can be used to delineate the characteristics and location of new forested areas. Such data serve as a fundamental input to update rockfall hazard maps in areas impacted by storms in the past, since disturbed forests have great importance in rockfall hazard mitigation (Lingua et al., 2020; Scheidl et al., 2020).

Assessing post-disturbance forest effects against natural hazards is crucial (Bebi et al., 2017). The evaluation of hazard protection in disturbed areas could become difficult due to their extension and the problematic accessibility, as observed in areas affected by disturbances in the Alpine region (e.g. large forested areas disturbed by the Vaia storm in 2018). This study introduces innovative methods to assess and monitor the temporal evolution of forest protection capacity affected by a disturbance event. Such methods can be directly applied to evaluate the post-disturbance forest protection capacity even on large areas, since the required input data is the point cloud derivable from LiDAR or photogrammetric surveys. Consequently, civil authorities could quickly define post-disturbance forest protection capacity over large areas, identifying sites with lower protection capacity requiring immediate management. The described methods can be further used to compute different management scenarios in a spatial-temporal framework to derive the most promising option. The analysis can be used to investigate the consequences of recent disturbances (storm Vaia 2018, Chirici et al., 2019) and monitor the temporal evolution of past disturbances (Quine and Bell, 1998) for immediate management of hazard areas.

5.6 Conclusions

The study investigated the protection capacity of windthrow forests thanks to two study areas in the European Alps (Disentis, Switzerland and Franza, Italy) recorded by high-resolution photogrammetric surveys. We assessed the performance of four indices in characterising the temporal evolution of windthrow areas and the smoothing effect of snow cover. The *stored volume height* and the *adapted tree parameters* resulted as being the best indices to assess and monitor the protection capacity of forests affected by windstorms. In particular, the *stored volume height* performed well in characterising the effect of snow cover on the biomass on the ground. The combination of *stored volume height* and *adapted tree parameters* allows analysing the characteristic of the biomass on the ground, the remaining standing trees and the development of natural regeneration. Regarding the temporal evolution, the minimum level of protection capacity was observed around ten years after the disturbance when the protective effect of the biomass on the ground was at a minimum, and natural regeneration was not yet sufficiently developed. Twenty-nine years after the disturbance the trees reduced the PRA area extent and fragmented the original PRA,

decreasing the potential size and effects of possible snow avalanches. The indices presented in this study can be used at a regional scale to spatially assess and monitor forest conditions affected by windthrow, improving the management of the most critical areas over time.

Acknowledgements

This research received funding as part of the project "Bridging the mass-flow modelling with the reality", from the CARIPARO foundation (2724/2018). This work was partly funded by the WSL research program Climate Change Impacts on Alpine Mass Movements – CCAMM (ccamm.slf.ch). The authors wish to thank Lorenzo Martini (TESAF Department) for performing the three drone flight surveys of the Franza study area.

Research data

The codes to compute the stored volume height and the adapted tree are available at the following link: https://github.com/TommBagg/Wind-disturbed_forest_analysis/releases/tag/WDFA_v1.0 (last access 12 December 2021), DOI: https://doi.org/10.5281/zenodo.5771996, Baggio, 2021.

Data are available from the corresponding author on request.

5.7 References

Allan, R.P., Hawkins, E., Bellouin, N., Collins, B., 2021. IPCC, 2021: Summary for Policymakers.

Baggio, T., 2021. Wind-disturbed_forest_analysis_v1.0 [code]. https://doi.org/10.5281/zenodo.5771996

Barbi, A., Checchetto, F., Delillo, I., Rech, F., 2013. Le precipitazioni sul Veneto-Valori annuali.

Bebi, P., Bast, A., Ginzler, C., Rickli, C., Schöngrundner, K., Graf, F., 2019. Waldentwicklung und flachgründige Rutschungen: eine grossflächige GIS-Analyse. Schweizerische Zeitschrift fur Forstwes. 170, 318–325. https://doi.org/10.3188/szf.2019.0318

Bebi, P., Bast, A., Helzel, K., Schmucki, G., Brozova, N., Bühler, Y., 2021. Avalanche protection forest: from process knowledge to interactive maps, in: IntechOpen. https://doi.org/10.5772/intechopen.99514

Bebi, P., Putallaz, J.M., Fankhauser, M., Schmid, U., Schwitter, R., Gerber, W., 2015. Die Schutzfunktion in Windwurfflächen. Schweizerische Zeitschrift fur Forstwes. 166, 168–176. https://doi.org/10.3188/szf.2015.0168

Bebi, P., Seidl, R., Motta, R., Fuhr, M., Firm, D., Krumm, F., Conedera, M., Ginzler, C., Wohlgemuth, T., Kulakowski, D., 2017. Changes of forest cover and disturbance regimes in the mountain forests of the Alps. For. Ecol. Manage. 388, 43–56. https://doi.org/10.1016/j.foreco.2016.10.028

Berger, F., Rey, F., 2004. Mountain protection forests against natural hazards and risks: New french developments by integrating forests in risk zoning. Nat. Hazards 33, 395–404. https://doi.org/10.1023/B:NHAZ.0000048468.67886.e5

Brang, P., Schönenberger, W., Ott, E., Gardner, B., 2001. Forests as Protection from Natural Hazards, in: The Forests Handbook. Wiley-Blackwell Publishing Ltd, pp. 53–81. https://doi.org/10.1002/9780470757079.ch3

Brasington, J., Langham, J., Rumsby, B., 2003. Methodological sensitivity of morphometric estimates of coarse fluvial sediment transport. Geomorphology 53, 299–316. https://doi.org/10.1016/S0169-555X(02)00320-3

Brovelli, M.A., Cannata, M., Longoni, U.M., 2004. LIDAR Data Filtering and DTM Interpolation Within GRASS. Trans. GIS 8, 155–174. https://doi.org/10.1111/j.1467-9671.2004.00173.x

Brožová, N., Baggio, T., D'Agostino, V., Bühler, Y., Bebi, P., 2021. Multiscale analysis of surface roughness for the improvement of natural hazard modelling. Nat. Hazards Earth Syst. Sci. 21, 3539–3562. https://doi.org/10.5194/nhess-21-3539-2021

Brožová, N., Fischer, J.-T., Bühler, Y., Bartelt, P., Bebi, P., 2020. Determining forest parameters for avalanche simulation using remote sensing data. Cold Reg. Sci. Technol. 172, 102976. https://doi.org/10.1016/j.coldregions.2019.102976

Bühler, Y., Kumar, S., Veitinger, J., Christen, M., Stoffel, A., 2013. Automated identification of potential snow avalanche release areas based on digital elevation models. Nat. Hazards Earth Syst. Sci. 13, 1321–1335. https://doi.org/10.5194/nhess-13-1321-2013

Burt, A., Disney, M., Calders, K., 2019. Extracting individual trees from lidar point clouds using treeseg. Methods Ecol. Evol. 10, 438–445. https://doi.org/10.1111/2041-210X.13121

Chandler, K.R., Stevens, C.J., Binley, A., Keith, A.M., 2018. Influence of tree species and forest land use on soil hydraulic conductivity and implications for surface runoff generation. Geoderma 310, 120–127. https://doi.org/10.1016/j.geoderma.2017.08.011

Chirici, G., Giannetti, F., Travaglini, D., Nocentini, S., Francini, S., D'Amico, G., Calvo, E., Fasolini, D., Broll, M., Maistrelli, F., Tonner, J., Pietrogiovanna, M., Oberlechner, K., Andriolo, A., Comino, R., Faidiga, A., Pasutto, I., Carraro, G., Zen, S., Contarin, F., Alfonsi, L., Wolynski, A., Zanin, M., Gagliano, C., Tonolli, S., Zoanetti, R., Tonetti, R., Cavalli, R., Lingua, E., Pirotti, F., Grigolato, S., Bellingeri, D., Zini, E., Gianelle, D., Dalponte, M., Pompei, E., Stefani, A., Motta, R., Morresi, D., Garbarino, M., Alberti, G., Valdevit, F., Tomelleri, E., Torresani, M., Tonon, G., Marchi, M., Corona, P., Marchetti, M., 2019. Forest damage inventory after the "Vaia" storm in Italy. For. - Riv. di Selvic. ed Ecol. For. 16, 3–9. https://doi.org/10.3832/efor3070-016

Colomina, I., Molina, P., 2014. Unmanned aerial systems for photogrammetry and remote sensing: A review. ISPRS J. Photogramm. Remote Sens. https://doi.org/10.1016/j.isprsjprs.2014.02.013

Dassot, M., Constant, T., Fournier, M., 2011. The use of terrestrial LiDAR technology in forest science: Application fields, benefits and challenges. Ann. For. Sci. 68, 959–974. https://doi.org/10.1007/s13595-011-0102-2

Doneus, M., Briese, C., 2011. Airborne Laser Scanning in forested areas–potential and limitations of an archaeological prospection technique, in: Remote Sensing for Archaeological Heritage …. pp. 59–76.

Dorren, L.K.A., Berger, F., Le Hir, C., Mermin, E., Tardif, P., 2005. Mechanisms, effects and management implications of rockfall in forests. For. Ecol. Manage. 215, 183–195. https://doi.org/10.1016/j.foreco.2005.05.012

Ellenberg, H., Leuschner, C., 2010. Vegetation Mitteleuropas mit den Alpen: in ökologischer, dynamischer und historischer Sicht.

Feistl, T., Bebi, P., Dreier, L., Hanewinkel, M., Bartelt, P., Bebi, P., Dreier, L., Hanewinkel, M., Bartelt, P., 2014. Quantification of basal friction for technical and silvicultural glide-snow avalanche mitigation measures. Nat. Hazards Earth Syst. Sci. 14, 2921–2931. https://doi.org/10.5194/nhess-14-2921-2014

Frehner, M., Wasser, B., Schwitter, R., 2005. Nachhaltigkeit und Erfolgskontrolle im Schutzwald.Wegleitung für Pflegemassnahmen in Wäldern mit Schutzfunktion [Sustainability and controlling in protection forests. Guidelines for tending forests with protective function], in: Bundesamt Für Umwelt,Wald Und Landschaft (BUWAL). Bern, Switzerland, p. 554.

Frey, W., Thee, P., 2002. Avalanche protection of windthrow areas: A ten year comparison of cleared and uncleared starting zones, Forest Snow and Landscape Research.

Gardiner, B., Blennow, K., Carnus, J.-M., Fleischer, P., Ingemarson, F., Landmann, G., Lindner, M., Marzano, M., Nicoll, B., Orazio, C., Peyron, J.-L., Reviron, M.-P., Schelhaas, M.-J., Schuck, A., Spielmann, M., Usbeck, T., 2010. Destructive Storms in European Forests: Past and Forthcoming Impacts.

Getzner, M., Gutheil-Knopp-Kirchwald, G., Kreimer, E., Kirchmeir, H., Huber, M., 2017. Gravitational natural hazards: Valuing the protective function of Alpine forests. For. Policy Econ. 80, 150–159. https://doi.org/10.1016/j.forpol.2017.03.015

Grohmann, C.H., Smith, M.J., Riccomini, C., 2011. Multiscale analysis of topographic surface roughness in the Midland Valley, Scotland. IEEE Trans. Geosci. Remote Sens. 49, 1200–1213. https://doi.org/10.1109/TGRS.2010.2053546

Hegg, C., Badoux, A., Witzig, J., Lueser, P., 2005. Forest influence on flood runoff generation studied on the Sperbelgraben example, in: Progress in Surface and Subsurface Water Studies at Plot and Small Basin Scale. pp. 47–52.

Lingua, E., Bettella, F., Pividori, M., Marzano, R., Garbarino, M., Piras, M., Kobal, M., Berger, F., 2020. The Protective Role of Forests to Reduce Rockfall Risks and Impacts in the Alps Under a Climate Change Perspective, in: Climate Change, Hazards and Adaptation Options. Springer, pp. 333–347. https://doi.org/10.1007/978-3-030-37425-9_18

Maggioni, M., Gruber, U., 2003. The influence of topographic parameters on avalanche release dimension and frequency. Cold Reg. Sci. Technol. 37, 407–419. https://doi.org/10.1016/S0165-232X(03)00080-6

May, C.L., 2002. Debris flows through different forest age classes in the central Oregon Coast Range. J. Am. Water Resour. Assoc. 38(4) 1097-1113.

McClung, D., Schaerer, P., 2006. The avalanche handbook.

Michelini, T., Bettella, F., D'Agostino, V., 2017. Field investigations of the interaction between debris flows and forest vegetation in two Alpine fans. Geomorphology 279, 150–164. https://doi.org/10.1016/j.geomorph.2016.09.029

Mkaouar, A., Kallel, A., Guidara, R., Ben Rabah, Z., 2018. Detection of forest strata volume using LiDAR data, in: 4th International Conference on Advanced Technologies for Signal and Image Processing (ATSIP). IEEE, pp. 1–6. https://doi.org/10.1109/ATSIP.2018.8364496

Moeser, D., Stähli, M., Tobias, J., 2015. Improved snow interception modeling using canopy parameters derived from airborne LiDAR data. Water Resour. Assoc. 51, 5041–5059. https://doi.org/10.1111/j.1752-1688.1969.tb04897.x

Motta, R., Ascoli, D., Corona, P., Marchetti, M., Vacchiano, G., 2018. Silviculture and wind damages. The storm "Vaia." For. - Riv. di Selvic. ed Ecol. For. 15, 94–98. https://doi.org/10.3832/efor2990-015

Niculiță, M., 2020. Geomorphometric methods for burial mound recognition and extraction from high-resolution LiDAR DEMs. Sensors 20, 1192. https://doi.org/10.3390/s20041192

Olmedo, I., Bourrier, F., Berger, Frédéric, Limam, A., Bertrand, D., Lollino, G., Giordan, D., Crosta, G.B., Corominas, J., Azzam, R., Wasowski, J., Sciarra, N., Berger, Frederic, 2015. Felled Trees as a Rockfall Protection System: Experimental and Numerical Studies Felled Trees as a Rockfall Protection System: Experimental and Numerical Studies Felled trees as a rockfall protection system: ex-perimental and numerical studies. Eng. Geol. Soc. Territ. 2, 1889–1893. https://doi.org/10.1007/978-3-319-09057-3_335ï

Paine, R.T., Tegner, M.J., Johnson, E.A., 1998. Compounded perturbations yield ecological surprises. Ecosystems 16, 535–545.

Popescu, S.C., Wynne, R.H., 2004. Seeing the trees in the forest: Using lidar and multispectral data fusion with local filtering and variable window size for estimating tree height. Photogramm. Eng. Remote Sensing 70, 589–604. https://doi.org/10.14358/PERS.70.5.589

Qi, W., Saarela, S., Armston, J., Ståhl, G., Dubayah, R., 2019. Forest biomass estimation over three distinct forest types using TanDEM-X InSAR data and simulated GEDI lidar data. Remote Sens. Environ. 232, 111283. https://doi.org/10.1016/j.rse.2019.111283

Quine, C.P., Bell, P.D., 1998. Monitoring of windthrow occurrence and progression in spruce forests in Britain. For. An Int. J. For. Res. 71, 87–97. https://doi.org/10.1093/forestry/71.2.87-a

R Core Team, 2021. R: A language and environment for statistical computing [WWW Document]. R Found. Stat. Comput. URL http://www.r-project.org (accessed 1.28.21).

Radtke, P.J., Amateis, R.L., Prisley, S.P., Copenheaver, C.A., Chojnacky, D.C., Pittman, J.R., Burkhart, H.E., 2009. Modeling production and decay of coarse woody debris in loblolly pine plantations. For. Ecol. Manage. 257, 790–799. https://doi.org/10.1016/j.foreco.2008.10.001

Rammer, W., Brauner, M., Ruprecht, H., Lexer, M.J., 2015. Evaluating the effects of forest management on rockfall protection and timber production at slope scale. Scand. J. For. Res. 30, 719–731. https://doi.org/10.1080/02827581.2015.1046911

Ringenbach, A., Bebi, P., Bartelt, P., Caviezel, A., 2021. The role of forest deadwood in rockfall protection, in: EGU2021.

p. 10791.

Roussel, J.R., Auty, D., Coops, N.C., Tompalski, P., Goodbody, T.R.H., Meador, A.S., Bourdon, J.F., de Boissieu, F., Achim, A., 2020. lidR: An R package for analysis of Airborne Laser Scanning (ALS) data. Remote Sens. Environ. https://doi.org/10.1016/j.rse.2020.112061

Rusu, R.B., Cousins, S., 2011. 3D is here: Point Cloud Library (PCL). Proc. - IEEE Int. Conf. Robot. Autom. 11–14. https://doi.org/10.1109/ICRA.2011.5980567

Saeki, M., Matsuoka, H., 1969. Snow-Buried Young Forest Trees Growing on Steep Slopes. J. Japanese Soc. Snow Ice 31, 19–23. https://doi.org/10.5331/seppyo.31.19

Sappington, J.M., Longshore, K.M., Thompson, D.B., 2007. Quantifying Landscape Ruggedness for Animal Habitat Analysis: A Case Study Using Bighorn Sheep in the Mojave Desert. J. Wildl. Manage. 71, 1419–1426. https://doi.org/10.2193/2005-723

Scheidl, C., Heiser, M., Vospernik, S., Lauss, E., Perzl, · Frank, Kofler, A., Kleemayr, K., Bettella, F., Lingua, E., Garbarino, M., Skudnik, M., Trappmann, D., Berger, F., 2020. Assessing the protective role of alpine forests against rockfall at regional scale. Eur. J. For. Res. 139, 969–980. https://doi.org/10.1007/s10342-020-01299-z

Schiesser, H.H., Pfister, C., Bader, J., 1997. Winter storms in Switzerland north of the Alps 1864/1865-1993/1994. Theor. Appl. Climatol. 58, 1–19. https://doi.org/10.1007/BF00867428

Schneebeli, M., Bebi, P., 2004. Snow and Avalanche Control. Encycl. For. Sci. 397–402. https://doi.org/10.1016/B0-12-145160-7/00271-4

Schönenberger, W., 2002a. Windthrow research after the 1990 storm Vivian in Switzerland: Objectives, study sites, and projects. For. Snow Landsc. Res. 77, 9–16.

Schönenberger, W., 2002b. Post windthrow stand regeneration in Swiss mountain forests: The first ten years after the 1990 storm Vivian. For. Snow Landsc. Res. 77, 61–80.

Schönenberger, W., Noack, A., Thee, P., 2005. Effect of timber removal from windthrow slopes on the risk of snow avalanches and rockfall. For. Ecol. Manage. 213, 197–208. https://doi.org/10.1016/j.foreco.2005.03.062

Schweizer, J., Jamieson, J.B., Schneebeli, M., 2003. Snow avalanche formation. Rev. Geophys. 41. https://doi.org/10.1029/2002RG000123

Seidl, R., Schelhaas, M.J., Lexer, M.J., 2011. Unraveling the drivers of intensifying forest disturbance regimes in Europe. Glob. Chang. Biol. 17, 2842–2852. https://doi.org/10.1111/j.1365-2486.2011.02452.x

Seidl, R., Schelhaas, M.J., Rammer, W., Verkerk, P.J., 2014. Increasing forest disturbances in Europe and their impact on carbon storage. Nat. Clim. Chang. 4, 806–810. https://doi.org/10.1038/nclimate2318

Silva, C.A., Hudak, A.T., Vierling, L.A., Loudermilk, E.L., O'Brien, J.J., Hiers, J.K., Jack, S.B., Gonzalez-Benecke, C., Lee, H., Falkowski, M.J., Khosravipour, A., 2016. Imputation of Individual Longleaf Pine (Pinus palustris Mill.) Tree Attributes from Field and LiDAR Data. Can. J. Remote Sens. 42, 554–573. https://doi.org/10.1080/07038992.2016.1196582

Teich, M., Fischer, J.T., Feistl, T., Bebi, P., Christen, M., Grêt-Regamey, A., 2014. Computational snow avalanche simulation in forested terrain. Nat. Hazards Earth Syst. Sci. 14, 2233–2248. https://doi.org/10.5194/nhess-14-2233-2014

Wohlgemuth, T., Schwitter, R., Bebi, P., Sutter, F., Brang, P., 2017. Post-windthrow management in protection forests of the Swiss Alps. Eur. J. For. Res. 136, 1029–1040. https://doi.org/10.1007/s10342-017-1031-x

Zhang, W., Qi, J., Wan, P., Wang, H., Xie, D., Wang, X., Yan, G., 2016. An easy-to-use airborne LiDAR data filtering method based on cloth simulation. Remote Sens. 8, 501. https://doi.org/10.3390/rs8060501

Zhao, K., Suarez, J.C., Garcia, M., Hu, T., Wang, C., Londo, A., 2018. Utility of multitemporal lidar for forest and carbon monitoring: Tree growth, biomass dynamics, and carbon flux. Remote Sens. Environ. 204, 883–897. https://doi.org/10.1016/j.rse.2017.09.007

6 General conclusions

Throughout the papers reported in the thesis, the reliability of simulation model outcomes has been improved. The papers focused on two types of mass flows: debris flows and snow avalanches. In particular, the thesis aimed to improve the assessment of the volume involved in a mass flow event and the interaction with the basal topography in order to improve the hazard and risk maps through the use of numerical models for the prediction of future events. In the context of this main objective two specific objectives have been addressed. The first deals with the improvement in numerical models of the mass volume acquired along the travelling area caused by the motion of the flow. The second involves the quantification of the initial released volume. Both the objectives have been carried out through the observation, data collection and successive analysis of occurred mass flow events or analysing particular triggering areas. To achieve the specific objectives, four research projects have been developed and successively finalized in four journal articles. The first two papers (chapter 2 and 3) improved the quantification of the volume acquired in the travelling area, while the last two papers (chapter 4 and 5) improved the volume quantification of triggering areas that provide initial volume to mass flow events.

Along the first research project, I focused on the evaluation of debris flow entrainment processes with the aim to improve their implementation in numerical models. Thanks to a well-documented extreme debris flow event occurred in the Gere channel (IT) we evaluated the observed entrained volume. The values correlated well with the smoothed channel slope and starting from this relation we calibrated a function based on the local slope, as well observed in the studies of Kronfellner-Kraus (1984) and Rickenmann and Zimmermann (1993), to derive an erosion coefficient used in the empirical erosion model implemented in the simulation tool r.avaflow. An exponential function resulted the best relation to accurately simulate the observed erosion volumes within two different areas of the channel. Results of this study can be exported also to other numerical models, since the erosion model implemented in r.avaflow is relatively easy to implement. Furthermore, the calibrated function can be used in channels of similar geology respect the studied one to improve the representation of erosion processes. In the study we also report other functions that could be adequate in other debris flow channels characterised by a different geology and availability of sediment. In particular, the paper addressed a gap of knowledge reported in literature concerning the necessity of simulating the process of bed erosion and successive material recruitment by debris flows. In fact, bed erosion was recognized as an important driver for the increase in debris flow magnitude (Jakob et al., 2005). Studies reported entrainment rates per channel length up to 100 m^3/m (Hungr et al., 2005; Marchi and D'Agostino, 2004; Marchi and Cavalli, 2007; Rickenmann and Zimmermann, 1993) and in some cases to 300 m^3/m for particular geological conditions and magnitude of the event (Rickenmann et al., 2003). Therefore the necessity to model reliably debris flow erosion was recognized and some empirical and process-based models have been devoleped and tested to back calculate real events (Armanini et al., 2009; Berger et al., 2011; Chen et al., 2006; Crosta et al., 2015; Egashira and Ashida, 1987; Hungr et al., 1984; Takahashi and Kuang, 1986). Most of the erosion models have been combined with single-phase routing

models (Pirulli and Pastor, 2012), leading to the simplification of the flow propagation and the processes of bed erosion and mass recruitment. The development of multi-phase physically based models (Pudasaini, 2012; Pudasaini and Mergili, 2019; Rosatti and Begnudelli, 2013) provided the opportunity to improve the modellization of erosion processes including the existing erosion models in the most advanced debris flow propagation models. In the article presented in chapter 2 of this thesis the multiphase routing model proposed by (Pudasaini and Mergili, 2019) together with the multiphase entrainment momentum based model (Mergili et al., 2017) has been used to appropriately reproduce the observed erosion pattern. The presented study together with similar ones (Armanini et al., 2009; Gregoretti et al., 2019; Starkloff and Stolte, 2014) provide a methodological approach to improve the representation of the dynamic of debris flow phenomena with the use of numerical models. Moreover, the presented paper provided new insights regarding the simulation of debris flow initiation processes through entrainment of the debris component from the channel bed. Civil authorities and technicians can benefit from these advances since they can improve the predictions of future events refining the existing hazard and risk maps.

In the same topic of mass flow entrainment, the second paper (chapter 3) analyses the phenomena of check dam collapse and successive mass increase through a simulation model. The study focuses on the debris flow event occurred at the end of the Vaia storm (2018) in the Rotian channel (IT). The phenomenon was particularly intense and the 15 check dams located in the channel collapsed. With the aim to reproduce the observed event with numerical models, we specifically developed and tested a methodology to reproduce the effect of check dam collapse. It consists in releasing the mass retained by the check dam at the passage of the flow in combination with bed erosion. In fact, comparing the simulated released mass (assumed equal to the mass retained by the check dam) with the observed erosion deposition pattern, we established that the increase in flow volume derived mainly by erosion processes. The study highlighted the importance of erosion processes - as reported in the previous paper presented in chapter 2 and by different authors - and the need of an accurate representation of entrainment in mass flow models. The proposed method resulted adequate to represent the effect of check dam collapse bettering the outcomes of previous studies (Marchelli and De Biagi, 2019; Sodnik et al., 2013) for the representation of mass released and the successive bed destabilization and erosion. Moreover, the proposed implementation for simulating the effect of check dam collapse is exportable to simulation models that have a great flexibility of mass input within the computational domain. The study provides the novel representation of the effect of check dam collapse in numerical models offering new tools for civil authorities to calculate the residual hazard and the related risk (Hartmann et al., 2021) associated to mitigation structure failure (especially useful when they are getting old). In such sense, the concept that mitigation structures are always considered adequate to decrease the magnitude of mass flows cannot be assumed if the structure stability is decreasing or in case of extreme events (return period > 300 years) or in combination with other mass movements (landslides, bank collapse, permafrost melting) as shown in the studies of Benito et al. (1998) and Wang (2013). In this context, the procedure representing the effect of check dam collapse can be also used to evaluate alternative management solutions of unstable mitigation structures that nowadays may not fully protect the target area.

Since such conditions are becoming more and more frequent because most of the check dams of the Alps have been realized before the 70s (Piton et al., 2016), the proposed methodology can be extremely useful to update the hazard maps in accordance with the actual structure conditions, for which the occurrence of failure may occur.

Regarding the third paper (chapter 4), the focus is on surface roughness as a factor influencing the estimation of initial volume of mass flows and the routing modelling. The objective of the study is to represent land covers interacting with mass flows that are commonly not taken in consideration such as shrub, disturbed and sparse forests together with other standard land covers as dense forest, rocky areas, smooth and very smooth surfaces. The objective was achieved analysing the performance of roughness algorithms in distinguishing the reported land covers. The vector ruggedness measure (Sappington et al., 2007a) resulted the algorithm that best performed. Testing the standard roughness approach against the directional one (appositely implemented in this study) we found out that the first one overestimates roughness values. Therefore, the use of directional roughness algorithms is certainly effective to improve the reliability of roughness maps as highlighted in the study of Trevisani and Cavalli (2016). The study also shows that DEMs with a spatial resolution of 1 m, which are becoming widespread, are well suited for use with roughness algorithms for natural hazard terrain classification and that higher spatial resolutions (0.1–0.5 m) do not necessarily improve the terrain surface roughness representation. Outcomes of the project can be integrated in existing algorithms (Bühler et al., 2013; Viglietti et al., 2009) to improve the generation of forest layers applied for large-scale hazard indication mapping. The suggested roughness algorithm and the directional one can be also used as a base to produce basal frictional coefficient maps. Their application in mass routing models can improve the representation of land covers interacting with natural hazards, so bettering the model performance.

In the fourth paper (chapter 5) the mitigation effect of a specific land cover has been assessed. In particular, forests affected by storm events are studied, by analysing the biomass on the ground to specifically quantify their protective function in the formation of snow avalanches. Two indices are developed to analyse the protection function of the felled trees (stored volume height) and to identify the remaining standing and new trees (adapted trees parameters). The indices are used to assess both the long-term temporal change of an abated forest (study area Disentis, CH), the short-term temporal change and the effect of the snow cover (study area Franza, IT). Analysing the Disentis area, the minimum level of protection was observed ten years since the storm event as consequence of biomass degradation and the slow rate of natural regeneration. The outcome is a novelty respect to previous studies for which the timing of minimum level of protection has not been assessed neither for small control areas (Frey and Thee, 2002). Regarding, the short-term temporal change, it has been obtained that in the years immediately after the storm the forest protection capacity temporally increased due to the breakage processes of small branches. This breakage increased the space between the stems, enhancing the potential volume of snow that can be stabilized. Thanks to a winter survey we found a good protection capacity of abated forests immediately after the event, estimating a cumulated snow depth around 3 m necessary to smooth the irregular surface of the abated trees. In contrast

with the homogenous conditions of the pre-storm forests, results of the study showed that the characteristics of wind-disturbed forests were spatially different. This aspect implies an accurate evaluation of the biomass structure to reliably define the protection capacity of windthrown areas. The study addresses this methodological gap, proposing two new indices to spatially assess and monitor over time and on large areas the protection capacity of forests affected by windstorm against snow avalanches. The proposed method overcomes previous approaches mainly based on field surveys of small study areas (Schönenberger, 2002a; Wohlgemuth et al., 2017). In particular, the two implemented algorithms can be applied to map large areas, since the required input are point clouds derivable from LiDAR or photogrammetric surveys. In this way civil authorities can quickly identify the most critical areas and effectively plan and design mitigation structures to reduce the risk toward citizens.

The four papers presented in this thesis advance the actual knowledge on the estimation and representation of volume involved in mass flow phenomena for a modelling purpose. Improvements are obtained investigating the processes of erosion and entrainment through calibration and implementation in a simulation tool. Advances are also obtained in the delineation and assessment of areas which are sources of the initial volume to mass flows. At this purpose, two codes are developed and published in open-source format and they are available online.

All outcomes are based on observations of occurred events followed by data collection and methodological solution development to fill the identified gap of knowledge in flow mass modelling. The findings provide effective methods and algorithms that can be straight used by researchers or civil authorities to improve the reliability of simulation model outcomes.

All this is realized throughout operative procedures that have been developed and tested and have bettered our capacity to predict the potential areas impacted by mass flows and, consequently, to effectively reduce the vulnerability of citizens and infrastructures.

References (General introduction and conclusions)

Allan, R. P., Hawkins, E., Bellouin, N. and Collins, B.: IPCC, 2021: Summary for Policymakers, 2021.

Armanini, A., Fraccarollo, L. and Rosatti, G.: Two-dimensional simulation of debris flows in erodible channels, Comput. Geosci., 35(5), 993–1006, doi:10.1016/j.cageo.2007.11.008, 2009.

Barbolini, M., Gruber, U., Keylock, C. ., Naaim, M. and Savi, F.: Application of statistical and hydraulic-continuum dense-snow avalanche models to five real European sites, Cold Reg. Sci. Technol., 31(2), 133–149, doi:10.1016/S0165-232X(00)00008-2, 2000.

Bebi, P., Bast, A., Helzel, K., Schmucki, G., Brozova, N. and Bühler, Y.: Avalanche protection forest: from process knowledge to interactive maps, in IntechOpen., 2021.

Benito, G., Grodek, T. and Enzel, Y.: The geomorphic and hydrologic impacts of the catastrophic failure of flood-control-dams during the 1996-Biescas flood (Central Pyrenees, Spain), Zeitschrift fur Geomorphol., 42(4), 417–437, doi:10.1127/zfg/42/1998/417, 1998.

Berger, C., McArdell, B. W. and Schlunegger, F.: Direct measurement of channel erosion by debris flows, Illgraben, Switzerland, J. Geophys. Res. Earth Surf., 116(F1), n/a-n/a, doi:10.1029/2010JF001722, 2011.

Berti, M. and Simoni, A.: Experimental evidences and numerical modelling of debris flow initiated by channel runoff, Landslides, 2(3), 171–182, doi:10.1007/s10346-005-0062-4, 2005.

Brožová, N., Fischer, J.-T., Bühler, Y., Bartelt, P. and Bebi, P.: Determining forest parameters for avalanche simulation using remote sensing data, Cold Reg. Sci. Technol., 172, 102976, doi:10.1016/j.coldregions.2019.102976, 2020.

Bühler, Y., Kumar, S., Veitinger, J., Christen, M. and Stoffel, A.: Automated identification of potential snow avalanche release areas based on digital elevation models, Nat. Hazards Earth Syst. Sci., 13(5), 1321–1335, doi:10.5194/nhess-13-1321-2013, 2013.

Chen, H., Crosta, G. B. and Lee, C. F.: Erosional effects on runout of fast landslides, debris flows and avalanches: a numerical investigation, Géotechnique, 56(5), 305–322, doi:10.1680/geot.2006.56.5.305, 2006.

Church, M. and Jakob, M.: What Is a Debris Flood?, Water Resour. Res., 56(8), doi:10.1029/2020WR027144, 2020.

Crosta, G. B., De Blasio, F. V., Locatelli, M., Imposimato, S. and Roddeman, D.: Landslides falling onto a shallow erodible substrate or water layer: an experimental and numerical approach, IOP Conf. Ser. Earth Environ. Sci., 26(1), 012004, doi:10.1088/1755-1315/26/1/012004, 2015.

Cucchiaro, S., Cavalli, M., Vericat, D., Crema, S., Llena, M., Beinat, A., Marchi, L. and Cazorzi, F.: Geomorphic effectiveness of check dams in a debris-flow catchment using multi-temporal topographic surveys, Catena, 174(February 2018), 73–83, doi:10.1016/j.catena.2018.11.004, 2019.

Egashira, S. and Ashida, K.: Sediment transport in steep slope flumes, in Japan Joint Seminar on Water Resources., 1987.

Ellen, S. D., Algus, M. A., Cannon, S. H., Fleming, R. W., Lahr, P. C., Peterson, D. M. and Reneau, S. L.: Description and mechanics of soil slip/debris flows in the storm, California. U.S. Geol. Surv. Prof. Pap., 1434, 63–112, 1982.

Frey, W. and Thee, P.: Avalanche protection of windthrow areas: A ten year comparison of cleared and uncleared starting zones. [online] Available from: http://www.bf.uni-lj.si/fileadmin/groups/2716/downloads/Članki_vaje/Frey___Thee_2002.pdf (Accessed 29 November 2018), 2002.

Fuchs, S., Röthlisberger, V., Thaler, T., Zischg, A. and Keiler, M.: Natural Hazard Management from a Coevolutionary Perspective: Exposure and Policy Response in the European Alps, Ann. Am. Assoc. Geogr., 107(2), 382–392, doi:10.1080/24694452.2016.1235494, 2017.

Gall, M., Borden, K. A., Emrich, C. T. and Cutter, S. L.: The unsustainable trend of natural hazard losses in the United States, Sustainability, 3(11), 2157–2181, doi:10.3390/su3112157, 2011.

Gregoretti, C., Stancanelli, L. M., Bernard, M., Boreggio, M., Degetto, M. and Lanzoni, S.: Relevance of erosion processes when modelling in-channel gravel debris flows for efficient hazard assessment, J. Hydrol., 568(September 2018), 575–591, doi:10.1016/j.jhydrol.2018.10.001, 2019.

Griffiths, P. G., Webb, R. H. and Melis, T. S.: Initiation of debris flows in tributaries of the Colorado River in Grand Canyon, Arizona, in 1st International Conference on Debris-Flow Hazards Mitigation, Mechanics, Prediction and Assessment., 1997.

Hartmann, S., Pedoth, L., Dalla Torre, C. and Schneiderbauer, S.: Beyond the Expected-Residual Risk and Cases of Overload in the Context of Managing Alpine Natural Hazards, Int. J. Disaster Risk Sci., 12(2), 205–219, doi:10.1007/s13753-020-00325-3, 2021.

Hungr, O., Morgan, G. C. and Kellerhals, R.: Quantitative analysis of debris torrent hazards for design of remedial measures., Can. Geotech. J., 21(4), 663–677, doi:10.1139/t84-073, 1984.

Hungr, O., McDougall, S. and Bovis, M.: Entrainment of material by debris flows, in Debris-flow Hazards and Related Phenomena, pp. 135–158, Springer, Berlin, Heidelberg., 2005.

Hungr, O., Leroueil, S. and Picarelli, L.: The Varnes classification of landslide types, an update, Landslides, 11(2), 167–194, doi:10.1007/s10346-013-0436-y, 2014.

Huppert, H. E. and Sparks, R. S. J.: Extreme natural hazards: population growth, globalization and environmental change, Philos. Trans. R. Soc. A Math. Phys. Eng. Sci., 364(1845), 1875–1888, doi:10.1098/rsta.2006.1803, 2006.

Iverson, R. M. and Vallance, J. W.: New views of granular mass flows, Geology, 29(2), 115–118, doi:10.1130/0091-7613(2001)029<0115:NVOGMF>2.0.CO;2, 2001.

Jakob, M., Hungr, O. and Jakob, D.: Debris-flow hazards and related phenomena. [online] Available from: https://link.springer.com/content/pdf/10.1007/b138657.pdf (Accessed 27 November 2018), 2005.

Jamieson, B. and Stethem, C.: Snow avalanche hazards and management in Canada: Challenges and progress, Nat. Hazards, 26(1), 35–53, doi:10.1023/A:1015212626232, 2002.

Kronfellner-Kraus, G.: Extreme Feststofffrachten und Grabenbildungen von Wildbächen [ex- treme sediment loads and erosion of torrents], in Int. Symp. Interpraevent, pp. 109–118, Villach., 1984.

Marchelli, M. and De Biagi, V.: Dynamic effects induced by the impact of debris flows on protection barriers, Int. J. Prot. Struct., 10(1), 116–131, doi:10.1177/2041419618798378, 2019.

Marchi, L. and Cavalli, M.: Procedures for the documentation of historical debris flows: Application to the Chieppena Torrent (Italian Alps), Environ. Manage., 40(3), 493–503, doi:10.1007/s00267-006-0288-5, 2007.

Marchi, L. and D'Agostino, V.: Estimation of debris-flow magnitude in the Eastern Italian Alps, Earth Surf. Process. Landforms, 29(2), 207–220, doi:10.1002/esp.1027, 2004.

Mergili, M., Fischer, J. T., Krenn, J. and Pudasaini, S. P.: R.avaflow v1, an advanced open-source computational framework for the propagation and interaction of two-phase mass flows, Geosci. Model Dev., 10(2), 553–569, doi:10.5194/gmd-10-553-2017, 2017.

O'Brien, J. S., Julien, P. Y. and Fullerton, W. T.: Two-dimensional water flood and mudflow simulation, J. Hydraul. Eng., 119(2), 244–261, doi:10.1061/(asce)0733-9429(1993)119:2(244), 1993.

Perla, R., Creng, T. T. and Mcclung, D. M.: A TWO-PARAMETER MODEL OF SNOW-AVALANCHE MOTION., 1980.

Pierson, T. C.: Flow behavior of channelized debris flows, Mount St. Helens, Washington, Hillslope Process, 269–296, 1986.

PIRULLI, M. and PASTOR, M.: Numerical study on the entrainment of bed material into rapid landslides, Géotechnique, 62(11), 959–972, doi:10.1680/geot.10.P.074, 2012.

Piton, G. and Recking, A.: The dynamic of streams equipped with Check Dams, in River Flow 2014, pp. 1437–1445, CRC Press., 2014.

Piton, G., Carladous, S., Recking, A., Tacnet, J. M., Liébault, F., Kuss, D., Quefféléan, Y. and Marco, O.: Why do we build check dams in Alpine streams? An historical perspective from the French experience, Earth Surf. Process. Landforms, 42(1), 91–108, doi:10.1002/esp.3967, 2016.

Pudasaini, S. P.: A general two-phase debris flow model, J. Geophys. Res. Earth Surf., 117(3), 1–28,

doi:10.1029/2011JF002186, 2012.

Pudasaini, S. P. and Fischer, J.-T.: A mechanical erosion model for two-phase mass flows, , 1–21 [online] Available from: http://arxiv.org/abs/1610.01806, 2016.

Pudasaini, S. P. and Fischer, J. T.: A mechanical erosion model for two-phase mass flows, Int. J. Multiph. Flow, 132, 1–16, doi:10.1016/j.ijmultiphaseflow.2020.103416, 2020.

Pudasaini, S. P. and Hutter, K.: Avalanche dynamics, Berlin, Heidelberg., 2007.

Pudasaini, S. P. and Krautblatter, M.: The Mechanics of Landslide Mobility with Erosion, [online] Available from: http://arxiv.org/abs/2103.14842 (Accessed 2 July 2021), 2021.

Pudasaini, S. P. and Mergili, M.: A multi-phase mass flow model, J. Geophys. Res. Earth Surf., 124, 1–23, doi:10.1029/2019jf005204, 2019.

Quervain, de, M. R. and Quervain de, M. R.: Problems of avalanche research, Sym- posium Davos 1965—Scientific Asp. Snow Ice Avalanches, IAHS Publ., 69, 1–8, 1966.

Raschky, P. A.: Institutions and the losses from natural disasters, Nat. Hazards Earth Syst. Sci., 8(4), 627–634, doi:10.5194/nhess-8-627-2008, 2008.

Rickenmann, D. and Zimmermann, M.: The 1987 debris flows in Switzerland: documentation and analysis, Geomorphology, 8(2–3), 175–189, doi:10.1016/0169-555X(93)90036-2, 1993.

Rickenmann, D., Weber, D. and Stepanov, B.: Erosion by debris flows in field and laboratory experiments, Int. Conf. Debris-Flow Hazards Mitig. Mech. Predict. Assessment, Proc., 2, 883–894, 2003.

Rosatti, G. and Begnudelli, L.: Two-dimensional simulation of debris flows over mobile bed: Enhancing the TRENT2D model by using a well-balanced Generalized Roe-type solver, Comput. Fluids, 71, 179–195, doi:10.1016/j.compfluid.2012.10.006, 2013.

Sappington, J. M., Longshore, K. M. and Thompson, D. B.: Quantifying landscape ruggedness for animal habitat analysis: a case study using bighorn sheep in the Mojave Desert, J. Wildl. Manage., 71(5), 1419–1426, doi:10.2193/2005-723, 2007.

Schlögel, R., Kofler, C., Gariano, S. L., Van Campenhout, J. and Plummer, S.: Changes in climate patterns and their association to natural hazard distribution in South Tyrol (Eastern Italian Alps), Sci. Rep., 10(1), 1–14, doi:10.1038/s41598-020-61615-w, 2020.

Schönenberger, W.: Post windthrow stand regeneration in Swiss mountain forests: The first ten years after the 1990 storm Vivian, For. Snow Landsc. Res., 77(1–2), 61–80, 2002.

Schönenberger, W., Noack, A. and Thee, P.: Effect of timber removal from windthrow slopes on the risk of snow avalanches and rockfall, For. Ecol. Manage., 213(1–3), 197–208, doi:10.1016/j.foreco.2005.03.062, 2005.

Schweizer, J., Jamieson, J. B. and Schneebeli, M.: Snow avalanche formation, Rev. Geophys., 41(4), doi:10.1029/2002RG000123, 2003.

Soares-Frazão, S., Lhomme, J., Guinot, V. and Zech, Y.: Two-dimensional shallow-water model with porosity for urban flood modelling, J. Hydraul. Res., 46(1), 45–64, doi:10.1080/00221686.2008.9521842, 2008.

Sodnik, J., Kryžanowski, A., Martin, M. and Mikoš, M.: Torrential Check Dams as Debris-Flow Sources, in Landslide and Flood Hazard Assessment, pp. 6–9, Zagreb., 2013.

Sovilla, B., Burlando, P. and Bartelt, P.: Field experiments and numerical modeling of mass entrainment in snow avalanches, J. Geophys. Res. Earth Surf., 111(3), 1–16, doi:10.1029/2005JF000391, 2006.

Sovilla, B., Margreth, S. and Bartelt, P.: On snow entrainment in avalanche dynamics calculations, Cold Reg. Sci. Technol., 47(1-2 SPEC. ISS.), 69–79, doi:10.1016/j.coldregions.2006.08.012, 2007.

Starkloff, T. and Stolte, J.: Applied comparison of the erosion risk models EROSION 3D and LISEM for a small catchment in Norway, Catena, 118, 154–167, doi:10.1016/j.catena.2014.02.004, 2014.

Takahashi, T.: Initiation and flow of various types of debris-flow, in Debris-flow hazards mitigation: mechanics, prediction, and assessment, pp. 15–25., 2000.

Takahashi, T.: Debris Flow: Mechanics, Prediction and Countermeasures, Taylor & Francis., 2007.

Takahashi, T. and Kuang, S. F.: Formation of debris flow on varied slope bed, Disaster Prev. Res. Inst. Annu., 29, 343–359, 1986.

Teich, M., Fischer, J. T., Feistl, T., Bebi, P., Christen, M. and Grêt-Regamey, A.: Computational snow avalanche simulation in forested terrain, Nat. Hazards Earth Syst. Sci., 14(8), 2233–2248, doi:10.5194/nhess-14-2233-2014, 2014.

Trevisani, S. and Cavalli, M.: Topography-based flow-directional roughness: potential and challenges, Earth Surf. Dyn., 4(2), 343–358, doi:10.5194/esurf-4-343-2016, 2016.

Veitinger, J., Purves, R. S., Sovilla, B., Stuart Purves, R. and Sovilla, B.: Potential slab avalanche release area identification from estimated winter terrain: a multi-scale, fuzzy logic approach, Nat. Hazards Earth Syst. Sci., 16(10), 2211–2225, doi:10.5194/nhess-16-2211-2016, 2016.

Viglietti, D., Letey, S., Motta, R., Maggioni, M. and Freppaz, M.: Snow and avalanche: The influence of forest on snowpack stability, ISSW 09 - Int. Snow Sci. Work. Proc., 323–327, 2009.

Wang, G. L.: Lessons learned from protective measures associated with the 2010 Zhouqu debris flow disaster in China, Nat. Hazards, 69(3), 1835–1847, doi:10.1007/s11069-013-0772-1, 2013.

Wohlgemuth, T., Schwitter, R., Bebi, P., Sutter, F. and Brang, P.: Post-windthrow management in protection forests of the Swiss Alps, Eur. J. For. Res., 136(5–6), 1029–1040, doi:10.1007/s10342-017-1031-x, 2017.

Zeng, Q. L., Yue, Z. Q., Yang, Z. F. and Zhang, X. J.: A case study of long-term field performance of check-dams in mitigation of soil erosion in Jiangjia stream, China, Environ. Geol., 58(4), 897–911, doi:10.1007/s00254-008-1570-z, 2009.

Figure index

Table index